Light Deflection And Absorption Of High-Redshift Quasars By Intervening Galaxy Systems

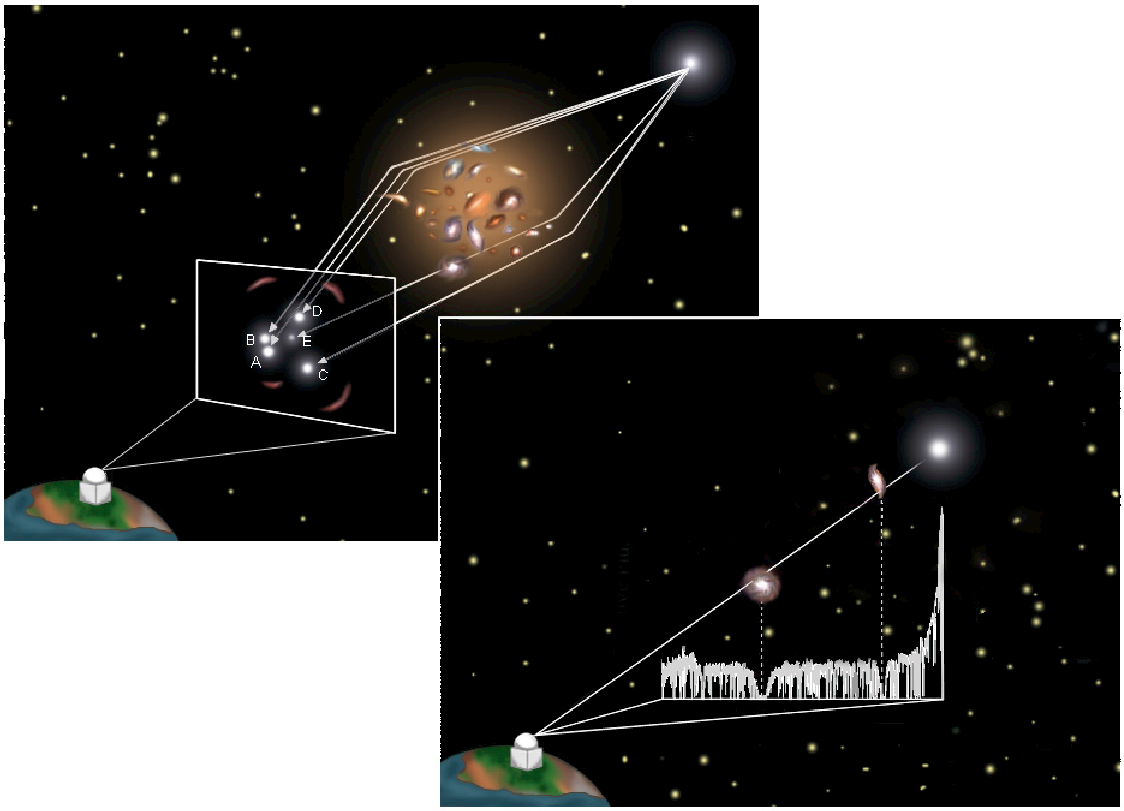

Janine Fohlmeister

Dissertation

submitted to the
Combined Faculties for the Natural Sciences and for Mathematics
of the Ruperto-Carola University of Heidelberg, Germany
for the degree of
Doctor of Natural Sciences

presented by

Diplom-Physikerin Janine Fohlmeister
Born in Guben, Germany

Oral examination: 30 April 2008

Light Deflection and Absorption of high-redshift Quasars by intervening Galaxy Systems

Referees: Prof. Dr. Joachim Wambsganß
Prof. Dr. Matthias Bartelmann

Zusammenfassung.
Die Ablenkung und Absorption des Lichtes hochrotverschobener Quasare durch Galaxiensysteme entlang der Sichtlinie werden in dieser Arbeit untersucht. Ein Beispiel starker Absorption ist das gedämpfte Lyα System im Spektrum des Quasars PKS 0458−020, bei welchem im Zentrum der breiten Absorption eine H I Lyα Emissionslinie zu sehen ist. Anhand dieser kann die Sternentstehungsrate des Systems zu $1,6^{+0,6}_{-0,3}$ $M_\odot$ a^{-1} bestimmt werden. Die beobachteten Metallabsorptionslinien sind zu kürzeren Wellenlängen hinverschoben, was einer Geschwindigkeit von bis zu 200 km s^{-1} entspricht. Die Ursache dafür ist entweder die Rotation einer großen Scheibe (~ 7 kpc) oder ein galaktischer Wind. Die Spektren der beiden 1,7 Bogensekunden auseinander liegenden Quasare Q 0037-3544 und Q 0037-3545 zeigen mehrere Lyα- und Metallabsorptionslinien bei gleicher Rotverschiebung. Mit Hilfe von Aufnahmen der Himmelsregion um beide Quasare in verschiedenen Filtern konnten Galaxien bei eben diesen Rotverschiebungen identifiziert werden. Daraus folgt, dass die Ausdehnung der für die Absorption verantwortlichen Strukturen mehr als 760 kpc beträgt. Die Ablenkung des Lichtes durch einen als Linse wirkenden Galaxienhaufen wird anhand des weit aufgespaltenen fünfach-Quasars SDSS J1004+4112 untersucht. Von diesem wurden über vier Jahre hinweg Lichtkurven gewonnen, anhand welcher die Lichtlaufzeitdifferenzen zwischen den Quasarbildern gemessen wurden. Diese betragen $\Delta\tau_{BA} = 40,6 \pm 1,8$ Tage zwischen den Bildern A und B und $\Delta\tau_{CA} = 821,6 \pm 2,1$ Tage (2,3 Jahre) zwischen den Bildern A und C. Letztere ist die längste bisher gemessene Lichtlaufzeitdifferenz in einem mehrfach gelinsten Quasar. Die untere Grenze für die Lichtlaufzeitdifferenz zwischen den Bildern A und D ist $\Delta\tau_{AD} > 1250$ Tage. Der Mikrogravitationslinseneffekt wird beobachtet und die intrinsische Variabilität des Quasars untersucht.

Abstract.
The light of a distant quasar can be affected by deflection and absorption by intervening galaxy systems. One example of strong absorption is the damped Lyα (DLA) system towards the quasar PKS 0458−020, in which H I Lyα is also detected in emission in the center of the damped Lyα absorption trough. We estimate the star formation rate of the DLA galaxy to be $1.6^{+0.6}_{-0.3}$ $M_\odot$ yr^{-1}. The associated metal lines are found to be blueshifted compared to the Lyα emission up to a maximum of $\sim$200 km s^{-1}. This can be interpreted either as the consequence of rotation in a large disk (~ 7 kpc) or as the imprint of a galactic wind. In a similar study, the analysis of Lyα and metal absorption lines in the spectra of the quasar pair Q 0037-3544 and Q 0037-3545 reveal the spatial extent of absorbing structures. We obtained deep images of the field around the two quasars that allow us to identify galaxies at redshifts corresponding to the observed absorptions, indicating that the absorbing structures extend over a distance of 760 kpc. The effect of quasar light deflection is analyzed by studying the variability of the wide separation quintuple gravitational lensed quasar SDSS J1004+4112. Four years of optical monitoring were obtained for the four brightest images. These light curves allow the measurement of the differences in the light arrival times, the time delay, between the images. The measured time delay between the image pair A and B is $\Delta\tau_{BA} = 40.6 \pm 1.8$ days and between images C and A $\Delta\tau_{CA} = 821.6 \pm 2.1$ days (2.3 years). The time delay between the images C and A is the longest measured time delay in a gravitationally lensed quasar so far. A lower limit on the remaining delay between image D and A of $\Delta\tau_{AD} > 1250$ days is derived. We detect microlensing and characterize the intrinsic variability of the quasar.

For my second child.

Contents

Chapter 1

Introduction

1.1 Quasars

In 1963 the first quasars were detected and found to be very distant and compact sources (Matthews & Sandage 1963). It was realized that quasars are very luminous ($\approx 10^{14} L_{\odot}$). They emit about 1000 times more radiation than our galaxy. The generally accepted model for the quasar engine is accretion of matter onto a massive ($10^6 - 10^9 M_{\odot}$) black hole. Since the time scales of quasar variability are small (down to the order of days), the size of the accretion disk can be estimated to be $< 10^{15}$cm. The disk is heated by the release of gravitational potential energy. The inner disk is the source of thermal X-ray emission whereas in the outer disk the UV and optical continuum originates. Along the rotational axis of the central black hole radio jets can be observed. The inner region of the quasar is believed to be surrounded by ionized gas clouds that emit Doppler-broadened lines due to their rapid orbital motion around the central engine. Broad line reverberation mapping studies (that measure the response times of broad line variations compared to the continuum) determine the size of the broad line region to be about 10^{16}cm. On an even larger scale the whole structure is believed to be enclosed by a gas and dust torus that emits infrared radiation. In the described model narrow lines arise from gas clouds that are even further out, at $\sim 10^{20}$cm. Depending on the inclination angle under which the quasar is observed, the torus can obscure the central region, so that different emission features become prominent or remain blocked in the spectra. This orientational characteristic led to the classification of different quasar types, like Seyfert galaxies, LINERs, Radio-Galaxies, BL Lac and others.

Quasar spectra show a continuum that can be described by a power law. Superimposed on this continuum are broad emission lines with widths of ~ 5000 kms^{-1} and narrow lines with widths of ~ 500 kms^{-1}. The strongest emission line in quasar spectra is the Lyman-α (Lyα) line. It is characteristic of the simplest and most abundant atom in the Universe, the hydrogen atom. The line is emitted with a wavelength of 1215.67 Å when an electron falls from the second energy level to the ground state.

Figure 1.1 shows the composite spectrum of quasars from the Sloan Digital Sky Survey between 800 Å and 8555 Å. Redward of the Lyα line the continuum is fitted with two power laws and a break wavelength of ~ 5000 Å. Beside the strong Lyα line several broad emission lines such as C IV and Mg II, as well as narrow forbidden lines such as O [III], are superimposed.

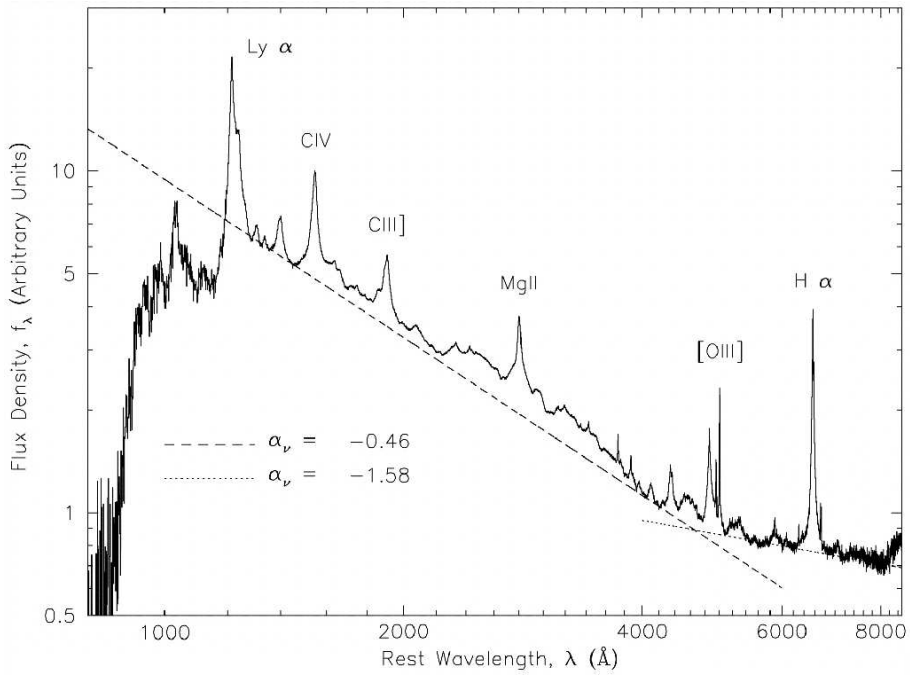

Figure 1.1: Median quasar spectrum between 800Å and 8555Å. This represents the composite of 2200 individual spectra of quasars found in the Sloan Digital Sky Survey with redshifts $0.044 \leq z \leq 4.789$. Several broad and narrow emission lines are indicated. The continuum is fitted by two power laws with a break at $\sim$ 5000Å (from Vanden Berk et al. 2001).

Quasars are uniformly distributed on the sky. They have been detected up to redshifts of $z > 6$. With the advent of large sky surveys the number of known quasars has increased enormously. The 2dF QSO redshift survey comprises the information for more than 20 000 quasars (Croom et al. 2004). The latest data release of the Sloan Digital Sky Survey[1] even contains a spectroscopic catalog of more than 100 000 quasars. These samples have been used for detailed statistical analysis of the quasar population regarding different properties, such as black hole mass (Corbett et al. 2003), luminosity function (Boyle et al. 2000), redshift evolution (Fan et al. 2001), clustering (Myers et al. 2006) and variability (Wilhite et al. 2006, Vanden Berk et al. 2004).

Apart from studying quasars themselves, their illuminating properties make them interesting objects for various astrophysical reasons. Quasars are the only bright and compact sources that can be found up to high redshift and that shine continuously. Additionally, their uniform distribution on the sky makes them ideal background candles for a number of cosmological studies.

1.2 Thesis Motivation

In the following we use four quasars as light sources to investigate different effects. The light of a distant quasar can be affected by concentrations of matter of various types along

[1] http://www.sdss.org/dr6/

the line of sight. Two of the most important phenomena are studied in this thesis: the absorption and the deflection of quasar light by intervening galaxy systems.

In Part I we will focus on the effect of light absorption by intervening galaxy systems along quasar sight lines. In Chapter 4 we will study the high column density absorption by an intervening damped Lyman-α system along the line of sight to the quasar PKS 0458-020. From the relative velocities of the observed metal absorption lines we can draw conclusions on the kinematics of the galaxy responsible for the absorption. In Chapter 5 we correlate the spatial information from the imaging of field galaxies with the spectral information of absorbers along the lines of sight towards the quasar pair Q 0037-3544 and Q 0037-3545.

Then in Part II we study the phenomenon of quasar light deflection by intervening massive galaxy systems that causes the creation of multiple quasar images. An overview on the present sample of lensed quasar systems is given and we repeat the basic principles of lensing theory. In Chapter 7 the unique wide-angle quintuply gravitationally lensed quasar SDSS J1004+4112 is analyzed regarding its variability. The obtained light curves allow the measurement of the time delays between the images.

Quasars are high-redshifted objects that take part in the expansion of the Universe. We will therefore first introduce the basic cosmological concepts that lead to the definition of distances in curved space-time in the next Chapter.

Chapter 2

Cosmological Concepts

In this Chapter we give a brief introduction to the standard model of cosmology. In this model the expansion of the Universe started 13.7 billion years ago with the Big Bang. During this expansion the Universe cooled down and simple particles could form that subsequently merged to build the structures that are observed today.

2.1 Einstein Equation

The fundamental equations of general relativity are the Einstein field equations, that relate the curvature of space-time to the distribution of matter and energy:

$$G_{ik} = \frac{8\pi G}{c^4} T_{ik} + \Lambda g_{ik}. \tag{2.1}$$

The Einstein tensor G_{ik} describes the geometry of space-time, the energy-momentum tensor T_{ik} represents the distribution of matter and energy. g_{ik} is the metric and the cosmological constant Λ plays the role of an integration constant.

2.2 The Dynamics of the Universe

The cosmological principle states that on average the matter in the Universe on large scales is distributed homogeneously and isotropically. The dynamics of the Universe is described by the Robertson-Walker metric:

$$ds^2 = c^2 dt^2 - a^2(t) \left[\frac{dr^2}{1 - kr^2} + r^2 (d\theta^2 + sin^2\theta d\phi^2) \right] \tag{2.2}$$

in comoving spherical coordinates (r, θ, ϕ), where ds is the line element and k the spatial curvature. Spaces with $k > 0$, $k = 0$ and $k < 0$ are called closed, flat and open, respectively. The time dependence of the geometry is given by the scale factor $a(t)$, which is normalized to a present (t_o) value of unity $a_o = 1$. It is related to the redshift by

$$\frac{a(t_o)}{a(t_e)} = z + 1 = \frac{\lambda_o}{\lambda_e}. \tag{2.3}$$

Thus a photon emitted at time t_e with rest-wavelength λ_e is redshifted in proportion to changes in the scale of the universe between emission and observation. λ_0 denotes the observed wavelength at time t_o.

The relative expansion rate is called the Hubble parameter:

$$H = \frac{\dot{a}}{a}. \tag{2.4}$$

Its present value, the Hubble constant, H_0 has the unit of an inverse time. It gives the ratio of the escape velocity of cosmic objects to their relative distance. The Hubble constant is sometimes expressed as the dimensionless Hubble parameter h:

$$H_0 = 100\ h \frac{\text{km}}{\text{sMpc}}. \tag{2.5}$$

2.3 The Friedmann Equations

The Einstein field equations (2.1) can be reduced to the following two independent equations by using the Robertson-Walker metric:

$$\left(\frac{\dot{a}}{a}\right)^2 = H^2 = \frac{8\pi G}{3}\rho - \frac{kc^2}{a^2} + \frac{\Lambda}{3} \tag{2.6}$$

$$\frac{\ddot{a}}{a} = -\frac{4\pi G}{3}\left(\rho + \frac{3p}{c^2}\right) + \frac{\Lambda}{3}. \tag{2.7}$$

In these two Friedmann equations the scale factor $a(t)$ is related to the pressure p and the density ρ. Setting $\Lambda = 0$ and $k = 0$ in equation 2.6 we get the critical density

$$\rho_{cr} = \frac{3H_0^2}{8\pi G} \tag{2.8}$$

that marks the transition between a geometrically open ($\rho < \rho_{cr}$) Universe that will always expand and a closed Universe ($\rho > \rho_{cr}$) leading to gravitational collapse.

We can rewrite the Friedmann equation (eq. 2.6) as:

$$\Omega_M + \Omega_k + \Omega_\Lambda = 1 \tag{2.9}$$

with the density parameters for matter, curvature and Λ:

$$\Omega_M = \frac{8\pi G}{3H_0^2}\rho_0; \quad \Omega_k = -\frac{k}{a_0^2 H_0^2}; \quad \Omega_\Lambda = \frac{\Lambda}{3H_0^2}. \tag{2.10}$$

For $k = 0$ the Universe is flat and equation 2.9 is reduced to $\Omega_M + \Omega_\Lambda = 1$. In this case the curvature of space-time is zero, corresponding to Euclidean space.

The most recent calculation of the above parameters from microwave background measurements yields values of $H_0 = 73.2 \pm 3.2$ km s^{-1} Mpc^{-1}, $\Omega_M = 0.241 \pm 0.034$, $\Omega_k = -0.014 \pm 0.017$ and $\Omega_\Lambda = 0.716 \pm 0.055$ (Spergel et al. 2007).

2.4 Cosmological Distances

In the dynamical universe the redshift of a source is used as a measure of its distance from us. There are several ways to define distances to objects, based on size or luminosity,

all of which give identical results in Euclidean space. In a curved, expanding space-time a definition of distance as a function of redshift according to the considered situation is needed. For a proper treatment we recall that light propagates on null-geodesics ($ds = 0$). From the Robertson-Walker metric (eq. 2.2), with $d\theta = d\phi = 0$, we can write

$$\frac{cdt}{a} = \frac{dr}{\sqrt{1 - kr^2}}. \tag{2.11}$$

In the following we describe four commonly used definitions of cosmological distances, which are the comoving distance, the proper distance, the luminosity distance and the angular diameter distance.

2.4.1 Comoving Distance

The comoving distance is defined as the distance that light propagates from redshift z to the present in comoving coordinates. It is given by the corresponding integral over the radial line element:

$$\begin{aligned} D_c(z) &\equiv \int_0^t \frac{cdt}{a(t)} = \int_0^r \frac{dr}{\sqrt{1 - kr^2}} \\ &= \frac{1}{H_0} \int_0^z \frac{dz}{\sqrt{\Omega_M (1+z)^3 + (1 - \Omega_M - \Omega_\Lambda)(1+z)^2 + \Omega_\Lambda}}. \end{aligned} \tag{2.12}$$

The comoving distance measures the distance between two points along a light path defined at the present cosmological time (i.e. in comoving coordinates scaled by $a(t)$).

2.4.2 Proper Distance

The light travel distance is called proper distance. It is derived by integrating the speed of light multiplied by the cosmological time interval.

$$\begin{aligned} D_{prop}(z) &\equiv \int_0^t cdt \\ &= \frac{1}{H_0} \int_0^z \frac{dz}{(1+z)\sqrt{\Omega_M (1+z)^3 + (1 - \Omega_M - \Omega_\Lambda)(1+z)^2 + \Omega_\Lambda}}. \end{aligned} \tag{2.13}$$

The proper distance measures the distance between two points along a path defined at a constant cosmological time.

2.4.3 Luminosity Distance

If we observe a flux F from a source with a known luminosity L, the luminosity distance can be defined by

$$D_L^2 = \frac{L}{4\pi F}. \tag{2.14}$$

It is related to the proper distance by

$$D_L(z) = (1+z)\, D_{prop}(z). \tag{2.15}$$

2.4.4 Angular Diameter Distance

The angular diameter distance is defined by

$$D_A(z) \equiv \frac{\delta l}{\delta \theta}, \tag{2.16}$$

where δl is the proper length of a distant object and $\delta\theta$ is the angle that it subtends. It can be calculated from the proper or luminosity distances by

$$D_A(z) = \frac{D_{prop}(z)}{(1+z)} = \frac{D_L(z)}{(1+z)^2}. \tag{2.17}$$

The angular diameter distance plays an important role in quasar lensing studies (see Section 6.1). The luminosity distance is crucial for measuring the luminosity based on the observed flux of a source, as we will do in Chapter 4. We will use the proper distance to determine the spatial separation between two objects (Chapter 5). For the distance calculations we will use a standard ΛCDM cosmology throughout with $\Omega_{\rm m} = 0.3$, $\Omega_\Lambda = 0.7$ and $H_0 = 70\,{\rm kms}^{-1}{\rm Mpc}^{-1}$.

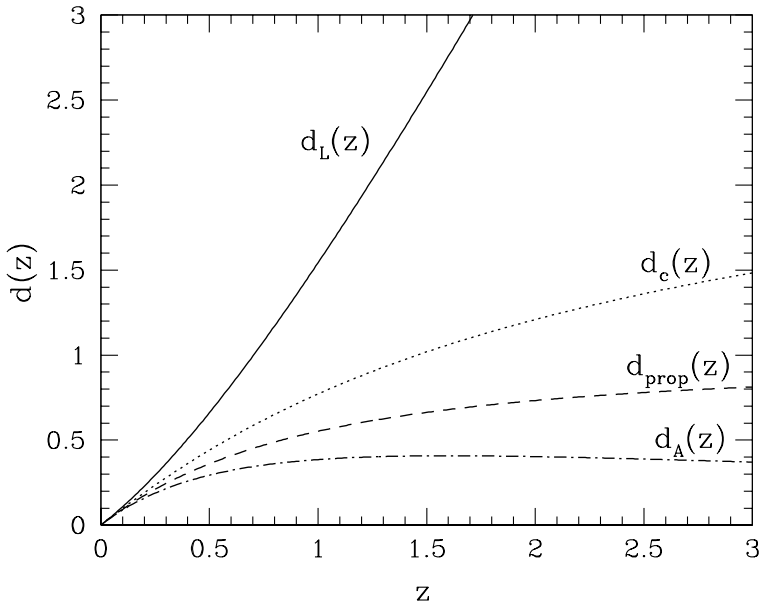

Figure 2.1: The four different distances used in cosmology (from Oguri 2004).

Part I

Quasar Light Absorption

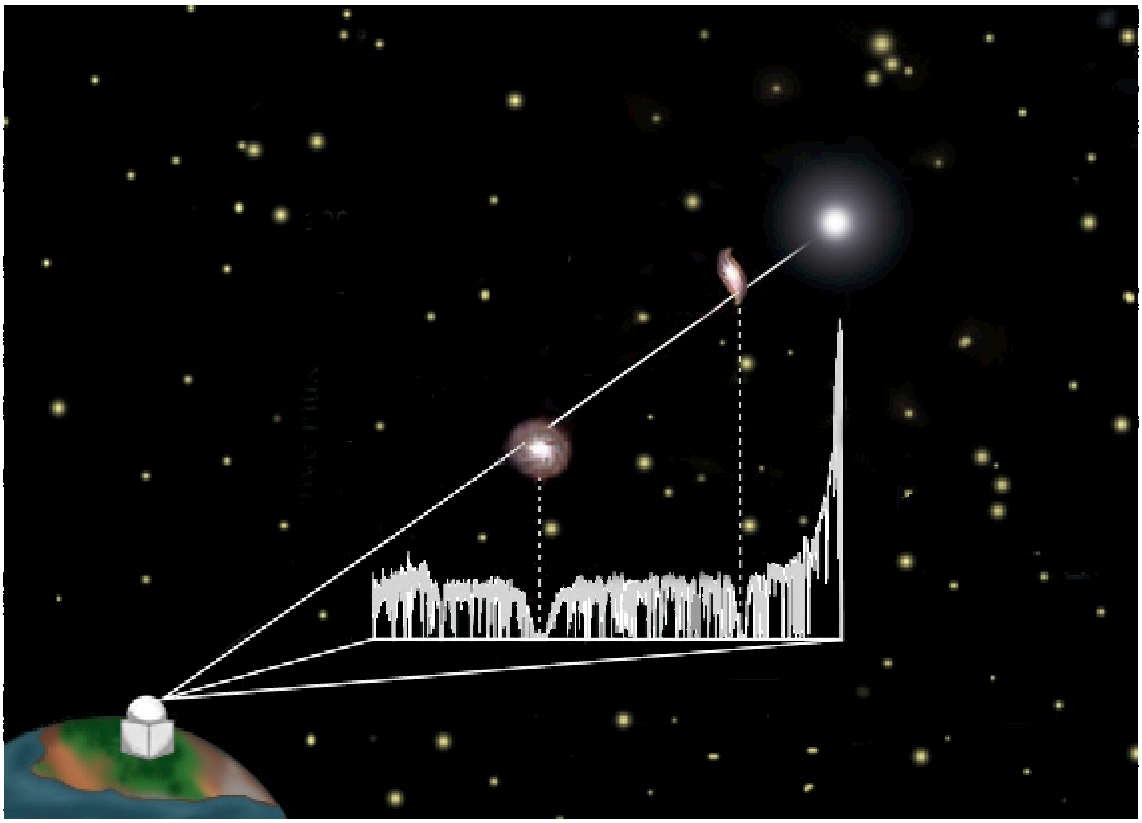

Chapter 3

The Nature of Absorption Line Systems

In a non-empty Universe the light emitted by quasars is affected by absorption along the path to the observer. Quasars probe random sight lines in the intergalactic medium that intersect with gas clouds and galaxies. Strong absorption lines viewed in the spectra of bright background quasars provide information on the distribution of neutral and ionized gas along the line of sight. The analysis of these absorption lines can reveal the metal and neutral hydrogen content of the Universe. The study of gas clouds via the information derived from absorption is a unique way to learn about their chemical composition from observations. Absorption lines from galaxies can be used to determine their physical properties such as the size and star formation rate. This allows the study of galaxy samples that are selected only by their absorption properties. In contrast to large surveys that use flux-limited samples, there is no bias towards brighter objects.

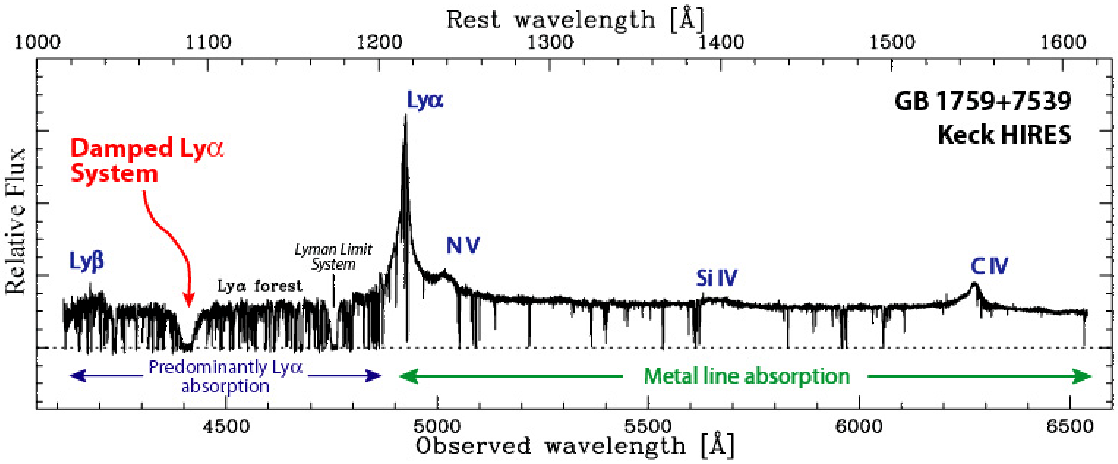

Figure 3.1: Keck HIRES spectrum of the quasar GB 1759+7539 at $z = 3.050$. Blueward of the strong Lyα emission line the Lyα forest including a Lyman limit system and a dominant damped Lyα system at z_{abs}=2.62 is seen. Redward of the strong emission line several metal absorption lines are detected (from Wolfe 2005).

Figure 3.1 shows a typical spectrum of a high redshift quasar. The spectrum is dominated by the strong Lyα emission of the quasar and several broad lines are seen redward

of this line. Many absorption lines, that are classified by their strength and the element that causes them, are seen. On the blue side of the Lyα line a number of Lyα absorbers caused by intervening H I clouds at different redshifts can be identified. There are also two broad absorption lines, a Lyman limit system and a damped Lyα system at z=2.62. On the red side of the Lyα emission a number of metal absorption lines are observed. The metal absorption lines are associated with Lyα absorbing clouds that have been enriched by metal production from stars. Other absorption lines observed in quasar spectra arise in the direct vicinity of the quasar, as in broad absorption line quasars. These absorption lines have similar redshift as the emission and are caused by gas in the central parts of the nucleus or by the quasar host galaxy. Here we will concentrate on absorption lines that are not associated with the background quasar.

Lyα absorption lines are usually categorized by the strength of the absorption. Due to the lower redshift of the absorbing source compared to the background quasar, they are always found blueward of the source Lyman-α emission line (see Figure 3.1). The following classes are selected depending on the H I column density:

- **Damped Lyman Alpha (DLA) systems** with $N(\mathrm{H\,I}) \geq 2 \times 10^{20}$ cm^{-2} are very broad absorption systems with characteristic damped wings. They have been found in the spectra of background sources like quasars and gamma ray burst afterglows. DLAs are believed to reside in either galaxies or proto-galaxies. Hydrogen is mainly neutral in damped Lyα systems, while it is ionized in all other classes of quasar absorption systems. DLAs are thus believed to dominate the neutral-gas content of the Universe, and to serve as reservoirs for star formation at high redshift (e.g. Nagamine, Springel & Hernquist 2004). Associated metal lines that are detected redward of the source Lyman-α emission have been used to trace the age-metallicity relationship and other aspects of galactic chemical evolution (Pettini 2004).
- **Sub-Damped Lyman Alpha systems** with $10^{19} < N(\mathrm{H\,I}) < 2 \times 10^{20}$ cm^{-2} are a sub-class of Lyman limit systems. They also have broad wings and show metallicities similar to DLAs. They have been introduced more recently in the literature as a separate class at the transition between Lyman limit and damped Lyman Alpha systems (Peroux et al. 2003).
- **Lyman limit systems (LLS)** have $10^{17} < N(\mathrm{H\,I}) < 2 \times 10^{20}$ cm^{-2}. They include sub-DLAs and associated metal absorption can be identified. At $N(\mathrm{H\,I}) > 10^{17}$ cm^{-2} the clouds become optically thick to radiation below 912 Å (the Lyman limit), causing a characteristic break in the spectrum.
- **Lyman alpha forest** is the name for the numerous lines observed blueward of the Lyα emission. These lines are optically thin and have low column densities of $N(\mathrm{H\,I}) < 10^{17}$ cm^{-2}. This is the most common absorption phenomenon in quasar spectra. The Lyman alpha forest traces clouds of neutral hydrogen at different redshifts along the line of sight to the quasar. Metal lines associated with these clouds can be identified.

In the next Chapters we will study two of the above Lyα absorption classes in detail. The damped Lyα system towards the quasar PKS 0458-020, which is one of the few known DLA systems where Lyα is seen in emission in the center of the broad absorption, is analyzed

in Chapter 4. Then in Chapter 5 we identify field galaxies that are responsible for Lyα absorption lines seen in the spectra of the quasar pair Q 0037-3544 and Q 0037-3545.

Chapter 4

The Damped Lyman-α System towards PKS 0458-020

The first broad damped Lyα absorption was identified in 1971 by Lowrance et al. (1971). Systematic searches for damped Lyα absorption systems in quasar spectra over the last years have increased the number of known DLAs to more than 500 (Prochaska, Herbert-Fort & Wolfe 2005). Due to the large H I column densities and the conspicuous presence of metals, DLAs are believed to arise in intervening galaxies. At low and intermediate redshifts, galaxy counterparts have been found in a number of cases (Le Brun et al. 1997, Chen & Lanzetta 2003). Although it is probable that at high redshift DLAs are associated with regions of star formation, it turns out to be difficult to detect them in emission. Despite intensive searches, very few cases have been found so far in which Lyα is seen in emission at the same redshift as the absorption (e.g. Møller & Warren 1993, Møller et al. 1998, Warren et al. 2001, Vreeswijk et al. 2004). One of these rare cases is the $z_{\rm abs} = 2.03954$ DLA system towards PKS 0458−020 where Lyα emission from the corresponding absorbing galaxy has recently been detected by Møller et al. (2004) in the center of the absorption trough. This DLA system is well known as it was one of the first to be detected in absorption in 21 cm observations (Wolfe et al. 1985).
In this Chapter, we present a new high-resolution spectrum of this quasar that allows us to discuss the kinematics of the Lyα emission line relative to the metal lines belonging to the DLA system. We measure metallicities and depletion factors. We discuss and compare two independent methods for the derivation of the star formation rate, one based on the Lyα emission line and one using the C II* absorption line. Also, we focus on the physical conditions in the DLA and investigate the absence of molecular hydrogen.

4.1 Observations and Data Reduction

The Ultraviolet and Visible Echelle Spectrograph (UVES; Dekker et al. 2000), mounted at the Nasmyth B focus of the ESO Kueyen VLT-UT 2 8.2 m telescope on Cerro Paranal in Chile, was used during three visitor mode observing runs. Dichroic beam splitters were used on October 21-23, 2000, and October 16, 2001, to observe at the same time with both spectroscopic arms. During these two runs, central wavelengths were adjusted to 437 nm in the blue arm and 570, 580 or 750 nm in the red arm. Full wavelength coverage was obtained this way between 376 and 939 nm with only a small gap between 741 and 757 nm due to the physical gap between the two red arm CCDs. The CCD pixels were

binned 2×2 and the slit widths were fixed to $1''$, yielding, under the $0\farcs6$ seeing conditions achieved during the observations, a resolving power $R \approx 53,000$. The total integration time on source was about 3.5 h. Complementary observations at wavelengths shorter than 387 nm down to the atmospheric cutoff ($\sim$ 305 nm) were obtained on October 29-30, 2003, using the blue arm of UVES in standalone together with the standard setting with central wavelength adjusted to 346 nm. During this third run, due to the faintness of the QSO the CCD pixels were binned 2×3, while the slit width again was fixed to $1''$. These additional observations amount to a total of about 3.5 h splitted into three different exposures.
The data were reduced using the latest version of the UVES pipeline (Ballester et al. 2000) which is available as a dedicated component of the ESO `MIDAS` data reduction system. The main characteristics of the pipeline are to perform a precise inter-order background subtraction for science frames and master flat-fields, and an optimal extraction with Gaussian modeling of the object spatial profile rejecting cosmic ray impacts and subtracting the sky spectrum simultaneously. The pipeline products were checked step by step. The wavelength scale of the spectra reduced by the pipeline was then converted to vacuum-heliocentric values and individual 1-D spectra were scaled, weighted and combined to produce the final science spectrum and its associated variance.

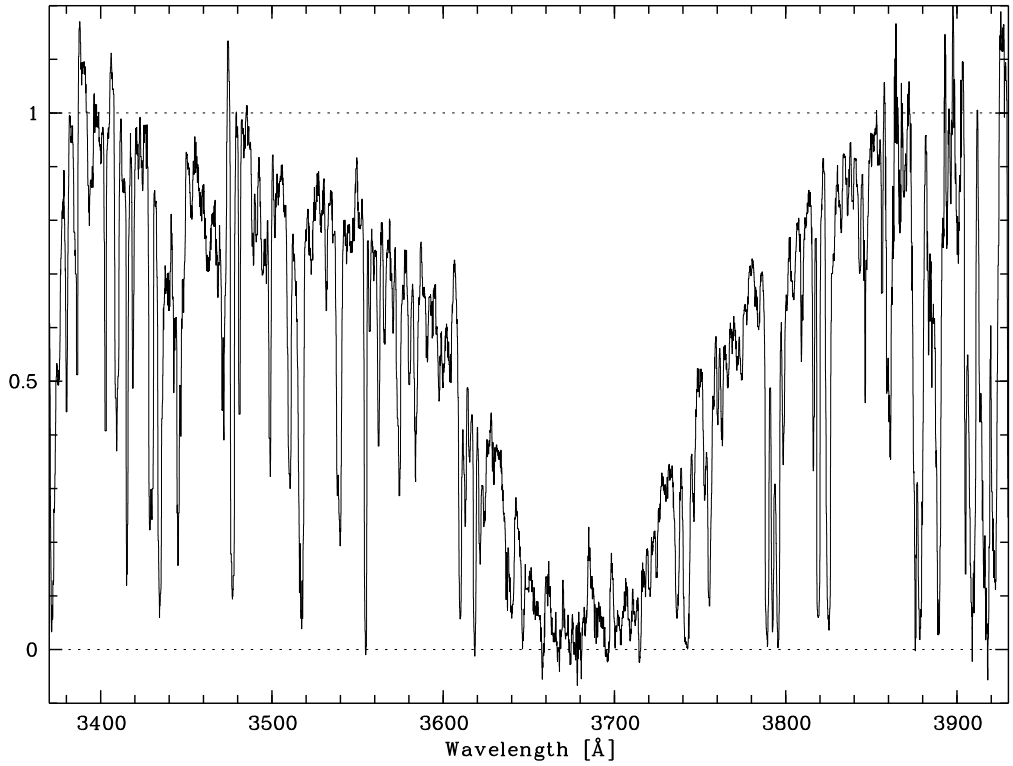

Figure 4.1: UVES spectrum of PKS 0458−020 in the wavelength interval between 3400 and 3900 Å showing the damped Lyα line with the Lyα emission line in the center. The original spectrum was smoothed with a Gaussian filter of FWHM 10 pixels. The neutral hydrogen column density of the system, obtained by Voigt profile fitting of the absorption trough, is $\log N(\mathrm{H\,I}) = 21.7$. An emission line is detected in the center of the absorption trough.

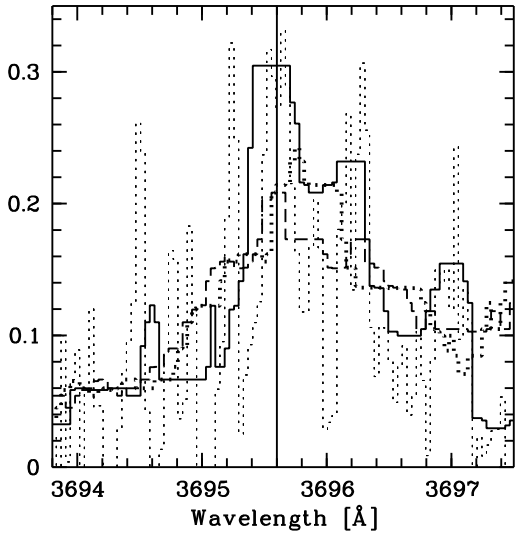

Figure 4.2: Inset of the spectrum showing the Lyα emission line centered at 3695.6 Å. The thin dotted line is the initial high-resolution spectrum. The solid, thick dotted and dashed lines show the emission line smoothed with a filter width of 5, 15 and 20 pixels respectively. Depending on the filter width the location of the peak of the emission varies by ~ 0.2 Å.

4.2 The Lyα Emission

By fitting the damped wings, we measure the column density of the damped Lyα absorption to be $\log N(\mathrm{H\,I}) = 21.7 \pm 0.1$. H I Ly$\alpha$ in emission is detected in the center of the broad absorption as can be seen in Figure 4.1. Since the emission line profile is affected by noise we applied different smoothing factors to the spectrum to measure the exact wavelength of the Lyα emission. In Figure 4.2, the initial spectrum of the Lyα emission line is shown together with the results of applying smoothing with different smoothing radii. As can be seen the position of the peak of the line slightly depends on the smoothing radius. The line is not symmetric, probably because of absorption by intervening neutral hydrogen in the blue wing. We therefore choose the peak of the line as an indicator of the mean position of the emission, 3695.6±0.2 Å (errors are estimated from the shifts due to different smoothing). This corresponds to an emission redshift of $z = 2.0400 \pm 0.0002$.
Our spectrum is not flux calibrated. We checked that the flux in the Lyα emission line relative to the continuum from the quasar is about the same as in the spectrum of Møller et al. (2004). The measured Lyα flux from Møller et al. (2004) is $F = 5.4^{+2}_{-0.8} \times 10^{-17}$ erg s^{-1} cm^{-2}. Assuming $H_0 = 70$ km s^{-1} Mpc^{-1}, $\Omega_\mathrm{M} = 0.3$ and $\Omega_\Lambda = 0.7$, the redshift $z = 2.0400$ corresponds to a luminosity distance of $d_\mathrm{L} = 15921$ Mpc. The observed flux therefore corresponds to a Lyα luminosity of $L_{\mathrm{Ly}\alpha} = 1.64 \times 10^{42}$ erg s^{-1}. Adopting the relation between the measured Lyα luminosity and the star formation rate from Kennicutt (1998), $L_{\mathrm{Ly}\alpha} = 10^{42} \times \mathrm{SFR}$, we derive a star formation rate of $\mathrm{SFR} = 1.6^{+0.6}_{-0.3}$ M$_\odot$ yr^{-1}. The Lyα emission provides only a lower limit to the SFR as the presence of dust can reduce the strength of the Lyα emission. In the following Section, we will see that the depletion factor is not small and that dust is present in the gas.

4.3 Column Densities and Metallicities

A number of metal absorption lines associated with the DLA system are detected: low-ionization species, e.g., C II*, Si II, Fe II, Cr II, Al II and Al III, and the high-ionization species C IV and Si IV. The column densities were derived via Voigt-profile fitting of the absorption lines, using for each species the different transitions present in the spectrum. Figure 4.3 and Figure 4.4 show a sample of the fitted line profiles. For the strong C II* and Si II lines, nine components are needed to reproduce the profiles. Their redshifts ($z_{\rm abs}$), column densities (log N in cm^{-2}) and turbulent broadening parameters ($b_{\rm turb}$ in km s^{-1}) are listed in Table 4.1. The components represent gas clouds associated with the DLA galaxy. The weaker lines were only detected in the two strongest components at $z_{\rm abs} = 2.03937$ and 2.03954 (labeled components 6 and 7), which are responsible for the main absorption (log N(Si II)>15.2). It is important to note that 21 cm absorptions have been reported by Wolfe et al. (1985) in these two components. Most of the neutral hydrogen is therefore probably associated with these two components. The 21 cm absorption is stronger at $z_{\rm abs} = 2.03937$ than at $z_{\rm abs} = 2.03954$ in accordance with the C II* absorption. Other species and in particular Si II show the contrary; their column densities are higher in component 7 than in component 6. Our column density determinations compare well with those of Prochaska & Wolfe (1999) except for Fe II, that we find 0.2 dex less abundant based on the Fe IIλ1611 optically thin transition.

Assuming that these two components dominate the DLA system and contain most of the neutral hydrogen, we derived the total column densities from these two components and the corresponding abundances relative to solar ([X/H] = log (X/H) − log (X/H)$_\odot$). The solar values were taken from Morton (2003). The H I column density cannot be constrained for individual components. Therefore, taking into account only the column density summed over the two strongest components of the system can introduce a systematic error in the sense that our derived metallicities could be lower limits. We can estimate the possible corresponding error by integrating the column densities for all components of Si II (Table 4.1) and comparing with the value obtained for the two strongest components (Table 4.2). In this way we derive a metallicity for silicon of [Si /H] =−1.11 instead of −1.28, which means that the metallicity of silicon could be underestimated by at most 0.17 dex.

From the values in Table 4.2, we can derive abundance ratios for different metals. In the ISM of our Galaxy, zinc and silicon are barely depleted onto dust-grains which is consistent with our observed ratio in this high redshift system of [Si II/Zn II] = −0.06. Other elements appear depleted: chromium ([Cr II/Zn II] = −0.44), iron ([Fe II/Zn II] = −0.65), phosphorus ([P II/Zn II] = −0.32) and manganese ([Mn II/Zn II] = −0.83). The depletion of iron compared to zinc is indicative of the presence of dust at a level compatible with the presence of molecular hydrogen (see Ledoux et al. 2003). The fact that molecular hydrogen is *not* detected (log $N(H_2) < 14.9$ and log $f < -6.52$) is therefore surprising, especially as the system has one of the highest H I column densities observed in DLAs (see Section 4.6).

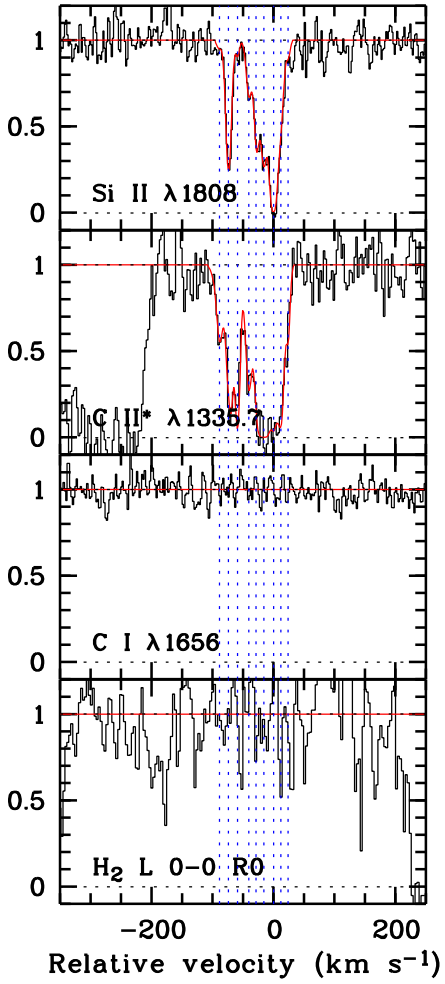

Figure 4.3: Absorption line profiles of the C II*λ1335 doublet and the Si IIλ1808 transition. Nine individual components were needed to perform the fit to the absorption lines that is overplotted to the data as a solid line. The components are indicated by vertical dashed lines. The portions of the spectrum where the C Iλ1656 and H_2L0R0 transitions are expected are also shown. The zero point of the velocity scale has been taken at $z_{\rm abs} = 2.03954$.

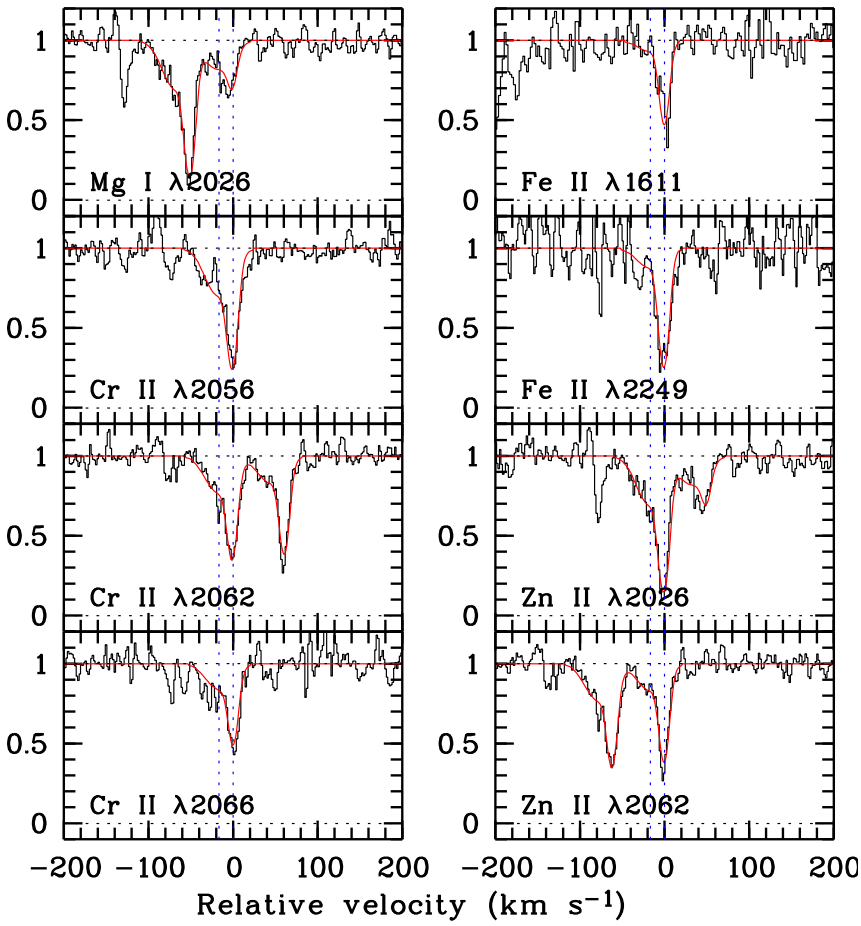

Figure 4.4: Voigt-profile fits to the Fe II, Cr II, Zn II and Mg I absorption lines. When lines are blended simultaneous fits were performed. The zero point of the velocity scale has been taken at $z_{\rm abs} = 2.03954$.

Table 4.1: Redshifts, ion column densities and turbulent broadening parameters for all components of the system

#	$z_{\rm abs}$	log N(C II*)	log N(Si II)	$b_{\rm turb}$ [km s^{-1}]
1	2.03864	13.16±0.23	< 14.37[a]	5.4±4.1
2	2.03879	13.48±0.21	15.19±0.03	4.7±0.4
3	2.03894	14.43±0.31	< 14.37[a]	~ 2.5
4	2.03913	13.55±0.15	14.65±0.10	5.2±1.8
5	2.03925	< 13.12[a]	14.99±0.10	4.3±1.4
6	2.03937	14.79±0.39	15.21±0.09	5.9±2.0
7	2.03954	13.91±0.65	15.90±0.20	5.3±0.9
8	2.03966	13.89±0.34	14.87±0.31	5.2±3.2
9	2.03978	< 13.12[a]	< 14.37[a]	2.5±4.4

[a] 5σ detection limit.

4.4 Kinematics

Figure 4.5 shows the velocity profiles of several low (C II, C II*, Si II, Fe II, Al II, Al III) and high (C IV, Si IV) ionization metal absorption lines. The zero point of the velocity scale is located at $z_{\rm abs} = 2.03954$ and corresponds to the position of the strongest Fe II and Zn II component (see Figure 4.4). We indicate in Figure 4.5 the position of the peak of the Lyα emission line as a vertical solid line ($\Delta v \approx +45$ km s^{-1}). As can be seen from the Figure the metal absorption lines are all blueshifted with respect to the Lyα emission. This is a consequence of kinematics either in the disk of a galaxy or in outflowing gas. We shall discuss both possibilities in more detail below.

4.4.1 Rotating Disk

Prochaska & Wolfe (1997) made the case that the kinematics of DLA systems can be explained by models of large rotating disks. For the most likely rapidly rotating thick disk model they found that the absorption profile should be asymmetric with the strongest absorption component located at one edge of the profile. In this model the emission originating from the central part of the disk should be offset from the absorptions. This corresponds to what we observe in the DLA towards PKS 0458−020. Indeed, the velocity profiles of all metal absorption lines are observed blueward of the Lyα emission and the strongest absorption component is located at the red edge of the profile. In addition, the Lyα emission is located outside of the absorption profile at $\Delta v = 45 \pm 16$ km s^{-1} (the uncertainty comes from the uncertainty in the redshift of the Lyα emission) redward of the strongest absorption component. If we assume that the line of sight goes through a large rotating disk and the Lyα emission originates from the center of this disk, the blueshift of the low-ionization transition lines compared to the Lyα emission can be explained by gas that takes part in the rotation of the disk and is moving towards us. The small velocity offset of the strongest absorption compared to the emission suggests that the line of sight crosses the mid-plane of the disk far from the major axis, where the projected rotational velocity is small. The impact parameter between the line of sight and the center of the disk should be small and the inclination high to ensure strong enough absorption spread over

Table 4.2: Ion column densities and metal abundances in components 6 and 7

Species	log N(X)	$\log(\mathrm{X/H})_\odot + 12$[a]	[X/H][b]
H I	21.70±0.10	...	...
H_2 (J=0)	<14.55	...	...
H_2 (J=1)	<14.60	...	...
C I	<12.45	...	...
C II*	14.84±0.35	...	...
Mg I	13.26±0.04	...	...
Mg II	16.07±0.07	7.58	−1.21±0.12
Si II	15.98±0.17	7.56	−1.28±0.20
P II	13.72±0.04	5.56	−1.54±0.11
Cr II	13.73±0.02	5.69	−1.66±0.10
Mn II	13.18±0.04	5.53	−2.05±0.11
Fe II	15.33±0.04	7.50	−1.87±0.11
Zn II	13.15±0.02	4.67	−1.22±0.10

[a] Reference abundances from Morton (2003).

[b] The given errors correspond to errors in the column densities.

more than 100 km s^{-1}. A small impact parameter between the emitting region and the line of sight was derived by Møller et al. (2004) of the order of 0.3 arcsec or 2.5 kpc. It is striking that the observed situation here corresponds to case 4 of Figure 14 in Prochaska & Wolfe (1997) and supports the case for a large rotating disk. Note that the same conclusion has been drawn from 21 cm observations by Wolfe et al. (1985). This scenario assumes that the Lyα emission line peak records the systemic velocity of the galaxy. This may not be the case as indicated by the velocity shifts usually observed between the Lyα and the [O III] emissions in Lyman break galaxies (Pettini et al. 2001) or in DLA systems (Weatherley et al. 2005).

4.4.2 Galactic Wind

On the other hand, the observed situation is also reminiscent of a wind flowing out of a star-forming region in our direction as observed in star-burst galaxies (e.g., Veilleux et al. 2005). The velocity offsets derived here for the strongest absorption components seem too small to be caused by a wind. We note that the high-ionization lines Si IV $\lambda\lambda$1393,1402 and C IV $\lambda\lambda$1548,1550 show a second broad absorption component at a projected velocity of -170 km s^{-1}. This strong feature is completely absent in the lower ionization lines. There are two possibilities to explain this high-ionization region. Either the absorption comes from a region of hot gas associated with the DLA absorber but located at the projected distance corresponding to $v = -170$ km s^{-1}, or there is hot gas moving towards us with this velocity which has been ejected by the DLA galaxy. The first explanation is unlikely as in that case the gas should be located close to the center of the galaxy for the rotation velocity to be large and should therefore be associated with less ionized gas. The observed high velocity offset component could be a heated shock front or the galactic wind itself. However, this is clear indication for a galactic outflow driven by the mechanical energy

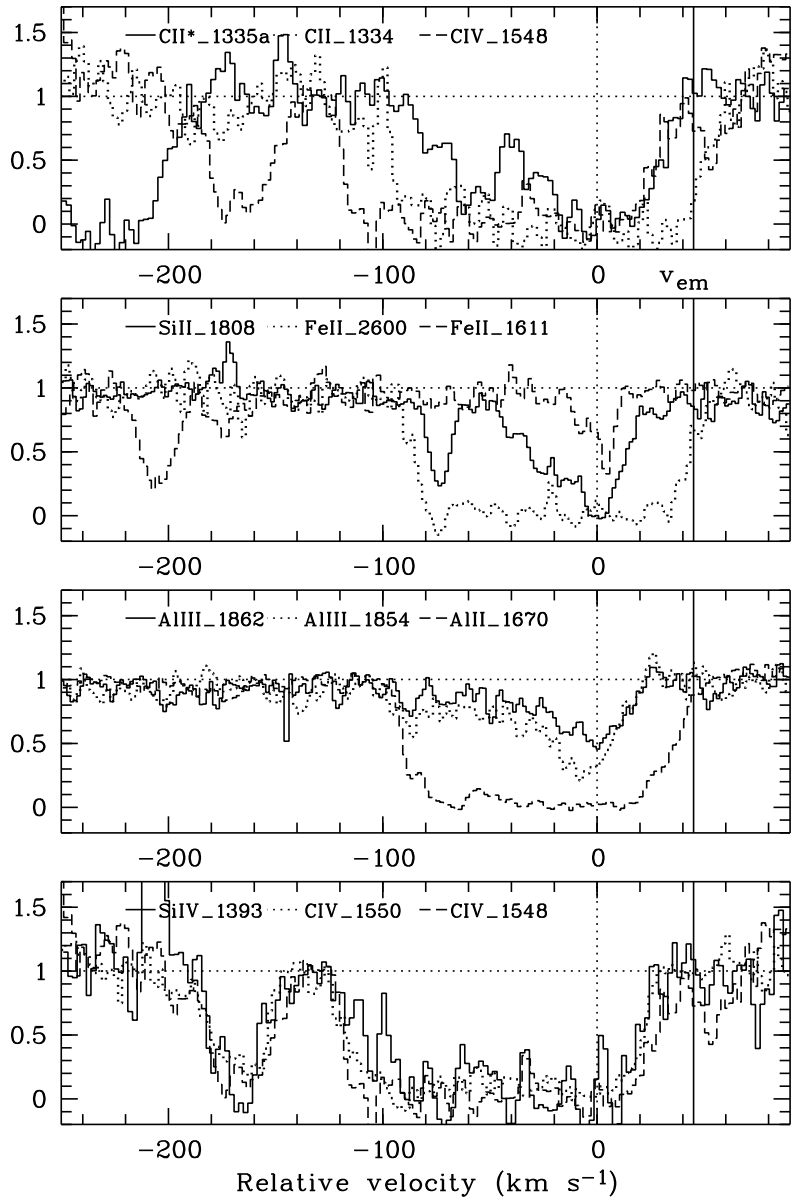

Figure 4.5: Velocity profiles of different metal absorption lines. The dashed vertical line marks the zero point derived from the Fe IIλ1611 absorption (see second panel from top). The peak of the Lyα emission indicated by the vertical black solid line is offset by about 45 km s^{-1} redward of the main absorption component. The zero point of the velocity scale has been taken at $z_{\rm abs} = 2.03954$.

deposited by supernova and stellar winds in star-forming regions.
Blueshifted absorption and redshifted Lyα emission is also seen in high-redshift spectra of UV-selected galaxies and is also interpreted to be caused by winds (see Adelberger et al., 2005, and references therein). For a sample of Lyman-break galaxies, Pettini et al. (2001) showed that the Lyα emission is redshifted by 200 to 1100 km s^{-1} relative to the position of optical emission lines (Hβ and [O III]) and that the absorptions for three-quarters of the sample are blueshifted by a median value of -300 km s^{-1}. They interpret this as the signature of strong galactic winds. In this scenario, the gas seen in absorption in front of

the stars is the approaching part of an expanding shell of swept-up material that has a very high optical depth to Lyα photons, so that the only detectable Lyα emission along the line of sight is from the back of the shell, behind the stars, receding at velocities where no foreground absorption takes place (Pettini et al. 2001). This is in agreement with the asymmetric Lyα emission line profile we observe, although the observed velocity range of $\Delta v = 120$ and 200 km s^{-1} for the low and high-ionization species respectively in the DLA towards PKS 0458−020 is smaller than the above findings. Weatherley et al. (2005) presented the detection of [O III] emission from galaxies responsible for two other damped Lyα systems. The velocity differences between the Lyα emission and the [O III] lines is about 100 km s^{-1} in both systems. Rest-frame optical emission lines are unaffected by resonant scattering and provide a better measurement of the galaxy systemic velocity. Therefore, the detection of [O III] emission lines from the galaxy in PKS 0458−020 could help to pin down the systemic velocity and to better determine the situation.
In this context, we note that the red wing of the C II* λ1335 absorption profile in Figure 4.5 follows exactly the red wing of the C IV λ1548 profile (the profile of the C II λ1334 line is broader). This implies that at least part of the C II* absorption comes from the warm gas and is closely associated with the C IV phase. This supports the conjecture that part of the gas is outflowing.

4.5 The Star Formation Rate from C II*

In Section 4.2, we obtained the SFR in the DLA from the Lyα emission line flux. Wolfe et al. (2003) proposed another technique to derive the SFR in DLA systems from the strength of the C II* absorption and the dust-to-gas ratio under the assumption that the gas in DLAs is heated by the same mechanism responsible for the heating of the ISM in the Milky Way. The authors argue that under steady-state conditions the cooling rate measured from the C II* absorption equals the heating rate per H atom, which can be used to infer the SFR per unit area $\dot{\psi}^*$. While the C II* absorption strength is measured locally along the line of sight, the derived SFR per unit area is thought to represent the mean SFR over the whole star-forming volume in the DLA.
For PKS 0458−020, Wolfe et al. (2003) derived two solutions for the SFR per unit area of $\dot{\psi}^* \approx 10^{-2}$ or 10^{-1} M$_\odot$ yr^{-1} kpc^{-2} together with a gas particle density of $\log n \approx 1.2$ or 0.3 cm^{-3} assuming that the gas where the C II* absorption occurs is respectively cold or warm. Recent revision of the UV background spectrum indicates that these SFRs could be slightly overestimated (Wolfe 2005). Note that, by combining the above values of the particle density with our measured H I column density, we can derive a characteristic length scale for the light path through the H I absorbing region of ∼0.1 or 0.8 kpc. Obviously, the physical size of the DLA galaxy is larger than this and therefore also the region over which the above mean star formation rates apply.
If the observed Lyα emitting region is the only source of heating, then we can derive the size of the heated region by equating the SFR from the Lyα emission to that derived from C II*. This size should be of the order of $R = 7.2$ or 2.3 kpc, respectively for the cold or warm gas, in order for the two SFR estimates to match. Note that this size is probably smaller than the total size of the H I disk, $R_{\rm disk}$. In the following, we try to estimate R. The first estimate can be obtained by assuming that the impact parameter between the Lyα emitting region and the line of sight corresponds to a lower limit of R. Møller et al. 2004 estimate this impact parameter to be $b_{\rm DLA} = 0\farcs3 \pm 0\farcs3$. Assuming the above cosmology (see Sect. 4.2), a redshift of $z = 2.04$ corresponds to an angular diameter

distance to the DLA of 1723 Mpc, so that the angle of 0.″3 corresponds to a proper size of 2.5 kpc. This value coincides with the above solution if the gas is warm. For the cold gas solution, this rather small value can be explained by the fact that the measured impact parameter can lie anywhere in the range $[0; R_{\rm disk}]$[1].
Another estimate of R can be derived by using high-resolution radio interferometry observations in front of the extended PKS 0458−020 radio source. Briggs et al. (1989) probed several different paths through the absorbing medium and concluded that the absorber is a disk-like structure that extends across 2″. This corresponds to a radius of $R_{\rm disk} = 8.4$ kpc. The disk should be oriented in the same direction as the radio source, and therefore in the South-Western direction, whereas the Lyα emitting region is in the North-Western direction. This is consistent, as are the kinematics, with the existence of an inclined large disk with its center at the location of the emitting region. Therefore a large value of R is not incompatible with this model.
On this basis alone, it is therefore difficult to decide whether the gas is cold or warm. Another way of looking at this problem is to estimate the mean UV flux along the line of sight.

4.6 Missing Molecules

Molecular hydrogen is not detected in our spectrum down to a limit of $\log N(\mathrm{H_2}) = 14.9$, corresponding to a molecular fraction ($f = 2\mathrm{N(H_2)}/[2\mathrm{N(H_2)} + \mathrm{N(H\,I)}]$) of $\log f = -6.52$. The absence of molecules is surprising at such a high H I column density ($\log N(\mathrm{H\,I}) = 21.7$). As the gas is probably dusty with a depletion factor of [Zn/Fe] = 0.65, this could be a consequence of high temperature and/or high UV background radiation.
The temperature of the gas can be estimated from the spin temperature. Absorption at 21 cm was reported in two components at the same redshifts as our components 6 and 7 (Wolfe et al. 1985; see Table 4.1). Combining the 21 cm absorption with the H I column density, Wolfe et al. (1985) estimated the spin temperature of the gas to be less than 1000 K. Kanekar & Chengalur (2003) corrected this value to $T_{\rm S} \sim 385\pm100$ K. This is unusually low for a DLA system and is in the range of Galactic values (<350 K; Braun & Walterbos 1992).
The integrated 21 cm optical depth of component 6 is about four times larger than that of component 7 in accordance with what is seen for the C II* absorption. It is however apparent that the metal column densities are smaller in component 6 (see Figure 4.5); the Si II column density is for example five times smaller in component 6 than in component 7. On the basis of this inverted ratio, if we assume similar physical conditions (metallicity and ionization factor) in both components, then the H I column density is smaller in component 6 than in component 7 by a factor of five and the spin temperature is smaller by a factor of twenty. Conversely, assuming a similar temperature would lead to a metallicity ten times smaller in component 6 which would be at odds with the high homogeneity of the gas usually seen in DLA systems (see Rodriguez et al. 2005). The above temperature of 385 K is the harmonic mean between the temperatures in the two components weighted by the H I column densities. Given the above ratio, we conclude that the spin temperatures of components 6 and 7 are of the order of 2000 and 100 K respectively.

[1] Møller et al. (2004) also give a firm upper limit for the impact parameter of $b_{\rm DLA} = 0.''8$, by which the object would fall outside the slit in their observations. This value corresponds to a proper size of 6.7 kpc

Using the SFR from the Lyα emission and the relation between SFR and UV flux, SFR $= L_{\rm UV} \times 1.4 \times 10^{-28}$ (Kennicutt et al. 1998), we derive a specific UV luminosity of $L_{\rm UV} = 1.14 \times 10^{28}$ erg s^{-1} Hz^{-1} in the frequency range between 1500 and 2800 Å. This luminosity corresponds to a UV flux of $F_{\rm UV} = 1.53 \times 10^{-17}$ erg s^{-1} cm^{-2} Hz^{-1} if we assume that the distance to the absorbing gas is given by the impact parameter. The resulting flux is ten times larger than the UV flux measured in the ISM of our Galaxy ($F_{\rm UVgal} = 1.47 \times 10^{-18}$ erg s^{-1} cm^{-2} Hz^{-1} following the fit in Appendix 1 of Pequignot & Aldrovandi (1986)). Therefore, the absence of molecular hydrogen is not surprising even though at least part of the gas is at low temperature and the depletion factor is not small ([Zn/Fe] = 0.65), indicating that dust is present in the gas. As shown by the models of Srianand et al. (2005), the absence of H_2 can be explained as the consequence of the high radiation field.
Note that this is consistent with the high mean ambient UV flux derived by Wolfe et al. (2004; >19.1 times the Galactic value).

4.7 Conclusions

We have presented the high-resolution spectrum of the strong damped Lyα absorber at $z_{\rm abs} = 2.03954$ in front of PKS 0458−020. It is one of the rare systems where Lyα is clearly seen in emission with an impact parameter between the emitting region and the line of sight of ∼0.3 arcsec (Møller et al. 2004) or 2.5 kpc using the adopted concordance cosmology. We determined the redshift of the Lyα emission line to be $z = 2.0400 \pm 0.0002$. The metal absorption lines are found to be blueshifted compared to the Lyα emission and to span a velocity range of $\Delta v = 120$ and 200 km s^{-1} for the low and high-ionization species respectively. The kinematics, together with the observations in 21 cm by Briggs et al. (1989), are strikingly consistent with the model of a large rotating disk presented by Prochaska & Wolfe (1997), in which the line of sight crosses the mid-plane far from the center of the disk but keeps a low impact parameter with the center of the disk. Conversely, the coincidence of the red wings of the C IV and C II* profiles and the extent of the C IV absorption argues for the presence of blueshifted warm gas, which may possibly be part of an outflow from the DLA galaxy. If true, the velocity of such outflows is much smaller than is observed in star-burst galaxies (see Veilleux et al. 2005). A possible detection of rest-frame optical emission lines could help to support the model of a large rotating disk. We derived column densities and metallicities for a number of species. The DLA absorber corresponds to a two-phase medium with warm and cold gas. We were able to compare the star formation rate derived from the Lyα emission line with the derivation from the C II* method in the same object. From the Lyα emission, we find a star formation rate of SFR $= 1.6^{+0.6}_{-0.3}$ M$_\odot$ yr^{-1}. From the C II* column density, Wolfe et al. (2003) derived a SFR per unit area of 10^{-2} and 10^{-1} M$_\odot$ yr^{-1} kpc^{-2} for cold and warm gas respectively. This means that the diffuse gas should be extended over a radius of ∼7.2 or 2.3 kpc respectively for both SFRs to match.
The absence of molecular hydrogen to a limit of $\log f = -6.52$ can be explained as a consequence of the high radiation field in the disk due to star formation. The ambient UV flux due to the observed emitting region is one order of magnitude larger than the flux in our Galaxy.

The results described in this Chapter have been published in Astronomy & Astrophysics as Heinmüller et al. 2006.

Chapter 5

Galaxy-Absorber Correlation in the Field of the Quasar Pair Q 0037-3544 and Q 0037-3545

Lyα absorbers that are seen at various redshifts in quasar spectra contain precious information on the physical state and the spatial distribution of the neutral hydrogen in the Universe. The strongest lines in the Lyα forest have been found to be associated with galaxies (Lanzetta et al. 1995, Le Brun et al. 1996, Chen et al. 2001), or groups or clusters of galaxies. The corresponding radius of the galactic gaseous halos is of the order of 200 kpc. This is not surprising since if there is gas in the intergalactic medium, the density of this gas is expected to be higher in the vicinity of the galactic potential wells. The case for the weak lines ($W_{\rm r} < 0.2$ Å) to be associated with galaxies is less clear. Tripp et al. (1998) have shown that at $z \sim 0.15$ all galaxies within a projected distance to the quasar line-of-sight of 600 kpc are associated with Lyα absorbers at less than $\Delta v = 1000$ kms^{-1} in redshift (the majority being at $\Delta v < 350$ kms^{-1}). In addition, the two-point correlation function of the absorption lines shows marginal evidence for clustering on 500 kpc scales in the case that the weakest lines are excluded.

Studies of the transverse correlation in the Lyα forest using several lines of sight can reveal the spatial extent of the absorbing structures. Multiple images of lensed quasars with separations of a few arcseconds imply that the absorbing structures have sizes > 50 kpc. Observations of pairs or groups of quasars have shown that Lyα complexes extend over hundreds of kpc (Petitjean et al. 1998) up to cluster-like sizes of the order of 1 Mpc (Young et al. 2001). Williger et al. (2000) even found evidence for an excess of clustering on 10 Mpc scales. The latter observation is confirmed by the recent determination of the transverse correlation function from QSO pairs (Coppolani et al. 2006).

All this means that the diffuse gas in the intergalactic medium traces well the large scale structures of dark matter, characterized by filaments, sheets and voids. Part of the gas is located inside dark matter filaments where star formation can occur very early in small halos that subsequently merge to build up galaxies. This gas is correlated with galaxies, and metal lines arising in the gas can be observed.

A way to accurately reconstruct the density field is to use the complementary knowledge of the spatial distribution of the gas along adjacent lines of sight and the spatial distribution of galaxies in the field (e.g. Pichon et al. 2001). Intermediate redshift ($z \sim 1$) is an ideal place for this experiment as the Lyα forest is still dense but much less than at

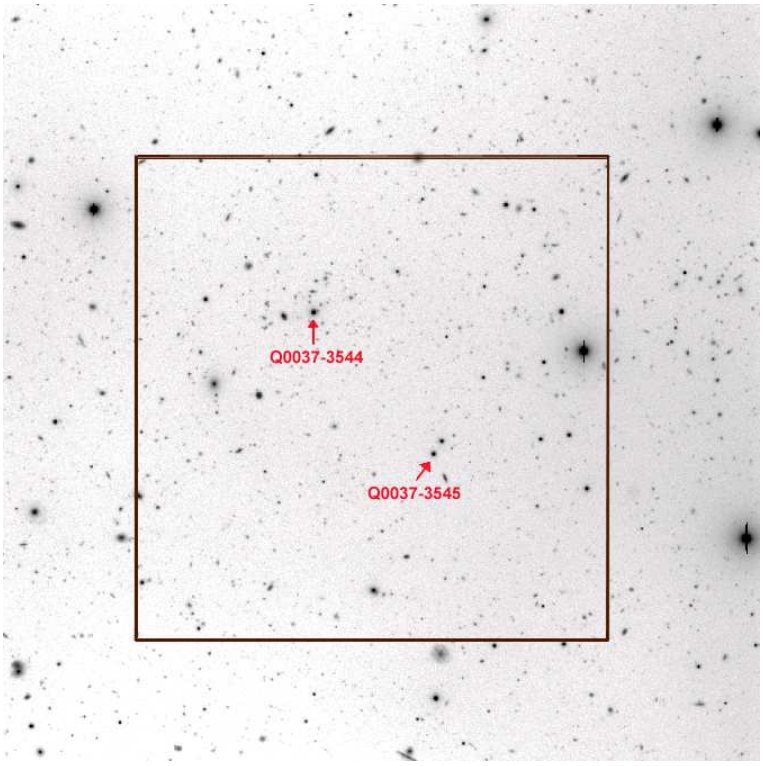

Figure 5.1: Field around the quasar pair Q 0037-3544 and Q 0037-3545. The whole field of view is $6.'8 \times 6.'8$. The inner box marks the smaller $5' \times 5'$ field of view of the H and Ks images.

higher redshift, so that blending effects and chance coincidences have little impact on the results. Well developed galaxies are in place and easy to detect. This is also the redshift range where it seems that galaxies experience strong evolution in their star-formation rate. However, as the Lyα lines are redshifted into the optical for $z > 1.7$, quasar pairs with redshifts $z \sim 1$ have to be observed with the Hubble Space Telescope.
Aracil et al. (2002) used high resolution HST-STIS spectra to study absorbers at $z \leq 1$ along the lines of sight towards four quasar pairs with image separations of 2-3 arcmin. In order to search for a possible correlation caused by the extent or the clustering properties of the structures traced by absorption lines, the distribution of velocity differences between nearest neighbor H I Lyα absorption lines detected in the spectra was analyzed.

One of the fields, including the pair Q 0037-3544 and Q 0037-3545, was chosen to perform an imaging survey in order to correlate the redshift distribution of galaxies in the field with the absorptions along the lines of sight. We obtained deep images of the field in the B, V, R, I-band with FORS1 and H and Ks-bands with SOFI. This quasar pair is also a known X-ray and radio source (Voges et al. 1999, Condon et al. 1998). The angular separation of the pair is $1.'7$. It has been chosen because the separation probes the transition between huge halos and filamentary structures. This gives us the unique opportunity to study the connection between the intergalactic gas and the field galaxies at intermediate redshift.
We describe the observations and data reduction in Section 5.1 and build a photometric redshift catalog of all galaxies in the field in Section 5.2. Correlations between the previously found absorption lines and the distribution of the galaxies are discussed in Section 5.3. Conclusions are drawn in Section 5.4.

5.1 Observations and Data Reduction

The field around the quasar pair Q 0037-3544 and Q 0037-3545 was observed with FORS1 at the VLT U1 telescope on August 28 and 29 in 2003 in the R and B band, and on September 25 in the V and I band. The total exposure times were 3000s, 3000s, 2400s and 6000s in the B, V, R and I filter, respectively. The field of view of these images is $6.'8 \times 6.'8$ with a pixel scale of $0.''2$/pixel. H and Ks frames were obtained on October 18 and 19 in 1999 with SOFI at the ESO-NTT with a field of view of $5' \times 5'$ and a pixel scale of $0.''29$/pixel. The total exposure times were 900s and 1800s for the H and Ks filter respectively. The $6.'8 \times 6.'8$ FORS1-field around the quasar pair is shown in Figure 5.1. The inner box marks the smaller field of view of the SOFI images (H and Ks filters). The frames were stacked for better image quality. The data reduction, including bias subtraction and flatfielding was performed using an automatic reduction pipeline.

Table 5.1: Characteristics of the observed quasar pair.

Name	RA	DEC	z	$\Delta\theta^a$
Q 0037-3544	00 39 42.5	-35 28 00	0.84	1.7
Q 0037-3545	00 39 37.2	-35 29 17	1.10	

[a] Angular separation of the quasar pair in arcmin.

5.2 Photometric Redshift Catalogue

For our analysis we first combined background subtracted frames of all available filters into one composite imaged. This image was used as reference frame to generate a reference catalogue for the object detection. Using the `SExtractor` software (Bertin & Arnouts 1996) we detected more than 3500 objects in the reference composite image and determined their coordinates. Given the coordinates for each object in this reference catalog, the photometry for each filter was performed in the following way. Within a search radius of one pixel the isophotal magnitude of the nearest neighbour to the coordinate entry in the reference catalog was determined in the corresponding image. For the H and Ks images the coordinates had to be rescaled due to the different pixel size and field of view of the SOFI instrument compared to the FORS1 field of view. This was done by using stars that are seen in the optical and in the infrared as reference points.
For the magnitude calibration in the B, V, R and I band we used the photometric standard stars in the fields of PG 2213-006, PG 0231+051 and Mark A (Landolt 1992). The fields containing the standard stars were observed under the same conditions during the observing runs. The H and Ks band magnitude calibration is based on the HST faint standards NIC_S294−D, NIC_S361−D and NIC_S677−D (Persson et al. 1998), that were also observed between the target exposures. If we define the limiting magnitude as the magnitude at which 50% of all galaxies are detected (see Figure 5.2), we derive values of 26.1, 25.8, 25.4, 24.5, 20.9 and 19.9 for the B, V, R, I, H and Ks filters respectively. The magnitude errors derived from `SExtractor` range between Δmag = 0.01 and Δmag = 0.3 in the optical and Δmag = 0.06 and Δmag = 0.5 in the H and Ks bands. The analysis is performed only in the inner field (see Figure 5.1), where we have photometric information in all 6 filters.

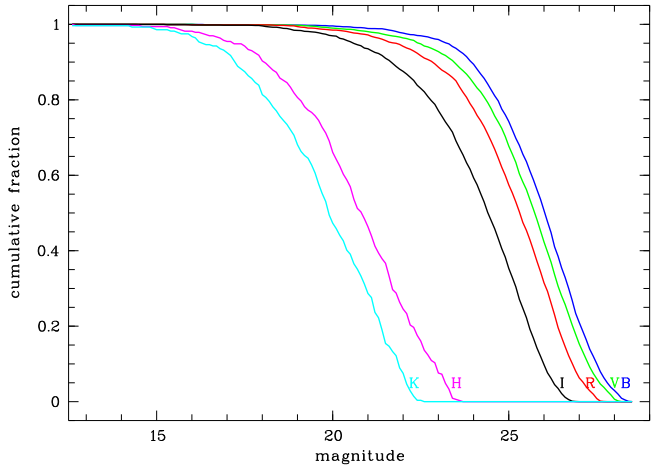

Figure 5.2: Cumulative fraction of field galaxies versus apparent magnitude. We define the magnitude at which the detection drops to 50% as the limiting magnitude for the corresponding filter.

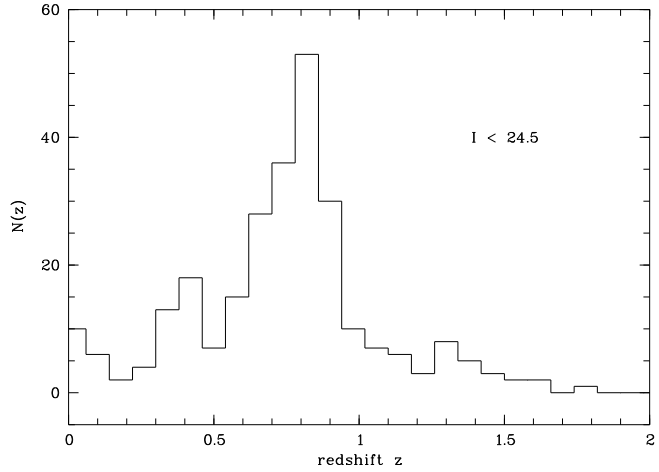

Figure 5.3: Photometric redshift distribution of the field galaxies for I<24.5.

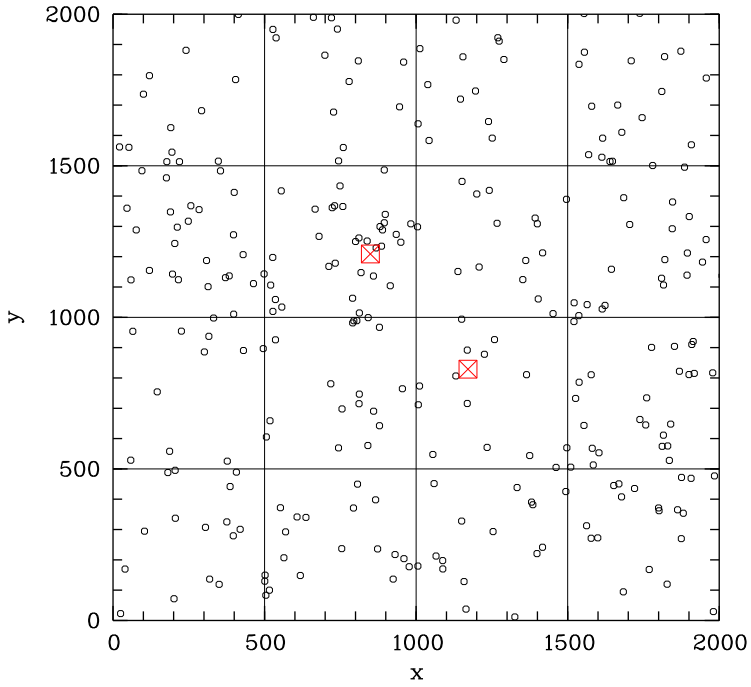

Figure 5.4: Spatial distribution of galaxies with photometric redshifts between $0.59 \leq z \leq 0.84$. The crossed squares mark the positions of the quasar pair Q 0037-3544 (upper left) and Q 0037-3544 (lower right). The box size of the overlaid grid corresponds to $1.'7 \times 1.'7$. An overdensity of galaxies in the above redshift range around the quasar Q 0037-3544 is seen.

Using the obtained photometry in six bands we are able to compute photometric redshifts of the field galaxies around the quasar pair Q 0037-3544 and Q 0037-3545. For this purpose we used the publicly available software `Hyperz`[1] (Bolzonella et al. 2000). `Hyperz` uses the multi-band photometric data of a galaxy to derive its most likely redshift by fitting the spectral energy distribution (SED) to galaxy template spectra based on the Bruzual & Charlot (1993) evolution models.
The resulting density for all field galaxies with I< 24.5 as a function of photometric redshift is shown in Figure 5.3. The median value of the redshift distribution is 0.76. We excluded catastrophic errors by demanding the redshift accuracy fulfils $\Delta z/(1+z) < 0.3$. By using six wavebands we derive a median error for the individual redshifts of the field galaxies of $\Delta z = 0.13$. We find a strong peak in the density of field galaxies at z$\sim$0.8. Table A.1 in the appendix lists the photometry and redshifts for the galaxies in our sample.

[1] http://webast.ast.obs-mip.fr/hyperz/

5.3 The Galaxy - Absorber Correlation

The quasars were observed spectroscopically by HST-STIS in June 2000 (Aracil et al. 2002). The line lists for all identified absorption systems of the quasar pair are given in Table 5.2. In the STIS spectrum of Q 0037-3544 several Lyα absorption lines have been discovered in the wing of the Lyα emission, corresponding to absorbers in the direct vicinity of the quasar. Coinciding absorption lines are observed at the same redshift along the line of sight to Q 0037–3545, about 1.′7 away from Q 0037–3544 (see Table 5.2). This indicates the presence at the redshift of the forground quasar of a gaseous structure of spatial extension larger than 700kpc.
Absorption line systems were identified in the redshift range common to both lines of sight between $z = 0.59$ and the emission redshift of Q 0037–3544 at $z = 0.84$. In Figure 5.4 we plot the spatial distribution of all galaxies in the field with photometric redshifts in this range ($0.59 \leq z_{\rm abs} \leq 0.84$). The crossed squares mark the positions of the two quasars. Around the quasar Q 0037-3544 an overdensity of galaxies is seen. To quantify this the frame was divided into a grid with boxes of 500×500 pixel side length corresponding to an angular separation of 1.′7×1.′7 (760 kpc×760 kpc at the probed redshift z ≈ 0.8). The mean number of galaxies in the above photometric redshift range is 17 per grid. In the grid around the quasar Q 0037-3544 the density of field galaxies is more than 2σ higher ($N_{gal} = 34$). Figure 5.5 shows $1' \times 1'$ zooms on the surroundings of the two quasars. The measured photometric redshifts of field galaxies are indicated, as well as proper distance radii in kpc at z = 0.8.

Table 5.2: Line list for the pair Q 0037-3544 and Q 0037-3545 from Aracil et al. (2002).

	Q0037-3544					Q0037-3545			
	$\lambda_{\rm obs}$ (Å)	$w_{\rm obs}$ (Å)	Ident.	z		$\lambda_{\rm obs}$ (Å)	$w_{\rm obs}$ (Å)	Ident.	z
1	1883.72	1.09	Lyβ	0.83648					
2	1935.63	2.47	Lyα	0.59223					
					1	2083.05	1.53	Lyα	0.71350
3	2098.4:	1.83							
					2	2142.95	0.76	Lyα	0.76277
4	2154.10	0.83	Lyα	0.77194					
5	2169.85	0.65	Lyα	0.78490					
6	2193.01	1.07	Lyα	0.80395					
7	2213.46	0.49	SiIII1206	0.83461					
					3	2214.50	1.38	Lyα	0.82163
8	2219.40	1.41	SiIV1393	0.59239					
9	2231.31	1.47	Lyα	0.83546					
			SiIV1402	0.59065					
					4	2293.83	1.10	Lyα	0.88689
					5	2318.05	1.25	Lyα	0.90681
					6	2344.75	1.06	FeII2344	0.00000
					7	2362.94	1.08	Lyα	0.94373
10	2383.35	0.55	FeII2382	0.00000	8	2383.15	0.78	FeII2382	0.00000
					9	2451.91	2.01	Lyα	1.01692
11	2464.69	0.91	CIV1548	0.59198					
			CIV1550	0.59198	10	2497.98	0.54	Lyα	1.05482
					11	2515.90	0.90	Lyα	1.06956
					12	2574.68	0.69	...	...
12	2600.73	1.13	FeII2600	0.00000	13	2601.22	0.68	FeII2600	0.00000
13	2626.04	0.75	CIV1548	0.69620					
14	2630.09	0.44	CIV1550	0.69599					
15	2796.30	1.06	MgII2796	0.00000	14	2796.31	0.53	MgII2796	0.00000
16	2803.14	0.95	MgII2803	0.00000	15	2802.46	1.06	MgII2803	0.00000
17	2843.13	0.54	CIV1548	0.83642					
			CIV1550	0.83642					

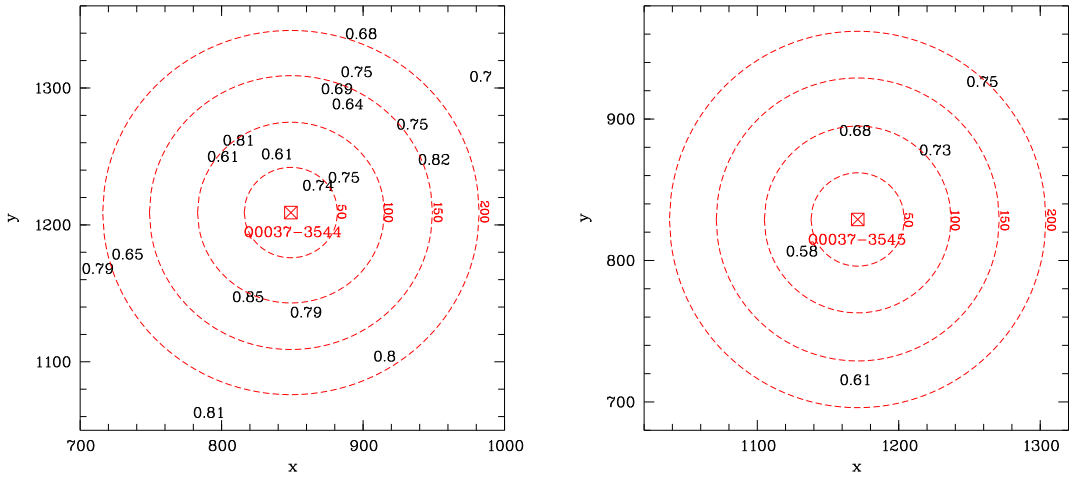

Figure 5.5: Inset on the fields around the quasar Q 0037-3544 at redshift $z = 0.84$ (left) and the quasar Q 0037-3545 at redshift $z = 1.10$ (right). The positions of the galaxies are marked by their photometric redshifts. Several galaxies at the redshift of absorption lines are detected. The field of view is $1' \times 1'$. The circles mark proper distance radii in kpc at z = 0.8.

In the following we refer to Q 0037-3544 at redshift $z = 0.84$ as the foreground and to Q 0037-3545 at $z = 1.10$ as the background quasar. Several absorptions at various redshifts have been detected. In this Section we comment on the absorption systems identified in the spectra and compare them with the photometric redshifts of our field galaxies.

5.3.1 $z_{abs} = 0.84$

This is also the redshift of the foreground quasar. Associated Lyα, Si IIIλ1206 and C IV absorptions are observed in the spectrum, as well as a feature at the position of Si IIλ1206. Lyα absorption is also detected at the same redshift in the spectrum of the background quasar. In the field around the foreground quasar several galaxies with similiar redshifts are detected $\gtrsim 100$ kpc away from the quasar (see Figure 5.5 left).
The detected metal absorption lines towards Q 0037-3544 indicate that the gas is warm and ionized because there is C IV. We find evidence for an overdensity of galaxies in the field. There is no detection of O VI absorption as expected from hot gas. For a sub-damped Lyα system at z_{abs}=2.65618 Fox et al. (2007) found the absorption profiles of O VI and C IV to be different. They concluded that the two ions trace different temperature regions of a multiphase structure.

5.3.2 $z_{abs} = 0.77$

There are a number of Lyα lines in both spectra around this redshift. A number of field galaxies at the same redshift are identified (see Figure5.5). The redshift distribution of all field galaxies (see Figure 5.4) shows an excess at $z \sim 0.8$.

5.3.3 $z_{abs} = 0.69$

There is a C IV doublet detected at this redshift in the foreground quasar. Few galaxies with this redshift are observed in the field although a possible candidate ($z_{phot} = 0.74$) is located within 50 kpc of the line of sight. No metal absorption line along the line of sight

to the background quasar has been found although the photometric redshift determination shows evidence for at least one field galaxy with corresponding redshift at a distance of 100kpc.

5.3.4 $z_{abs} = 0.59$

In the foreground quasar strong Lyα and C IV absorption lines are detected, as well as Si IVλ1393,1402. There is no corresponding absorption identified in the background quasar. Two field galaxies within a radius of $\lesssim 100$ kpc have similiar redshift. There is also evidence for one galaxy at this redshift about 70 kpc away from the background quasar.

5.4 Conclusions

The presented photometric redshifts of galaxies in the field around the quasar pair Q 0037-3544 and Q 0037-3545 together with the previously observed absorptions along the line of sight in the HST spectra allow us to study the spatial structure in front of the quasars. We find a number of galaxies at redshifts corresponding to the absorbers. We have discovered a high concentration of galaxies around the quasar Q 0037-3544, for which several Lyα and metal absorption lines have been detected by Aracil et al. (2002). If this implies the presence of a cluster we would expect to observe O VI absorption by warm gas, which was not identified in the spectrum. No extended X-ray emission around the quasar, characteristic for clusters, has been observed with Chandra. Furthermore, clusters are known to extend to scales of $\sim$1 Mpc (e.g. Fassbender et al. 2008), larger than the scale observed here. This argues against the interpretation that the observed overdensity is a cluster. It is probable that we have discovered a large scale filament-like structure that would be worth confirming with follow-up spectroscopy.
The field around Q 0037-3545 seems less populated by galaxies in the studied redshift range, which is in agreement with the absence of detectable metal absorption line systems along the line of sight. The few galaxies in the field of Q 0037-3545 nevertheless have redshifts corresponding to Lyα absorbers along both quasar sight lines. The results indicate that the absorbing structures extend over a distance of 760 kpc. We note that the accuracy of our photometric redshift measurements ($\Delta z \approx 0.13$) is too low to draw final conclusions.
We measure the photometric redshift of one field galaxy in the vicinity of Q 0037-3544 to be similiar to the observed metal absorption at $z = 0.59$. This might imply a large ($<$70 kpc) gaseous halo around the galaxy, but spectroscopic redshift confirmation is needed.

Part II

Quasar Light Deflection

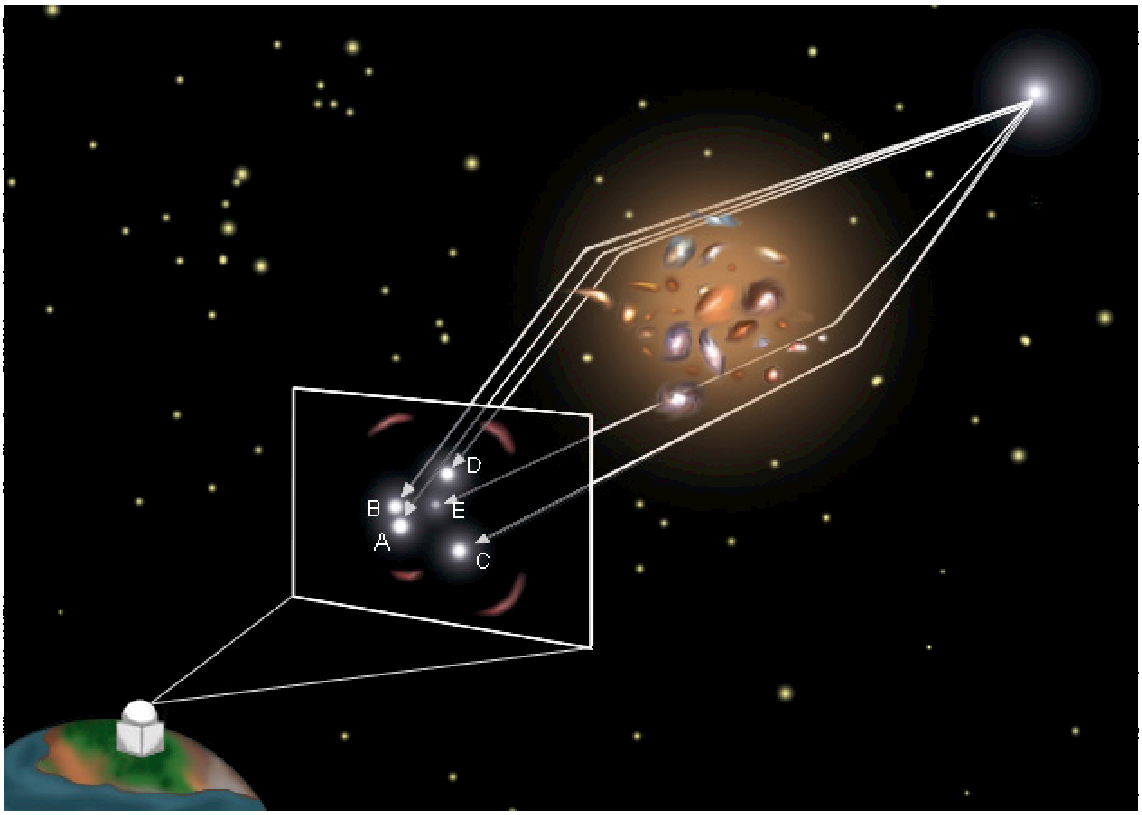

Chapter 6

Introduction

In Figure 6.1 the typical strong lensing situation, where the light emitted by a distant quasar is bent by an intervening galaxy or galaxy cluster acting as a lens, is illustrated. As a result multiple images of the source quasar can be observed. The propagation time from the source to the observer differs for each image (due to the geometry and lens potential). When the source varies in brightness, the variations appear in the images at different times, separated by the time delays. The distances between the observer, lens and source depend on the Hubble constant. In 1964 Refsdal concluded that if the image separation and the time delay could be measured, the lens mass could be modeled and the Hubble constant could be determined (Refsdal 1964).
When one of the light paths to a quasar image intersects a region of a high number density of stars, these stars act as microlenses and split the macro image into micro images (Figure 6.1). The micro images have separations of microarcseconds and therefore are not resolvable, but due to relative motion between the source and the stars, brightness variations caused by microlensing can be observed. In 1989, the microlensing effect was first detected as uncorrelated brightness variations in the four images of the lensed quasar Q 2237+0305 (Irwin et al. 1989).
The first gravitationally lensed quasar, Q 0957+561, was discovered in 1979 by Walsh, Carswell & Weymann (1979). Up to the present day, more than 100 lensed quasars are known. A list with their most important parameters can be found on the `CASTLES` survey web page[1] (Kochanek et al. 1999). About 60 of them are doubly imaged and about one third are quadruply imaged. There are few systems known that show 3, or more than 4 images. In about 15 cases a circular image, called Einstein ring, is observed. In 80 systems the source redshifts z_s are measured, and 64 have a measured lens redshifts z_L. Only 60 sources have both redshift determinations, and there are still 13 cases that have no redshift measurement at all.
Figure 6.2 shows the distribution of the lenses in image separation (using either twice the mean distance of the images from the lens or the image separation). The observed distribution combines both the true separation distribution and selection effects. Most systems have a separation of less than $5''$, which is the typical image separation caused by a galaxy acting as a lens. So far, there are only four objects known that have a separation larger than $5''$. The cutoff at small separations ($< 1''$) is due to the finite resolution of lens surveys. Towards higher separations the lensing efficiency of clusters relative to galaxies is lower. Depending on the density profile of lensing halos, gravitational lens statistical

[1] http://www.cfa.harvard.edu/castles

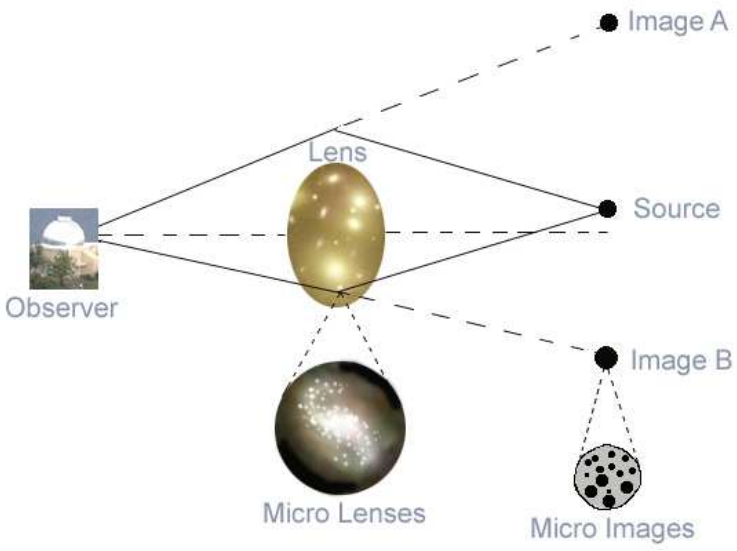

Figure 6.1: Sketch of a gravitational lens situation. The lens along the line of sight from the observer produces multiple images of the source.

theory predicts a stronger tail at larger image separations than is observed (Takahashi & Chiba 2001) or agrees with the observed image separation distribution (Oguri 2006). Traditionally, gravitationally lensed quasar candidates were searched for among apparently bright objects in quasar samples and are therefore biased towards small separation systems. The small panels in Figure 6.2 show four examples of lenses with different image separations. The pictures are scaled to reflect the relative sizes compared to each other. The first panel shows the quadruple quasar HE 0435-1223 with an image separation of 2.6″ (Wisotzki et al. 2002). The second panel is the 6″ double Q 0957+561, the first lensed quasar to be discovered (Walsh, Carswell & Weymann 1979). The giant lens SDSS J1004+4112 (which will be discussed in the following Chapter) is the largest quintuple lens found so far. The record holder in terms of image separation is the 22″ split lens SDSS J1029+2623, for which the component near image A was recently confirmed to be a third lensed image (Oguri et al. 2008).
So far only 16 out of the 100 known lensed quasar systems have a time delay determination, reflecting the difficulties of the measurement. These difficulties include telescope time allocation, observational gaps in the light curves, low variability amplitude of the source and uncorrelated variability in the images due to microlensing. Table 6.1 lists all objects for which the time delay could be determined, ordered by its length. The measured values are of the order of days to months. The longest value of 417 ± 3 days (Kundic et al. 1995) for Q 0957+561 was the first successful time delay measurement after a long controversy between different monitoring groups that was resolved when a sharp flux variation occurred.

In the following Section the main principles of gravitational lens theory are introduced. In Chapter 7 the unique quintuple lensed quasar SDSS J1004+4112 is studied in detail. We analyze four years of optical monitoring that allow us to measure the time delays between the images and to study the microlensing induced and intrinsic variability of the quasar.

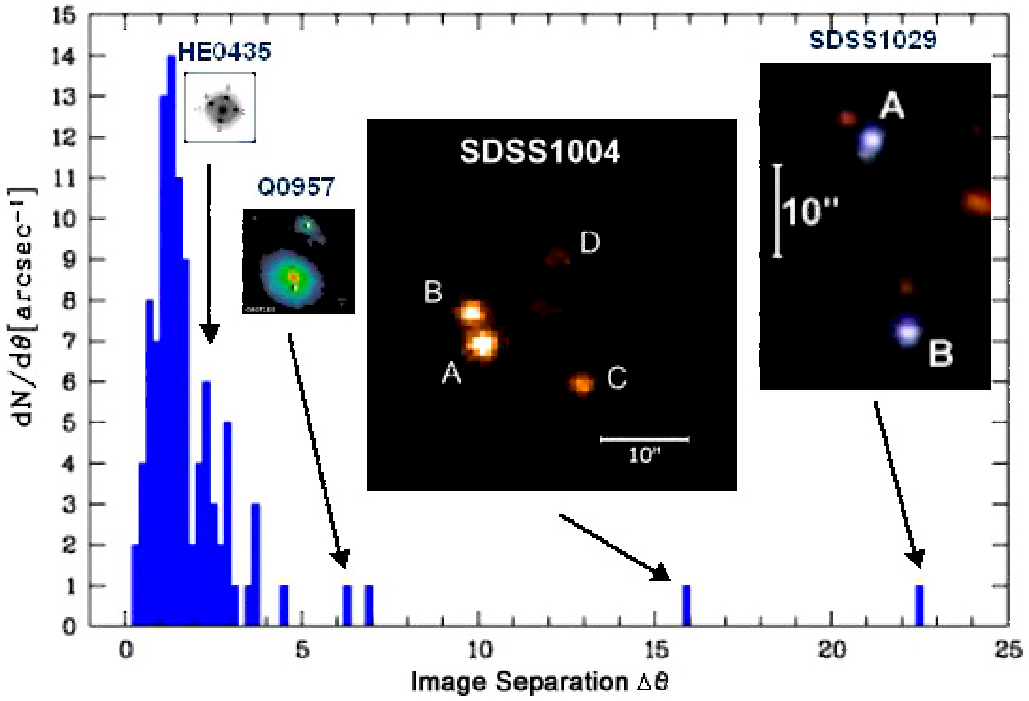

Figure 6.2: The distribution of gravitationally lensed quasars in image separation $\Delta\theta$ (based on the sample of 100 lensed quasars in the CASTLES list of 02/2008).

Table 6.1: Summary of Observed Quasar Time Delays

Lens Name	N_{image}	z_S	z_L	$\Delta\theta$ $[arcsec]$	$\Delta\tau$ $[days]$*
B1422+231	4	3.62	0.34	1.68	8.2±2.0
B0218+357	2	0.96	0.68	0.34	10.5±0.4
HE0435-1223	4	1.69	0.46	2.42	14.4±0.8
FBQ0951+2635	2	1.24	0.24	1.11	16±2
PG1115+080	4	1.72	0.31	2.32	25±2
PKS1830-211	2	2.51	0.89	0.99	26±4
SBS0909+523	2	1.38	0.83	1.17	45±5
SDSS1650+4251	2	1.54	0.00	1.23	49.5±1.9
B1600+434	2	1.59	0.41	1.40	51±2
B1608+656	4	1.39	0.63	2.27	77.0±1.5
RXJ1131-1231	4	0.66	0.30	3.80	87±8
HE2149-2745	2	2.03	0.50	1.70	103±12
SBS1520+530	2	1.86	0.72	1.59	129±3
RXJ0911+0551	4	2.80	0.77	2.47	146±4
HE1104-1805	2	2.32	0.73	3.19	152±3
Q0957+561	2	1.41	0.36	6.26	417±3

*For quadruple systems the longest measured delay is given.

6.1 Gravitational Lens Theory

6.1.1 The Lens Equation

Figure 6.3 shows the geometry of a simple lensing situation involving a source, a point lens and an observer. In this scenario the source at redshift z_S (or angular diameter distance D_S) from the observer, with a position angle $\vec{\beta}$ (corresponding to a distance η from the optical axis in the source plane) is lensed by a point lens at redshift z_L (distance D_L). The lens and source planes are perpendicular to the optical axis, which is defined as a straight line from the observer through the lens. D_{LS} denotes the distance between lens and source. The angle $\vec{\theta}$ and position ξ in the source plane at which the lensed image is observed result from the deflection angle $\hat{\alpha}$. From general relativity we know that the deflection angle for a circularly symmetric lens is

$$\hat{\alpha}(\xi) = \frac{4GM(\xi)}{c^2\xi}, \tag{6.1}$$

where the impact parameter ξ is the distance from the lens center to the image, and $M(\xi)$ is the mass enclosed within the radius ξ.
In the following all distances are interpreted as angular diameter distances, so that Euclidean geometry can be applied. Under the condition that all angles are small ($\hat{\alpha} \approx \sin\hat{\alpha} \approx \tan\hat{\alpha}$), which is fulfilled in most relevant astrophysical situations, from figure 6.3 one can read the relation:

$$\vec{\eta} = \frac{D_\mathrm{S}}{D_\mathrm{L}}\vec{\xi} - D_\mathrm{LS}\vec{\hat{\alpha}}(\xi), \tag{6.2}$$

where η denotes the two-dimensional position of the source from the optical axis in the source plane. By substituting $\vec{\eta} = D_S\vec{\beta}$ and $\vec{\xi} = D_L\vec{\theta}$ we derive the angular lens equation

$$D_\mathrm{S}\vec{\beta} = D_\mathrm{S}\vec{\theta} - D_\mathrm{LS}\vec{\hat{\alpha}}\ . \tag{6.3}$$

Introducing the reduced deflection angle $\vec{\alpha} = \frac{D_\mathrm{LS}}{D_\mathrm{S}}\vec{\hat{\alpha}}$, the equation translates into

$$\vec{\beta} = \vec{\theta} - \vec{\alpha}(\vec{\theta}), \tag{6.4}$$

and relates the true position of the source to its observed position on the sky. A source with true position β can have more than one solution for its observed angular position θ on the sky, i.e. the lens produces multiple images.

6.1.2 The Point Mass Lens

For a spherically symmetric lens, inserting the reduced deflection angle (eq. 6.1) and $\vec{\xi} = D_L\vec{\theta}$ into the Lens Equation (eq. 6.4) gives:

$$\beta(\theta) = \theta - \frac{D_\mathrm{LS}}{D_\mathrm{L}D_\mathrm{S}}\frac{4GM(\theta)}{c^2\theta}. \tag{6.5}$$

For a source that is perfectly aligned behind the lens on the optical axis ($\beta = 0$), the image is a ring whose angular radius is called the Einstein radius:

$$\theta_E = \sqrt{\frac{4GM(\theta_E)}{c^2}\frac{D_\mathrm{LS}}{D_\mathrm{L}D_\mathrm{S}}}. \tag{6.6}$$

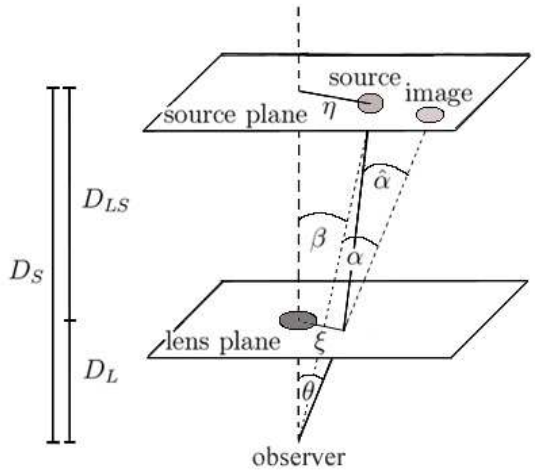

Figure 6.3: A schematic diagram of a gravitational lens system.

The Einstein radius provides a convenient angular scale in lensing situations. The typical Einstein radius for quasars lensed by galaxies is of order arcseconds. Using the Einstein radius (eq. 6.6), the lens equation for a point mass $M = M(\theta)$ has the form of a quadratic equation

$$\beta = \theta - \frac{\theta_E^2}{\theta} \,, \tag{6.7}$$

with two solutions for the image positions

$$\theta_\pm = \frac{1}{2}\left(\beta \pm \sqrt{\beta^2 + 4\theta_E^2}\right). \tag{6.8}$$

The images have different parity, one residing within and the other outside the Einstein ring.
Gravitational lensing changes the apparent solid angle of a source, not the surface brightness. The photons are redistributed, while their number is preserved.

$$\text{magnification} = \frac{\text{image solid angle}}{\text{source solid angle}} = \frac{\text{image area}}{\text{source area}}$$

The magnification factor μ is given by

$$\mu = \frac{\theta}{\beta}\frac{d\theta}{d\beta}. \tag{6.9}$$

By substituting the lens equation (eq. 6.7) for β we obtain the magnifications of the two images

$$\mu_\pm = \left[1 - \left(\frac{\theta_E}{\theta_\pm}\right)^4\right]^{-1} = \frac{u^2+2}{2u\sqrt{u^2+4}} \pm \frac{1}{2}, \tag{6.10}$$

where the impact parameter $u = \beta\theta_E^{-1}$ is the angular separation of lens and source in units of the Einstein radius.

The magnification of the image inside the Einstein ring is negative ($\theta_- < \theta_E$, $\mu_- < 0$). It has negative parity, meaning that the image is mirror-inverted compared to the source. The total magnification is the sum of the absolute magnifications of the two images:

$$\mu = |\mu_+| + |\mu_-| = \frac{u^2+2}{u\sqrt{u^2+4}}. \tag{6.11}$$

The difference between the magnifications of the two images is

$$|\mu_+| - |\mu_-| = 1. \tag{6.12}$$

If the source position is at the Einstein radius, $u = 1$, the total magnification becomes $\mu = \frac{3}{\sqrt{5}} \approx 1.34$, e.g. a magnification of 34% is observable. As $u \to 0$ the magnification diverges $\mu \to \infty$, and the solution is the Einstein ring with formally infinite magnification.

6.1.3 Magnification and Distortion

The distortion of images can be described by the Jacobian matrix A:

$$A = \frac{\partial\vec{\beta}}{\partial\vec{\theta}} = \left(\delta_{ij} - \frac{\partial^2\psi(\vec{\theta})}{\partial\theta_i\partial\theta_j}\right) = \begin{pmatrix} 1-\kappa-\gamma_1 & -\gamma_2 \\ -\gamma_2 & 1-\kappa+\gamma_1 \end{pmatrix}, \tag{6.13}$$

where the two-dimensional deflection potential $\psi(\vec{\theta})$ is related to the deflection angle $\vec{\alpha}$ by its gradient $\vec{\alpha} = \nabla\psi$, so that the mapping $\vec{\theta} \to \vec{\beta}$ is a gradient mapping. The convergence κ is related to ψ via the Poisson equation $\nabla^2\psi = 2\kappa$. We have introduced the components of the shear $\gamma \equiv \gamma_1 + i\gamma_2$,

$$\gamma_1 = \frac{1}{2}(\psi_{11} - \psi_{22}), \quad \gamma_2 = \psi_{12} = \psi_{21}. \tag{6.14}$$

The magnification is the inverse of the determinant of the Jacobian A:

$$\mu = \frac{1}{detA} = \frac{1}{(1-\kappa)^2 - |\gamma|^2}, \tag{6.15}$$

and becomes a function of the local convergence κ and the shear γ. The images are distorted in shape due to the tidal gravitational field described by the shear γ, while the convergence κ has the effect of expanding the light bundle. The magnification in a lens is not an observable, since the intrinsic luminosity of sources is unknown. Nevertheless, the magnification ratio is provided by the measurable flux ratio of the images.

6.1.4 Critical Curves and Caustics

Curves in the lens plane where the Jacobian vanishes, $detA = 0$, have formally infinite magnification and are called critical curves. Astronomical sources have a finite size, which keeps their observed magnification finite. The corresponding curves in the source plane which are obtained by mapping the critical curves into the source plane with the lens equation are called caustics. Critical curves are closed and smooth. Caustics in the source plane are not necessarily smooth, but can develop cusps. Caustics play a central role in the study of strong gravitational lensing. When a source approaches a caustic, images are highly magnified. If the source crosses a caustic, the number of images changes by two (e.g., Schneider et al. 1992). Spherically symmetric mass distributions have circular

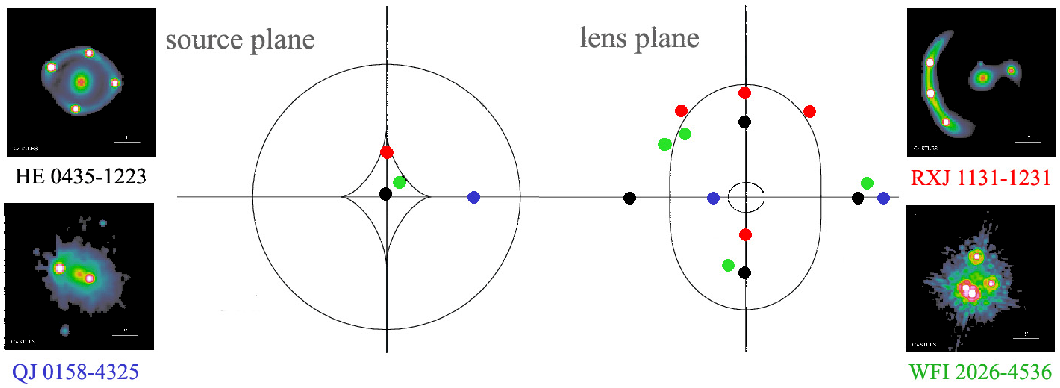

Figure 6.4: Critical curves (right) and caustics (left) of a non-circular lens. The four most common image configurations observed amongst lensed quasars are illustrated. The small panels show typical examples for these standard geometries from the CASTLES survey (Kochanek et al. 1999).

critical curves. In the case of a point mass lens, the caustic degenerates into a point. Elliptical lenses or spherically symmetric lenses plus external shear have caustics that show cusps and folds.

6.1.5 Image Configurations of Multiply Lensed Quasars

Lensing by galaxies is not well described by spherically symmetric lens models as in the simple point mass lens introduced above. In reality two sources of angular perturbations exist. The first one is the ellipticity of the lens. The second one is tidal perturbations from nearby objects, called external shear. Figure 6.4 shows typical image configurations produced by non-circular symmetric lenses. On the right half of the figure the two critical lines in the lens plane on which the Jacobian vanishes are displayed. The left half of the figure shows the corresponding inner (astroid) and outer caustics. The small panels give examples of the most commonly observed image configurations. The upper left cruciform geometry is created by a source near the center of the lens (black dots). A four-image lens showing three close bright images is observed when the source is close to a cusp caustic (upper right panel, red dots). When the source is located between the inner and outer caustic, two images on either side of the source are created (lower left panel, blue dots). The lower right panel shows an example for the image configuration that is also observed in the wide-separation lens SDSS J1004+4112, which is discussed in Chapter 7. This four-image geometry with one bright merging image pair is observed when the source approaches a fold caustic (lower right panel, green dots).

6.1.6 Fermat Potential and Time Delay

By using the lens equation (eq. 6.4) and writing the deflection angle as the gradient of the effective lens potential ψ we obtain:

$$(\vec{\theta} - \vec{\beta}) - \nabla\psi(\vec{\theta}) = 0 \tag{6.16}$$

We can introduce the Fermat potential as a function of the lens plane coordinate $\vec{\theta}$ and the source position $\vec{\beta}$:

$$\tau(\vec{\theta}; \vec{\beta}) = \frac{1}{2}(\vec{\theta} - \vec{\beta})^2 - \psi(\vec{\theta}) \tag{6.17}$$

so that its gradient

$$\nabla\tau(\vec{\theta};\vec{\beta}) = \nabla_\theta \left[\frac{1}{2}(\vec{\theta}-\vec{\beta})^2 - \psi(\vec{\theta})\right] = 0 \tag{6.18}$$

is equivalent to the lens equation (eq. 6.4). This means that lensed images appear at locations that correspond to extrema in the light travel time, corresponding to Fermat's principle in geometrical optics. Thus images are located at minima (maxima) and saddle points of the arrival time surface, which are characterized by the second derivative of the Fermat potential, i.e. the Jacobian matrix (eq. 6.13). Since the magnification factor is $\mu = (detA)^{-1}$, images at minima ($detA > 0$; $trA > 0$) and maxima ($detA > 0$; $trA < 0$) of τ have positive parities, while images at saddle points of τ ($detA < 0$) have negative parity.
The time delay function can be written from the lens equation in terms of the gravitational potential as

$$\tau(\vec{\theta}) = \frac{1+z_L}{c}\frac{D_L D_S}{D_{LS}}\left(\frac{1}{2}(\vec{\theta}-\vec{\beta})^2 - \psi(\vec{\theta})\right) = \tau_{geom} + \tau_{grav}. \tag{6.19}$$

The first term, τ_{geom}, depends on the image geometry $(\vec{\theta},\vec{\beta})$ and is the geometrical time delay due to the different path lengths of the deflected light ray compared to a direct line to the observer. The second term, τ_{grav}, is called Shapiro delay (Shapiro 1964). It represents the time dilation due to gravity in the lens potential. The involved distances depend on the Hubble constant. Therefore its value can be determined by measuring the difference in the arrival times, the time delay, between the images of a lensed quasar and using a good model for the effective lens potential ψ.

Chapter 7

The Quintuple Lensed Quasar SDSS J1004+4112

7.1 Introduction

The wide-separation lensed quasar SDSS J1004+4112 was discovered in the Sloan Digital Sky Survey search for lenses (Inada et al. 2003; Oguri et al. 2004). The quasar at $z_s = 1.734$ is split into five images. With a maximum image separation of $14\farcs62$ it is one of the rare examples of a quasar gravitationally lensed by a cluster (Inada et al. 2003, Wambsganss et al. 2003). The cluster at $z_l = 0.68$ has been characterized with X-ray observations (Ota et al. 2006; Lamer et al. 2006) and there are additional multiply imaged arcs formed from still higher redshift background galaxies (Sharon et al. 2005). The faint fifth lensed image of the quasar is located near the center of the brightest cluster galaxy (Inada et al. 2005). Figure 7.1 shows an Hubble Space Telescope image of the system.

The fact that the source is a time-variable quasar offers unique opportunities for this cluster lens. The time delay between the quasar images can be measured as a constraint on the mass distribution. In theory, the time delays determine the mean surface density near the images for which the delay is measured (Kochanek 2002). Several theoretical studies of the time delays in SDSS J1004+4112 (Oguri et al. 2004; Williams & Saha 2004; Kawano & Oguri 2006) have explored their dependence on the mean mass profile of the cluster, finding a broad range of potential delays. As we shall see, all these models are incorrect in their details because they neglect cluster member galaxies whose deflection scales are larger than the positional constraints on the quasar images used in the models. Nonetheless, all these models indicate that the delay between the A and B images is relatively short (weeks) and that its value should indicate the magnitude of the much longer (years) delays between the C and D images.

Traditionally, time delay measurements in lensed quasars are sought-after for determining the Hubble constant independently of local distance estimators (Refsdal 1964, Oguri et al. 2008). One other interesting applications of this system is to use the time delays between the lensed images to study the structure of the cluster. If we assume the Hubble constant is known, then the delays break the primary model degeneracy of lensing studies, the "mass sheet degeneracy" (Falco et al. 1985), as do analyses employing sources at different redshifts (see Sharon et al. 2005). The delay ratios constrain the structure even if the Hubble constant is unknown. Time delay estimates are furthermore required

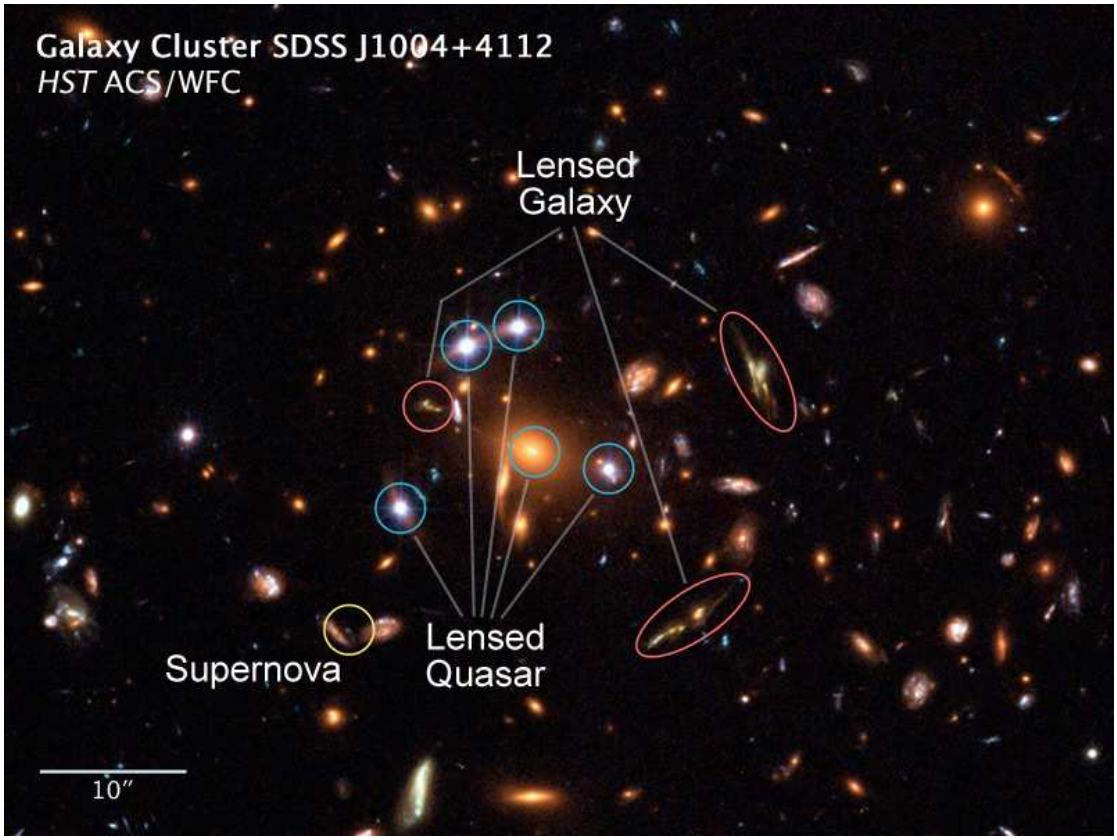

Figure 7.1: Hubble image of SDSS J1004+4112 showing the four bright quasar images and the galaxies of the lensing cluster. The positions of the images of lensed high redshift galaxies are also indicated (Credit: ESA, NASA, K. Sharon, Tel Aviv University and E. Ofek, Caltech).

to distinguish intrinsic source variability from variations due to microlensing by stars in the lensing galaxies. We expect this lens to have a fairly short time scale for microlensing variability caused by stars either in the intracluster medium or in galaxies near the images. The internal velocities of a cluster are much higher than in a galaxy (700 km/s versus 200 km/s), and SDSS J1004+4112's position on the sky is almost orthogonal to the CMB dipole (Kogut et al. 1993), giving the observer a projected motion on the lens plane of almost 300 km/s.
With a measured time delay microlensing variations can be extracted and used to estimate the mean stellar mass and stellar surface density of lensing galaxies, their transverse velocities, and the structure of the quasar source (Gil-Merino et al. 2005, Mortonson et al. 2005, Poindexter et al. 2007). Evidence for microlensing in SDSS J1004+4112 has already been reported based on differential emission line variability of the C IV broad line in image A compared to B by Richards et al. (2004), Lamer et al. (2006) and Gómez-Álvarez et al. (2006). Green (2006) suggested that this could also be due to time variable absorption in the source quasar.

In this Chapter we present the results of four years of optical monitoring for SDSS J1004+4112 in Section 7.2 and Section 7.3. The light curves span 1300 days and allow the measurement of the B-A, C-A and C-B delays as well as a lower estimate for the D-A delay. In Section 7.4 various methods for the determination of the delays and their advantages are

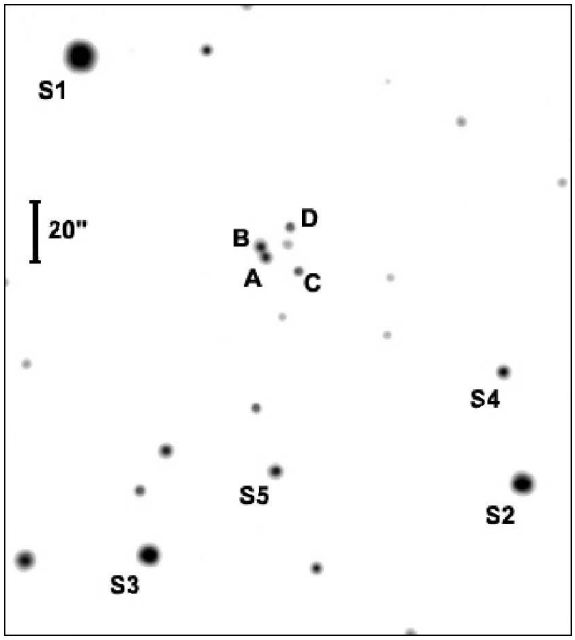

Figure 7.2: The r-band image obtained with Minicam on January 16, 2005. The 3.3 arcmin × 3.5 arcmin field shows the lensed images of SDSS J1004+4112 and the five reference stars S1, S2, S3, S4 and S5 used for the PSF.

discussed. In Section 7.6 the microlensing variability between the images in the system is estimated and in Section 7.8 we measure the structure function of the intrinsic variability. Conclusions and future prospects for exploiting this system are given in Section 7.9.

7.2 Data and Observations

The photometric monitoring observations presented here took place between December 2003 and June 2007. Table 7.1 gives a summary of all involved telescopes. The bulk of these data were taken with the 1.2m telescope at Fred Lawrence Whipple Observatory on Mount Hopkins (Arizona) using the 4Shooter (R-band, 93 epochs, 0.″66 pixels), Minicam (SDSS r-band, 74 epochs, 0.″604 pixels), and Keplercam detectors (SDSS r-band, 178 epochs, 0.″672 pixels, plus 4 epochs in R-band) during the first (December 03 - July 04), second (October 04 - June 05), third (October 05 - June 06) and fourth (October 06 - June 07) season respectively. Additional data were obtained with the Apache Point Observatory (APO) 3.5m telescope using SPICam (SDSS r-band, 9 epochs, 0.″282 pixels), the MDM 2.4m Hiltner telescope using the RETROCAM (Morgan et al. 2005, SDSS r-band, 47 epochs, 0.″259 pixels), 8K (R-band, 12 epochs, 0.″344 pixels), Templeton (R-band, 8 epochs, 0.″275 pixels) and Echelle (R-band, 3 epochs, 0.″275 pixels) detectors, the MDM 1.3m McGraw-Hill telescope using the Templeton detector (R-band, 6 epochs, 0.″508 pixels), the Palomar Observatory 1.5m telescope using the SITe detector (R-band, 13 epochs, 0.″379 pixels), the Wise Observatory 1.0m telescope with the Tektronix (R-band, 30 epochs, 0.″696 pixels) and TAVAS (clear, 53 epochs, 0.″991 pixels) detectors, and the WIYN 3.5m telescope using the WTTM (SDSS r-band, 3 epochs, 0.″216 pixels) detector. The combined data set consists of 533 epochs (one epoch being one observing night).
In Figure 7.2 the quasar images are labeled A, B, C and D, following the notation of Inada

Table 7.1: Summary of Monitoring Observations

Telescope	Detector	Pixel Scale [″/pixel]	N_{epoch}	Filter
FLWO 1.2m	4Shooter	0.666	93	R
	Minicam	0.604	74	r
	Keplercam	0.672	4+178	R+r
APO 3.5m	SPICam	0.282	9	r
MDM 2.4m	Retrocam	0.259	47	r
	8K	0.344	12	R
	Templeton	0.508	6	R
	Echelle	0.275	3	R
MDM 1.3m	Templeton	0.508	8	R
Palomar 1.5m	SITe	0.379	13	R
Wise 1.0m	Tektronix	0.696	30	R
	TAVAS	0.991	53	clear
WIYN 3.5m	WTTM	0.216	3	r

et al. (2003). The (non-variable) reference stars used for flux calibration and building the point spread function are S1, S2, S3, S4 and S5. The average sampling rate is once every third day. In each observing night at least three 300s exposures were taken. The images of each night were then combined to improve the signal-to-noise for the further analysis. Regions around each of the quasar images and the "standard" S1-S5 stars (see Figure 7.2) are fitted to determine the relative fluxes and the structure of the PSF. For each filter, the star S1 was defined to have unit flux while the fluxes of the stars S2, S3, S4 and S5 were adjusted to this calibration standard based on all the available epochs of data for each filter. The relative fluxes of the standard stars depend on the filter, with ratios of 1.0:0.439:0.360:0.130:0.0583 for the R-band, 1.0:0.334:0.329:0.0937:0.0613 for the SDSS r-band, and 1.0:0.63:0.64:0.39:0.20 for the clear filter. In the WIYN/WTTM, MDM 2.4m/8K and MDM 2.4m/Templeton data, the star S1 is frequently too close to saturation for use, so its weight in the fits is greatly reduced. It was not necessary to further subdivide the calibrations for the individual detectors given the overall quality of the photometry, as the average calibration offsets between detectors using the same filter were well under 0.01 mag. We then matched the R-band and clear observations to the r-band observations using the quasar light curves themselves. For each R/clear epoch bracketed by r-band observations within 1 week, we interpolated the r-band observation to the epoch of the other band and computed the mean offset between the light curves. Offsets of 0.043 ± 0.006 mag and 0.250 ± 0.011 mag must be added to the R-band and clear magnitudes respectively to match them to the r-band data. We note that our final magnitudes are not fully calibrated to the true r-band and that our analysis method derives more from the difference imaging methods used in almost all modern variability studies (Alard & Lupton 1998) than from classical photometry. In essence, we used the standard stars to put the data for each filter onto a consistent flux scale, and then used the quasars themselves to put the different filters onto a consistent flux scale. Color terms arising from the color differences between the stars and the quasars are unimportant because our analysis and results depend only on flux ratios between the quasars. The inclusion of the clear filter data might be problematic if the quasar images had very different colors. Empirically, eliminating the clear filter data has no effect on our results.

7.3 Light Curves and Variability

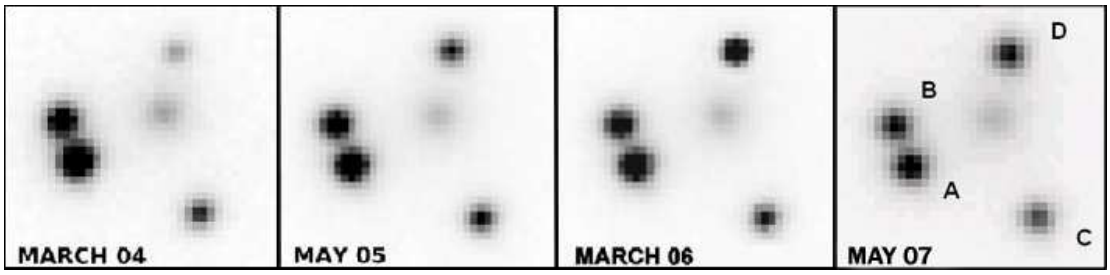

Figure 7.3: The panels show 23″ × 23″ insets on the four bright quasar images at the four observing epochs separated by about one year. The faint source in their middle is the bright galaxy belonging to the lensing cluster.

Figure 7.4 and 7.5 show the resulting light curves of the 4 bright quasar components and the small panels in Figure 7.3 show snapshots of the four bright quasar images at four different observing epochs, in March 2004, May 2005, March 2006 and May 2007. These images illustrate how images A and B slowly faded during the course of the four seasons while image D became significantly brighter. During the first season image D was very faint and almost not detectable in the background level of the frames. By the end of the fourth season its brightness was comparable to image B. The galaxies of the lensing cluster are not detectable in the individual observations, except for the bright galaxy close to image D (G1 in Oguri et al. 2004). The fifth quasar image, E, is also too faint to be detected in our frames. Its position is near the center of the bright galaxy G1.
The light curves in Figure 7.4 and 7.5 of the 4 bright quasar components span a range of 1300 days from December 2003 to June 2007. The time scales in this Figure is given as Julian date. $JD - 2452990 = 0$ corresponds to 16 December 2003. Table B.1 in the appendix presents the photometry for the four images. The gaps from July to October 2004, June to October 2005 and June to October 2006 are about 100 days each. During this time the object was not observable. In Fig 7.4 the raw data points for each observing night are shown without magnitude offset in order to present the quality of the data and the relative brightness of the images compared to each other. SDSS J1004+4112 is a relatively faint quasar for monitoring with 1m-class telescopes, and the image quality of the FLWO and WISE telescopes is poor. As a result, the noise in many of the measurements is relatively large compared to the variability amplitude. On the other hand, our sampling cadence is quite high, so the overall statistical power of the data is very good, with a mean sampling rate of once every third day while the source is visible. In Fig 7.5 the same data are binned by a running mean of one point every five days averaged over ±7 days and image C and D are offset by 0.3 and 1.0 mag, respectively, to emphasize the trends in the individual light curves of the images.

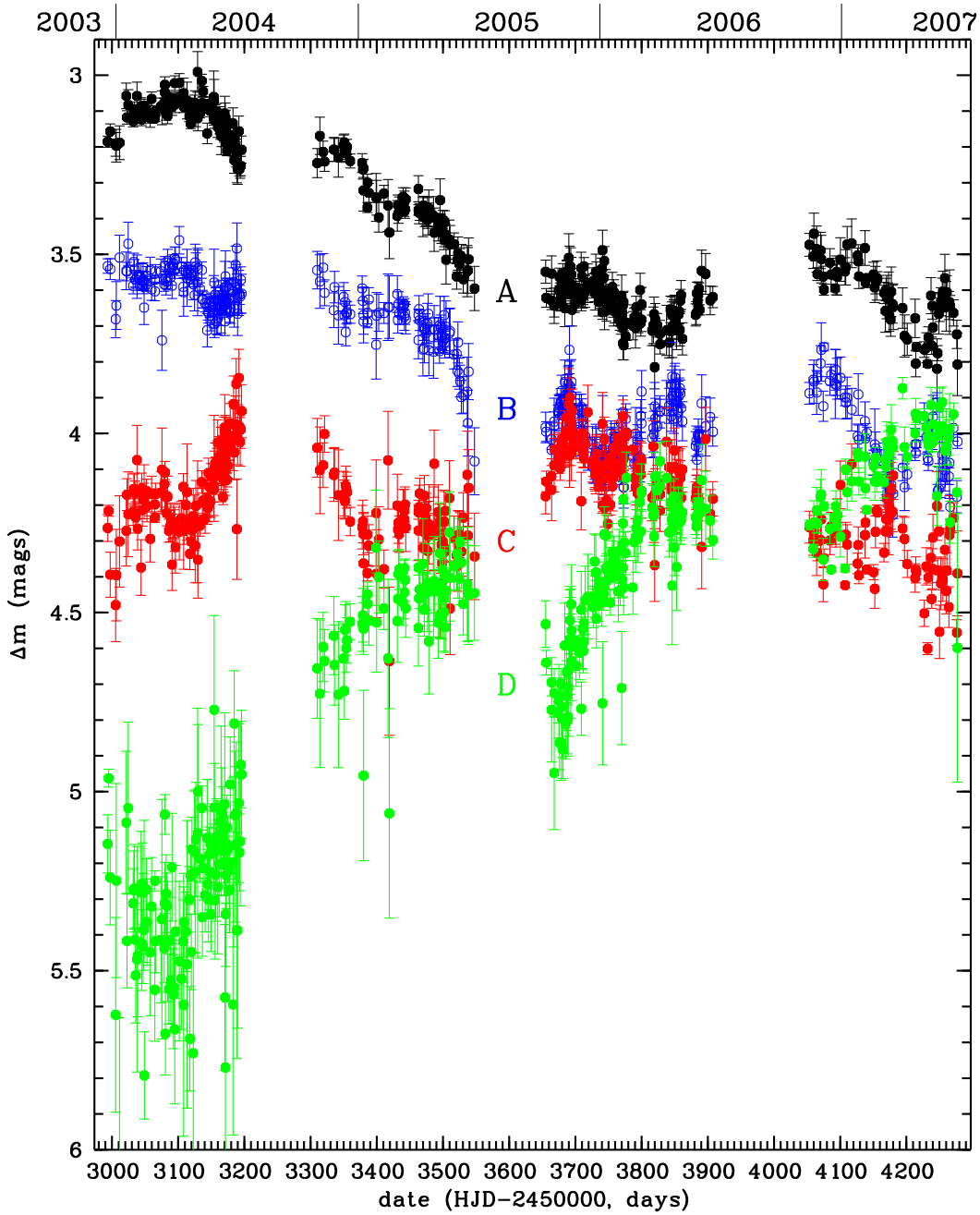

Figure 7.4: Light curves of the A, B, C and D images of SDSS J1004+4112 from December 2003 to June 2007.

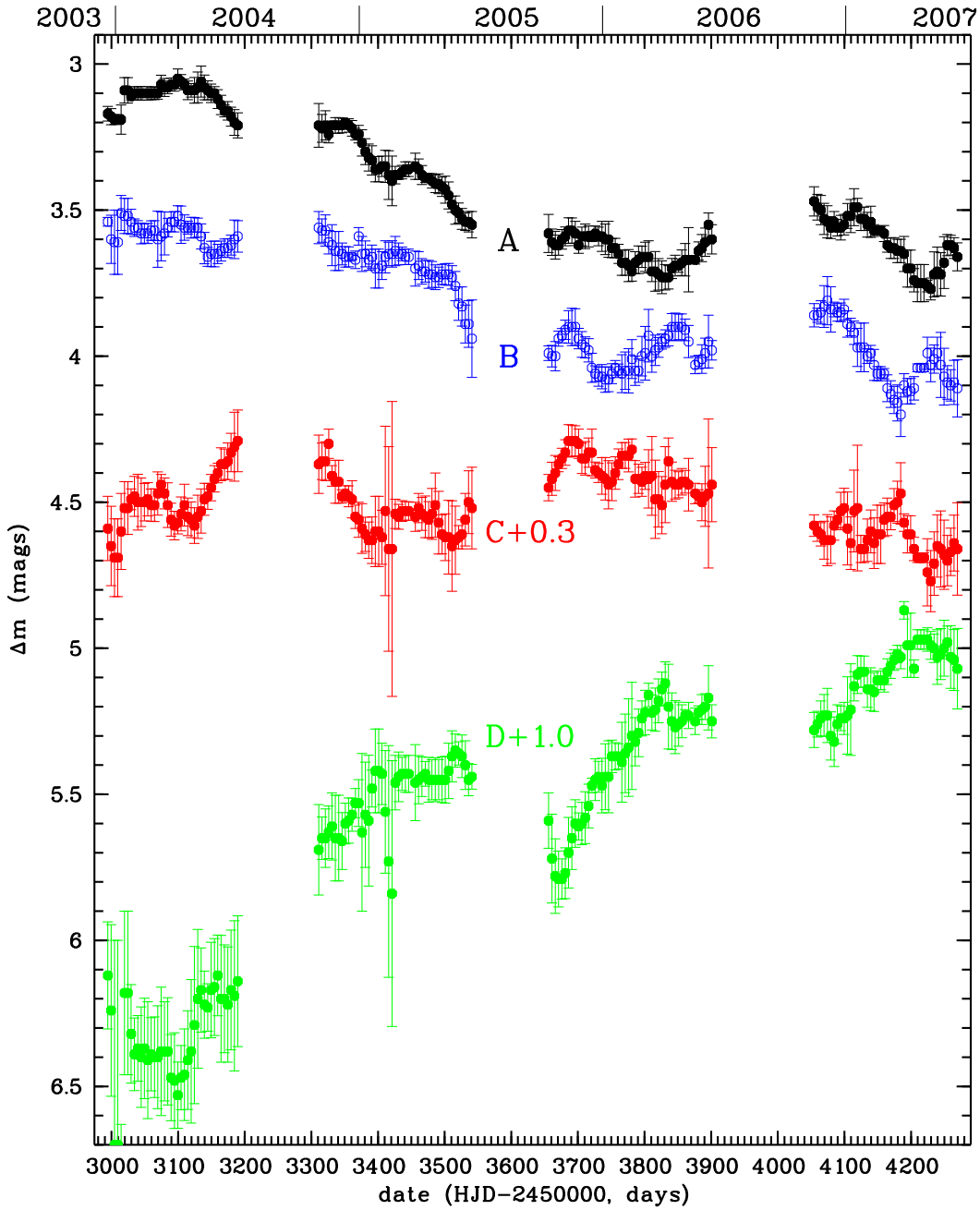

Figure 7.5: Same as Figure 7.4, with images C and D offset by 0.3 and 1.0 mag to avoid overlap with each other and with image B in the third season. Here we present a running average of the data (one point every five days averaged over ±7 days) to emphasize the trends rather than the noise.

All four bright quasar images show variability of more than 0.15 mag within each observing season. The close image pair A and B shows low amplitude brightness fluctuations of about 0.2 mag in the first season. Image A is rising slightly over the first 100 days and is declining slowly afterwards. The light curve of image B appears flat during the first 130 days of observations. After that image B shows a decline which appears to be very similar to that seen in image A at the end of the season, and then slightly rises again. In the second observing season the A and B light curves are almost monotonically decreasing. Both images get fainter by about 0.5 mag over more than 200 days. We note that towards the end of the second season image B shows a much steeper decline than image A. The data of the third season are more noisy. Brightness fluctuations of about 0.2 mag are observed. Image B shows a drop starting at 700 days and image A a similar one 740 days after the beginning of the monitoring. After 800 days image B is rising over 60 days by 0.2 mag. The same feature is seen in A at the end of the season. During the fourth season, images A and B faded by approximately 0.4 mag showing a nice feature with maxima in images A and B near days 4120 and 4080 respectively, followed by a roughly 100 day decline to minima at 4220 (A) and 4180 (B) days. For the purposes of measuring the B-A time delay, the most interesting features are the minima in the B light curve near days 3150, 3750 and 4190 in the first, third and fourth seasons respectively, and the corresponding features in the A light curve roughly 40 days later. The second season shows no obvious features that can be used to measure the delay.
The second important point to note is that the B-A flux ratio has changed significantly between the first and fourth seasons, indicating that microlensing is occurring in this system, as has been previously suggested by variations in the C IV emission line profile (Richards et al. 2004, Lamer et al. 2006, Gómez-Álvarez et al. 2006). The average R band (not time delay corrected) flux ratio between the close image pair is B/A=0.64±0.13 in the first season. The r band flux ratio in the second to fourth season are B/A=0.77±0.07, 0.73±0.07 and 0.69±0.08, respectively.

Compared to the close image pair, components C and D show variations of up to 0.6 mag within each of the observing seasons, with the strongest variations seen in image D. During the first 100 days of observations, image C was relatively constant and showed a rise of 0.4 mag by the end of the first season. At the beginning of the second season it had faded by about 0.5 mag during 100 days and stayed constant afterwards. Towards the third season it became 0.3 mag brighter with two small maxima at days 3680 and 3780. In the middle of the fourth season the light curve of image C shows a bump over 150 days of 0.4 mag.
In the first season image D could barely be detected due to its faintness, which is reflected in the large scatter of the data points. The same image became about one magnitude brighter in the second season (see Figure 7.3). The light curve of image D is monotonically increasing from day 100 to 400 and shows a plateau afterwards. By the end of season two, the two images C and D have equal brightness. Before October 2005 image D faded by 0.35 mag and was constantly rising within the third season by 0.7 mag before dropping down. During the fourth season image D continued brightening by 0.4 mag. Over the whole four seasons image D brightened by more than 1.5 mag and became the second brightest of the four images (see Figure 7.3).

7.4 Measuring the B–A Time Delay

Model predictions for the time delay of the close image pair A and B are a few weeks (Oguri et al. 2004; Williams & Saha 2004; Kawano & Oguri 2006) and therefore should be measurable within each season of the light curves. Many techniques for calculating time delays from light curves have been established (e.g. Gil-Merino et al. 2002, Pelt et al. 1994, Press, Rybicki & Hewitt 1992, Kochanek et al. 2006). In the following, three robust methods are applied. The three methods produce mutually consistent results, but we will adopt the Kochanek et al. (2006) polynomial method for our standard result because it naturally includes the effects of microlensing on the delay estimate. As is clear from the light curves, image B leads image A. The delay ordering of the images is thus C-B-A-D-E, because lens modeling either predicts this ordering or the reverse.
For our analysis of the B-A delay we treated the data that can be found in Table B.1 in the appendix as follows. If the point spread function fit for an image had a χ^2 statistic larger than the number of degrees of freedom N_{dof} (see Table B.1), we rescaled the photometric errors for that image by $\left(\chi^2/N_{dof}\right)^{1/2}$ on the grounds that having $\chi^2 > N_{dof}$ meant that the uncertainties were underestimated. For the time delay estimates we dropped the 16 points marked in Table B.1 that were more than 3σ from the best fitting models. We also repeated the time delay estimates excluding all points with rescaled photometric errors larger than 0.1 mag, finding no significant changes.

7.4.1 Simple χ^2 Minimization

The simplest approach to the delay measurement problem is to take the observed light curves $A(t_i)$ and $B(t_i)$ and cross-correlate them with linearly interpolated light curves $a(t)$ and $b(t)$ for the other image. Assuming the time series $A(t_i)$ and $B(t_i)$ are undisturbed replicas of the same underlying original quasar light curve shifted in time, the difference of both $A(t_i) - b(t_i - \tau)$ for the correct time delay τ should be a constant $m(\tau)$ and reflect the magnification ratio of the two images. In practice, we use a different magnitude offset for each season to partially compensate for the effects of microlensing. Based on this assumption the time delay is calculated by minimizing the deviations from $m(\tau)$ for each pair $(A(t_i), b(t_i - \tau))$ and $(a(t_i + \tau), B(t_i))$ by a fit statistic

$$\begin{aligned}\frac{\chi^2(\tau)}{N_{dof}(\tau)} &= \frac{1}{2N_{dof}(\tau)} \sum_i^{N(\tau)} \frac{(A(t_i) - b(t_i - \tau) + m(\tau))^2}{\sigma_{A,i}^2 + \sigma_{b,t}^2} \\ &\quad + \frac{1}{2N_{dof}(\tau)} \sum_i^{N(\tau)} \frac{(a(t_i + \tau) - B(t_i) + m(\tau))^2}{\sigma_{a,t}^2 + \sigma_{B,i}^2} \end{aligned} \tag{7.1}$$

that is symmetric as to which image is being interpolated. The errors in the observed magnitudes are $\sigma_{A,i}$ and $\sigma_{B,i}$ and the errors in the interpolated magnitudes are $\sigma_{a,t}$ and $\sigma_{b,t}$. The statistic is carried out only where the light curves overlap (i.e. excluding the seasonal gaps), so the number of data points used $N(\tau)$ depends on the delay τ.
Figure 7.6 shows the results for the four seasons separately and for the combined light curve. Analyzed separately, the first, third and fourth seasons show minima at 30.0 ± 5.0, 46.1 ± 5.0 and 36.9 ± 4.0 days respectively, while there is no clear minimum for the second season due to the lack of significant features in the light curve. For the joint analysis of all four seasons we allowed for an independent value of $m(\tau)$ within each season to model the

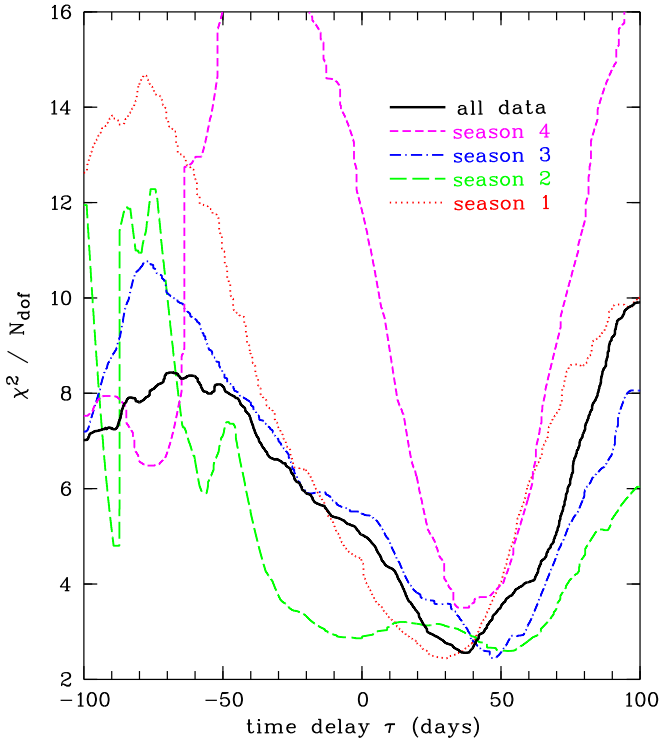

Figure 7.6: Results of the χ^2 minimization between the two time series A and B of SDSS J1004+4112 for the first (dotted line), second (dashed line), third (dash-dotted line), fourth (small dashed line) and combined observing seasons (solid line). Note that near the minimum for the combined light curve a change of χ^2/N_{dof} of 0.01 is statistically significant.

changes in the flux ratios due to microlensing. The analysis of the combined data yields a delay of 37.7±3.0 days ($\Delta\chi^2 = 4$).

7.4.2 The Dispersion Method

One potential weakness of the simple χ^2 method is the need for interpolation. As our second independent approach for the determination of the time delay between images A and B we apply the dispersion spectra method developed by Pelt et al. (1994, 1996). For this no interpolation between the data points to compare the light curve of the two images is needed. Instead, a combined light curve $C(t)$ is constructed by shifting the data points of one image in magnitude $m(\tau)$ and time (τ) and combining them with the data points of the other image

$$C(t_k) = \begin{cases} A_i, & \text{if} \quad t_k = t_i \\ B_j - m(\tau), & \text{if} \quad t_k = t_j + \tau \end{cases} \tag{7.2}$$

where $k = 1, .., N$ is the number of data points of the combined light curve $C(t_k)$ and $N = N_A + N_B$. The dispersion spectrum is defined as:

$$D^2(\tau) = \min_{m(t)} D^2(\tau, m(t)). \tag{7.3}$$

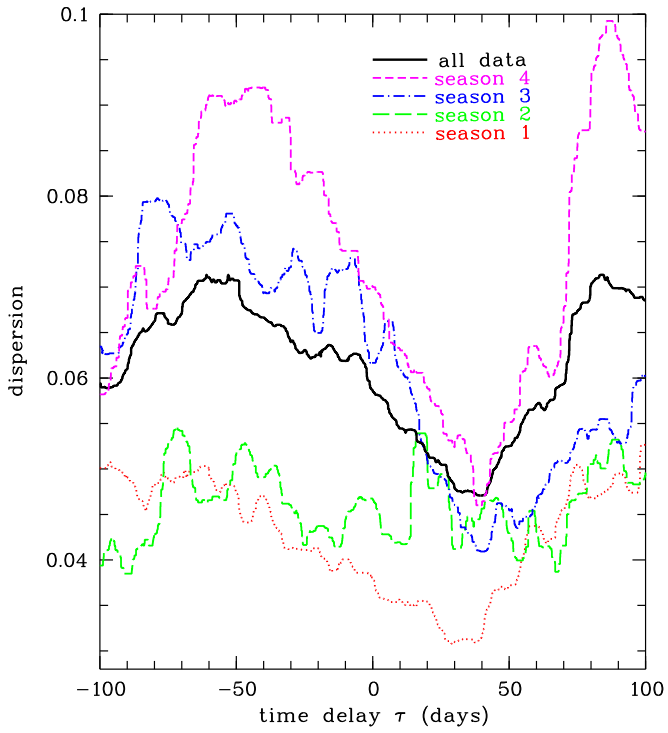

Figure 7.7: Dispersion spectra for the first (dotted line), second (dashed line), third (dash-dotted line), fourth (small dashed line) and combined observing seasons (solid line) for the delay between image A and B of SDSS J1004+4112.

Here we use the following analysis

$$D^2(\tau) = \min_{m(\tau)} \frac{\sum_{k=1}^{N-1} S_k W_k G_k (C_{k+1} - C_k)^2}{2 \sum_{k=1}^{N-1} S_k W_k G_k} \tag{7.4}$$

where the $W_k = (\sigma_k^2 + \sigma_{k+1}^2)^{-1}$ are the statistical weights of the data corresponding to the error bars. G_k is either 1 if the points k and $k+1$ come from different images (B-A) and 0 otherwise (A/A or B/B), to measure the dispersion in the overlap areas of the combined light curve. The parameter S includes only pairs in the combined light curve with less distance between two observations than a certain decorrelation length δ

$$S_k = \begin{cases} 1, & \text{if} \quad |t_{k+1} - t_k| \leq \delta \\ 0, & \text{if} \quad |t_{k+1} - t_k| > \delta \end{cases} \tag{7.5}$$

The value of the decorrelation length has only very small impact on the global behavior of the dispersion spectra because of the dense regular sampling of our observations. A decorrelation time scale of $\delta = 3$ days is used, but the results depend little on the exact choice.

The results are shown in Figure 7.7. As above, dispersion spectra were calculated for each observing season individually and for the combined data. We again used independent estimates of Δm for each observing season to compensate for the effects of microlensing.

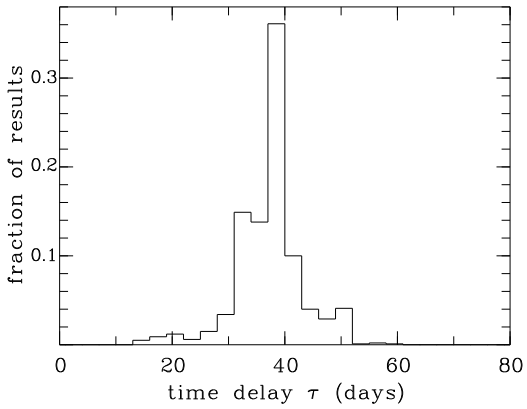

Figure 7.8: Results of the resampling procedure in the dispersion method. From the width of the distribution we estimate the uncertainty for the time delay measurement in the dispersion spectra.

We find 36.0 ± 7, 38.0 ± 4 and 38.7 ± 3 days for the first, third and fourth seasons, 40.1 days for the combined data, and no significant minimum using only the data from the second season.
We estimated the errors using the resampling procedure of Pelt et al. (1994). The combined light curve C_k was smoothed for each time delay using a 7-point median filter surrounding each point. Residuals relative to the original data were then reshuffled randomly to create artificially noisy combined light curves. Time delays for a set of 1000 such light curves were determined by calculating the dispersion spectra, leading to the distribution of minimum dispersion estimates shown in Figure 7.8. If we define the uncertainties by the range about the median encompassing 68% of the random trials, we estimate that the uncertainty in the time delay is ± 6 days.

7.4.3 The Polynomial Method

The clear indication of microlensing effects means that corrections for microlensing are required to determine an accurate time delay. Both the χ^2 and minimum dispersion methods treated the flux ratios between the images within each season as a constant. Either method could be modified to allow for more complex microlensing variations, but for our final analysis we will use the polynomial fitting method of Kochanek et al. (2006), since it can most easily incorporate the effects of microlensing on both the delays and their uncertainties.
In the polynomial method, each light curve is decomposed into intrinsic and extrinsic variations, in order to estimate the differential time delays between the images and to analyze the microlensing variability. Thus, the light curve of the ith lensed image, $m_i(t)$ is simultaneously fit with two Legendre polynomials one for the intrinsic $s(t)$ and one for the microlensing variation $\Delta\mu_i(t)$:

$$m_i(t) = s(t + \Delta t_i) + \Delta\mu_i(t), \tag{7.6}$$

with

$$s(t) \simeq \sum_{m=0}^{N_{src}} a_m P_m \left[\frac{t - t_c}{\delta t}\right], \tag{7.7}$$

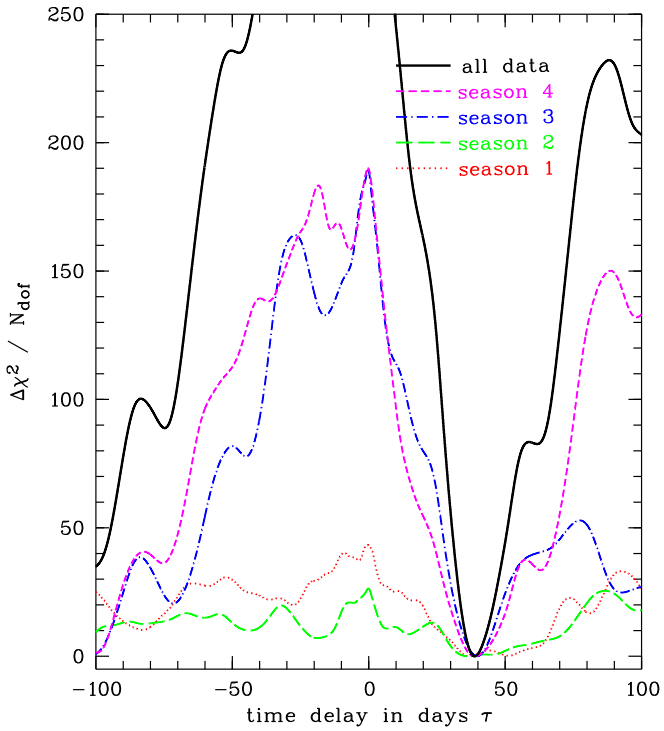

Figure 7.9: SDSS J1004+4112 polynomial method $\chi^2 - \chi^2_{min}$ for the standard model we adopt for the delay between image A and B. The dotted line shows the result for the first, the dashed line for the second, the dash-dotted line for the third, the small dashed line for the fourth and the solid line for the combined observing seasons. The dropping χ^2 at the edges is due to the diminishing overlap of the light curves, which allows the source variability to start fitting the two separate light curves independently and "perfectly."

and

$$\Delta\mu_i(t) = \sum_{m=0}^{N_\mu} c_{mi} P_m \left[\frac{t - t_c}{\delta t}\right], \tag{7.8}$$

where $s(t)$ is the magnitude of the source at time t, $t_c = (t_N + t_1)/2$ is the midpoint of the time series, $\delta t = (t_N - t_1)/2$ is the half-width of the time series, and P_m is the mth Legendre polynomial. If no microlensing occurs, the light curve of the ith lensed image, $m_i(t)$, would be a time and magnitude shifted copy of the source light curve.
When fitting the observations m_{ij} of the magnitude of image i at time t_j, the χ^2 fitting statistic is

$$\chi^2 = \sum_{i=1}^{N_{im}} \sum_{j=1}^{N_{obs}} \left(\frac{m_{ij} - s(t_j + \Delta t_i) - \Delta\mu_i(t_j)}{\sigma_{ij}}\right)^2. \tag{7.9}$$

By minimizing the χ^2, any choice of the time delays would provide an acceptable fit if series of arbitrarily high orders were allowed. Therefore a constraint from the observed variability of quasars is applied. For the ensemble quasar structure function using the photometry from SDSS quasars, Vanden Berk et al. (2004) measured

$$V(\tau) = (\tau/\tau_0)^\gamma \mathrm{mag}^2 \tag{7.10}$$

finding values of $\tau_0 \simeq 70{,}000$ days and $\gamma \simeq 1/3$ in the r-band. The mth term in the Legendre series has a mean square magnitude variation of $a_m^2/(2m-1)$ and a characteristic rest-frame time scale of $t_m = 4\delta t/m(1+z_s)$. The mean squared power of each term is allowed to be $(t_m/\tau_0)^{1+\gamma}$, i.e. the root-mean-squared variations should vary as $m^{-4/3}$ for $\gamma = 1/3$. Instead of minimizing the χ^2, the function

$$H = \chi^2 + \lambda \sum_{m=0}^{N_{src}} \frac{a_m^2}{2m-1} \left(\frac{\tau_0}{t_m}\right)^{1+\gamma}, \tag{7.11}$$

is minimized, where λ is a Lagrangian multiplier that controls the weight of the constraint on the quasar structure function relative to the weight of the individual data points.
The optimal values of Δt_i are determined by differentiating H with respect to the parameters and solving the resulting linear equations. The data from each season are considered separately.
The polynomial orders for the time variations of the source are modeled as a Legendre polynomial of order N_{src}, and the time variations due to microlensing are modeled as a Legendre polynomial of order N_μ in each of the three seasons. The orders are determined by using the F-test to indicate which polynomial order no longer leads to statistically significant improvements in the fits. We used polynomial orders of $N_{src} = 20$, 40, and 60 and $N_\mu = 0$, 1 and 2. The microlensing polynomial orders correspond to using a constant flux ratio, a linear trend or a quadratic trend for each season. Based on the F-test, the improvement in the fit to the data is significant when jumping from $N_{src} = 20$ to 40 and from $N_\mu = 0$ to 1 (from constant flux ratios in each season to linear trends), but not for any of the higher-order models. The delays for all the cases are consistent with each other given their uncertainties, so we will adopt the result for the $N_{src} = 60$, $N_\mu = 3$ model. Using higher than necessary polynomial orders should be conservative and overestimate the uncertainties in the time delay.

Figure 7.9 shows the results for the polynomial method for each of the four seasons separately and for the combined data set. The four seasons show minima at 37.0 ± 10.0, 36.5 ± 15.0, 39.8 ± 2.0 and 38.9 ± 3.0 days respectively. Formally a minimum is found for the second season, but its feature is not significant, resulting in a big error bar (± 15 days at $\Delta\chi^2 = 4$).
For the joint analysis of all four seasons the single seasons are fit with individual polynomials. The analysis of the combined data yields a delay of $\Delta t_{BA} = 40.6 \pm 1.8$ days ($\Delta\chi^2 = 4$, see Figure7.9). The overall fit has $\chi^2 = 1112$ for $N_{dof} = 677$ degrees of freedom. In this model, the mean magnitude differences between A and B for the three seasons are 0.460 ± 0.005, 0.283 ± 0.007, 0.339 ± 0.007 and 0.381 ± 0.007 mag.
Thus, microlensing is clearly present, as expected from the visible structure of the A and B light curves. The need to model the microlensing more accurately than just a seasonal change in the flux ratio means that the polynomial models fit the data considerably better than the first two methods, which is one reason for the significantly smaller formal uncertainties in the delay. Using only the higher precision data points has a negligible effect on the delays or the inferred level of microlensing. We can only measure the differential microlensing between A and B, and the choice of assigning it to image B is an arbitrary one which does not affect the time delay estimate.

7.5 The Long Time Delays

In the previous Sections the time delay between the A and B image pair of the quintuple lensed quasar SDSS J1004+4112 was measurable with a total of four observing seasons. While larger separation lenses tend to have longer time delays, for these two images the propagation time difference is small because they form a close image pair (separated by $3\farcs8$) created by the source lying close to a fold caustic. For the more widely separated C and D images theoretical models predict time delays of the order of months to years (Oguri et al. 2004; Williams & Saha 2004; Kawano & Oguri 2006). For example, Oguri et al. (2004) found an approximate scaling relation of $\Delta t_{\rm CD}/\Delta t_{\rm BA} = 143 \pm 16$ for their models, which would imply a 15 year C-D time delay given our result of 40.6 ± 1.8 days for the B-A time delay. On the other hand, Williams & Saha (2004) predicted delay estimates of order $\Delta t_{\rm CB} \approx 400$ days and $\Delta t_{\rm AD} \approx 600$ days, albeit with a large scatter (about ± 200 days).

7.5.1 The C-A and C-B Delay

After four years of monitoring the time range covered by the light curves provided sufficient overlap to measure the time delays for the wide separated ($14\farcs62$) image C relative to the close image pair. Empirically, we could test for delays between image C and A of ± 1300 days. Since the overall behavior of the A and B light curves during the first and second season is mainly decreasing or flat while the light curve of image C shows an increase in the first season (Figure 7.5), the time delay between C and B (with C leading) must be larger than 560 days. The very characteristic features in the light curves of the images A and B in the third and fourth season and of image C in the first and second season are suggestive for detecting a time delay "by eye". The bump at the beginning of the first season in C is very similar to that observed at the end of the third season in image B. There is a decline of about 0.3 mag at the beginning of the second season in image C that is repeated in image B in the fourth season, followed by a clear minimum.
For the statistical analysis of the time delay the methods described in Section 7.4 were applied. Using the dispersion spectra method (Pelt et al. 1994, 1996), we find $\Delta\tau_{CA} = 822 \pm 7$ days. To probe the result independently of the image A light curve, we check the time shift between the light curves of image C and B. The time ordering of the images being C-B-A-D, we expect a value of $\Delta\tau_{CB} = \Delta\tau_{CA} - \Delta\tau_{BA} = 782 \pm 7$ days. Our analysis yields a value of $\Delta\tau_{CB} = 780 \pm 6$ days, which is consistent with the prediction. The measurement for the time delay between images C and A is slightly less accurate than the time delay between C and B, because the shifted A light curve has less overlap with the image C light curve due to the seasonal gaps.
In Figure 7.10 the results for the χ^2-minimization for the C-B and C-A image pairs are shown. Both minima are separated by about 40 days, reflecting the time delay of the close image pair B-A. For the polynomial method analysis we simultaneously fit A, B and C holding the B-A delay fixed to 40.6 days and find a C-A delay of 821.6 ± 2.1 days. Figure 7.11 presents the polynomial method $\chi^2 - \chi^2_{min}$ for the $N_{src} = 60$, $N_\mu = 3$ model. The overall fit has $\chi^2 = 1850$ for $N_{dof} = 1035$ degrees of freedom.

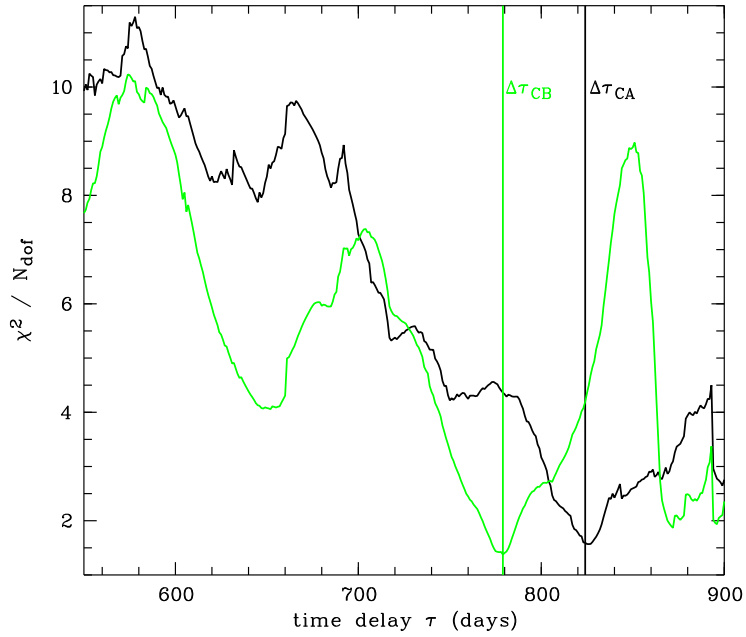

Figure 7.10: Result of the χ^2 minimization for the C-A and C-B delay in SDSS J1004+4112. The offset between the minima reflects the B-A delay. Both curves artificially drop for very large delays ($\geq$ 850 days), because of the diminishing overlap between the two light curves.

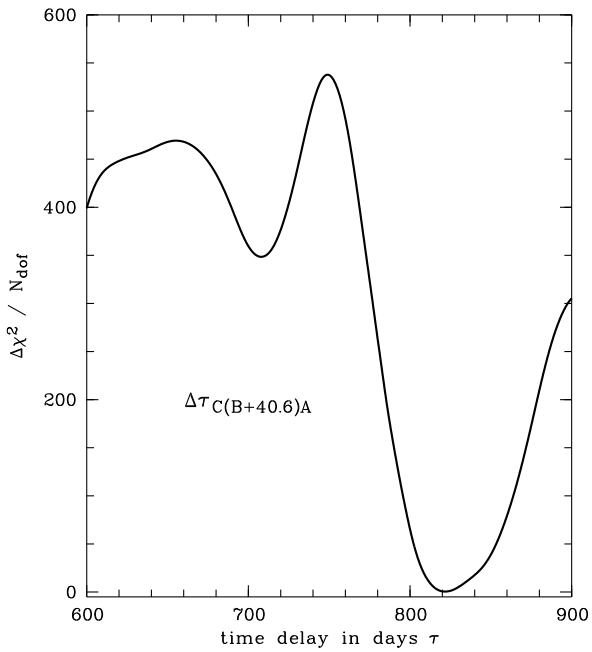

Figure 7.11: Polynomial method $\chi^2 - \chi^2_{min}$ for the C - BA delay in SDSS J1004+4112. A, B and C were simultaneously fit by holding the B-A delay fixed to 40.6 days. The minimum is at 821.6 ± 2.1 days.

7.5.2 Constraints on the A-D Delay

The observed light curve of image D is mainly rising during the overall course of our monitoring, while the light curve of image A is mainly fading. From the derived ordering of the images, we know that image D should lag the other three images. No feature is seen in the light curve of image D that can be matched to the first season of image A. By the end of the third season; the light curve of image D flattened, so that it seemed to be connectable to the first season in image A. In the fourth season image D continued to brighten, so it cannot be matched to the slowly fading A light curve of the first two seasons. From this behavior we can derive a lower limit on the time delay between the images A and D of $\Delta\tau_{DA} > 1250$ days (3.4 years).

7.6 Microlensing

Figure 7.12 shows the superposition of the shifted A, B and C light curves and the differences between them. From the residuals we can estimate the differential microlensing variability compared to image B. Image B was arbitrarily assumed to represent the intrinsic variability of the source quasar, because its light curve has most overlap with the other two. If we had chosen a linear interpolation of the data points of image B, the residual B light curve in the lower panel of Figure 7.12 would be zero. We decided to do a polynomial fit to the B light curve and then to subtract it from the three images to avoid adding additional noise to image C and A. If the light curves are not affected by microlensing and intrinsic variations of the source quasar are the only source of variability, the residuals of the time delay shifted light curves should be constant.
Figure 7.12 clearly shows that the residuals of the A and C light curves indicate that microlensing with amplitudes of order 0.15 mag is present. After correcting for the time delay, the mean magnitude differences between the images A and B for the four seasons are 0.460 ± 0.005, 0.283 ± 0.007, 0.339 ± 0.005 and 0.381 ± 0.007 mag. For the two seasons overlapping with image C we find mean magnitude differences, seasonal gradients and second derivatives of 0.590 ± 0.010 mag, -0.04 ± 0.02 mag/year and 0.29 ± 0.09 mag/year^2 for C relative to A and 0.368 ± 0.005 mag, 0.05 ± 0.01 mag/year and 0.18 ± 0.04 mag/year^2 for B relative to A.

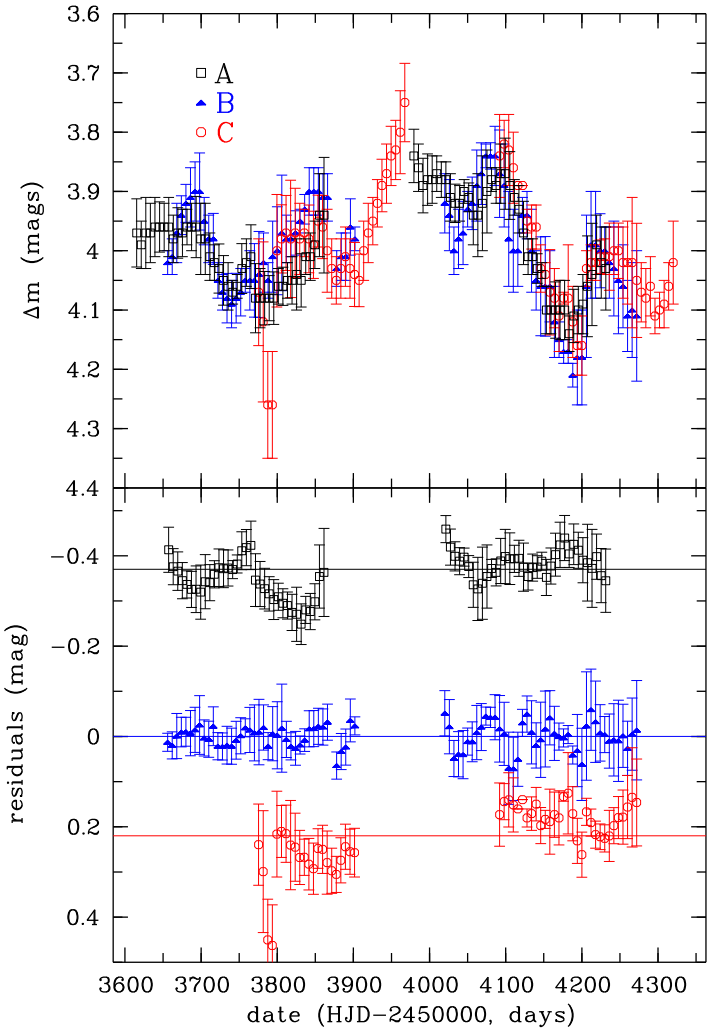

Figure 7.12: The image A, B and C light curves of SDSS J1004+4112 in their overlap region after shifting by the respective time delays. The data are binned in one week intervals with error bars derived by error propagation from the measurement errors (see Table B.1). The lower box shows the residual magnitudes shifted by the offset between the images, revealing microlensing variability of order 0.15 mag. The light curve of image B was chosen to have constant flux because it has the most overlap with the other two images.

7.7 Variability Forecast

With a value of 821.6 ± 2.1 days (2.3 years), the C-A delay is the longest gravitational lens time delay measured so far, almost doubling the previous longest value of Q 0956+561 (for comparison see Table 6.1). We note that SDSS J1004+4112 is an ideal laboratory for studying correlations in the intrinsic variability of quasars. With image C leading images A and B by 2.3 years (see Figure7.13), sharp variations in image C can be used to plan intensive monitoring of images A and B. The delay between A and B provides redundancies that protect against gaps caused by bad weather, the Moon or the Sun. As we have seen in Section 7.6, the difference light curve of the time delay shifted images gives an estimate of the amount of microlensing. The amplitude of microlensing magnification is known to be larger for compact sources, so that magnified images of quasars appear bluer. The same correlation has been found in variability studies of single quasars. When quasars become brighter they also become bluer. In SDSS J1004+4112 the two sources of variability can be distinguished, allowing to study the timescales and underlying physics of those effects. SDSS J1004+4112 could also be used to measure the response times of emission lines to continuum variability as a function of wavelength (Peterson et al. 2004, Kaspi et al. 2007). The long delays between the images also mean that seasonal gaps are completely filled. This allows us to examine the structure function of the variability with a densely-sampled, gap-free light curve (modulo corrections for microlensing).

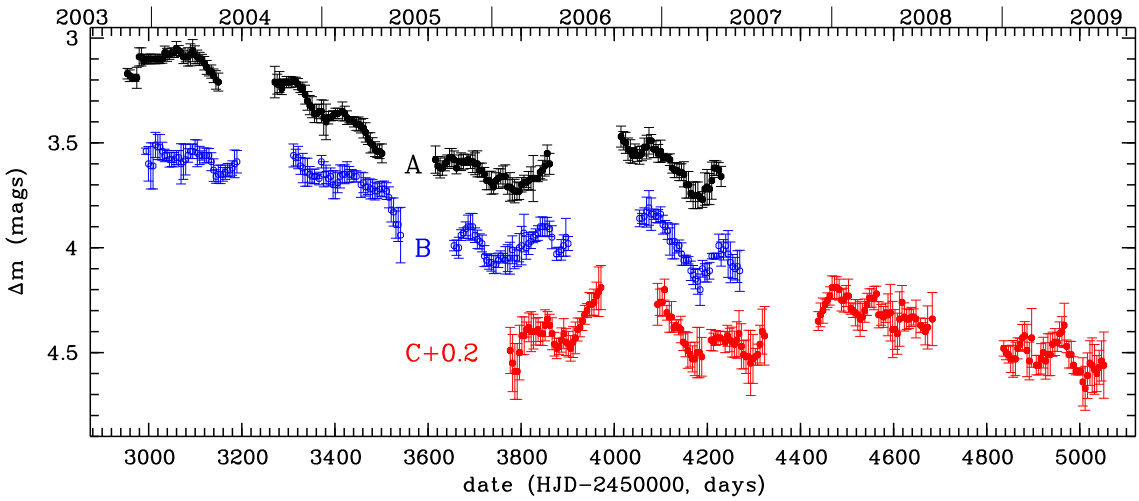

Figure 7.13: The time delay shifted image A, B and C light curves of SDSS J1004+4112. The data are binned (one point every five days averaged over ±7 days) to get rid of high-frequency noise and to emphasize trends. With image C being the leading image, its light curve provides a 2.3 yr forecast on the expected variability in the light curves of images A and B. That preview allows for well prepared detailed re-monitoring of prominent features like the bump in the third season and the sharp peak in the fourth season in the C light curve, which can be reobserved in image A and B in the ongoing season and in June/May 2009, respectively.

7.8 The Structure Function

The time scales of quasar variability can put constraints on the size and physical processes in the emitting region. The minimum time scales on which quasars can be seen to vary in brightness are usually poorly constrained due to observational noise. The measurement of the longest time scales of variability is limited by the length of monitoring baselines and lacks a sufficient number of well monitored objects. Over the last 20 years several groups have established correlations between a measure of the amplitude of variability and parameters such as luminosity and redshift. Analysis of big quasar samples (e.g. Vanden Berk et al. 2004) found an anti-correlation between luminosity and variability amplitude, i.e. more luminous quasars vary with smaller amplitude. However these studies suffer from a degeneracy between redshift and luminosity, which are correlated in most quasar samples.
One way to probe the time scales and amplitudes of quasar variability is the construction of the structure function. The quasar structure function is a tool to characterize quasar variability independent of short-timescale monitoring gaps and to compare with theoretical models of quasar variability (e.g. Kawaguchi et al. 1998). It measures the variability in the magnitude as a function of time lag between observational epochs. The structure function is defined as

$$S(\tau) = \sqrt{\frac{1}{N(\tau)} \sum_{i<j} [(m(t_j) - m(t_i))^2 - \sigma_j^2 - \sigma_i^2]}, \tag{7.12}$$

where $(m(t_j) - m(t_i))$ is the magnitude difference between two observations that are offset by a time lag τ and $m(t_j)$ is the measured magnitude with uncertainty σ_j at epoch t_j. The sum runs over $N(\tau)$ epochs for which $\tau = t_j - t_i$, and only includes those time differences where data is available. The structure function can be fitted as a single power law

$$S(\tau) = S_{100} \left(\frac{\tau}{100\text{days}} \right)^{\beta} \tag{7.13}$$

where τ is the rest-frame time difference and S_{100} is the amplitude for a time lag of 100 days.

For SDSS J1004+4112 we can determine the structure function over a moderate time range and with a dense sampling rate and no seasonal gaps if we use the time-delay connected quasar light curves. Such data generally do not exist; structure functions for individual quasars have been determined with very sparse observational sampling of only a few epochs per year (e.g. Hawkins 2007, 28 years of monitoring with 4 epochs per year) or in the composite form for big quasar samples but also very sparse sampling of about two epochs per quasar (Vanden Berk et al. 2004, de Vries et al. 2005, Wilhite et al. 2008).
We compute the structure function for the time-delay connected B and C light curves. These cover a time-baseline of 2065 days (5.7 years) in the observer's frame, corresponding to a maximum rest-frame baseline at $z_s = 1.734$ of 755 days. For the BC light curves we also computed the structure function subtracting the microlensing variability estimate found in the time delay analysis (see Section 7.6). For the very different behavior of the image D light curve, which could not yet be time-delay connected to the other images, we compute the structure function independently for rest frame time lags up to 470 days.
In Figure 7.14 we show the three structure functions with logarithmic axes. The bins were chosen to have equal logarithmic rest-frame time lag intervals. The error bars were

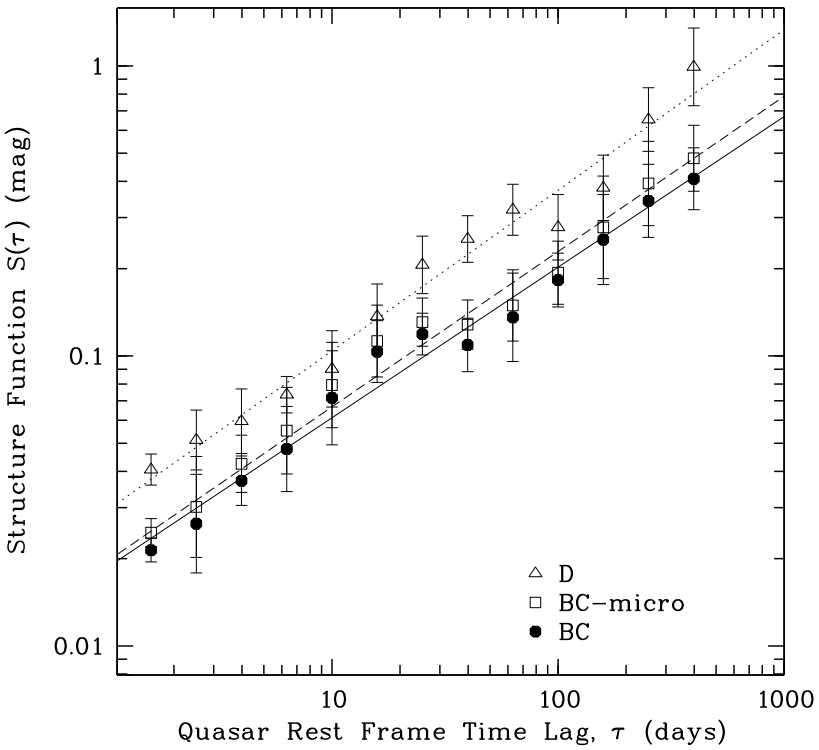

Figure 7.14: The quasar r-band structure function for the observed D light curve (triangles) and the time delay connected BC light curve (filled circles). The open squares present the structure function for the microlensing corrected BC light curve.

determined by propagating the measurement uncertainty in the magnitude differences and the statistical error in the mean for the values in that bin.
The slopes of the structure function are mutually consistent, with $\beta_{BC} = 0.52 \pm 0.02$ and $\beta_{BC'} = 0.54 \pm 0.02$ after subtracting the estimated microlensing variability. Microlensing has little effect on the results because the source variability (~ 0.7 mag) greatly exceeds the microlensing variability (~ 0.15 mag). After a rest frame time lag between two observations of 100 days (9 months in the observers frame), the mean magnitude difference for the BC light curve is $S(\tau = 100) = 0.19 \pm 0.05$ mag.
For image D we find a similar albeit steeper slope of $\beta_D = 0.55 \pm 0.03$, as expected from the light curve. The mean magnitude difference after 100 days, $S(\tau = 100)$, is 0.30 ± 0.06 mag and about 0.1 magnitude higher than that determined from the BC light curve. From the lower limit of our time delay estimate we know that the observed magnitude variations in image D precede by at least 3.4 years those of images A and B. If the brightening in image D of almost 1.5 mag during the four observing seasons together with the lower limit of the time delay indicate that the source was fainter in the past (which need not be the case, depending on the absolute magnification of image D), then the observed higher variability amplitude of the fainter image D could be related to the anticorrelation of variability with quasar luminosity found in large surveys of quasar variability (Vanden Berk et al. 2004, de Vries et al. 2005, Wilhite et al. 2008).
Theoretical models of quasar variability involving a starburst scenario predict slopes of $0.74 \leq \beta \leq 0.90$, whereas accretion disk instability models predict shallower slopes of

$0.41 \leq \beta \leq 0.49$ (Kawaguchi et al. 1998), as well as a flattening of the structure function after ~ 100 days in both cases. Our measurements are in disagreement with those predictions.
Quasar structure functions in the r-band have been determined over a similar time lag range for large ensembles of quasars and show shallower power law slopes. For example, Vanden Berk et al. (2004) found $\beta = 0.336 \pm 0.033$ for a sample of 25000 quasars, de Vries et al. (2005) found $\beta = 0.153 \pm 0.004$ for about 40000 quasars, and Wilhite et al. (2008) found $\beta = 0.486$ for a sample of 8000 quasars. We note that while our r-band measurement corresponds to the UV rest wavelength, the above r-band structure functions present the ensemble variability of many quasars (contributing only a very small number of epochs each), that have different redshifts and therefore also different rest wavelengths. Another systematic problem with the determination of the structure function from quasar ensembles is that small time lag bins are biased towards more luminous and high-redshifted objects. For the above samples, the average amplitudes at 100 days were $S_{100} \simeq 0.11$ (Vanden Berk et al. 2004), 0.23 (de Vries et al. 2005) and 0.121 mag (Wilhite et al. 2008). The structure function of SDSS J1004+4112 is steeper and shows a higher amplitude than the average quasar.
Other determinations for smaller samples that include observations of multiple epochs for each object show a diversity of power law slopes, e.g. 0.20 ± 0.01 (Hawkins 2007) or 0.47 ± 0.07 (Rengstorf et al. 2006). For the latter compilation the measured r-band 100-day-variability is 0.121 ± 0.001 and smaller than in the case presented here for a single quasar. Individual quasars are also known to show a diversity of slopes. For example, Collier & Peterson (2001) measured UV slopes ranging from 0.7 to 1.5 for a sample of 13 nearby active galactic nuclei and found their structure functions to flatten after time lags of about 10 days before exhibiting oscillations. In our data we don't see a sign of flattening towards higher time lags.

7.9 Conclusions

We have presented four seasons of monitoring data for the four bright images of the five image gravitational lens system SDSS J1004+4112. By using three different methods we measured the time delay between the merging A and B image pair, finding that B leads A by 40.6 ± 1.8 days. Together with model predictions for the arrival times, this fixes the overall time ordering of the images to be C-B-A-D-E. The three tested methods give consistent results within their error bars. The χ^2 minimization is very simple to apply, but interpolation between the data points where the behavior of the light curve is unknown is needed. The dispersion method avoids the need for interpolation by calculating the dispersion of the combined light curve. Nevertheless in this method we had to vary the magnitude offsets for each season between A and B to account for the microlensing. Without this modification, e.g. using a constant magnitude difference for all seasons, the dispersion method would fail to find the right time delay. The polynomial method has the advantage of simultaneously fitting the microlensing and intrinsic variability, but whether a polynomial is a good representation of a light curve is questionable; the order of the polynomial has no physical meaning. None of the methods succeed if there is no sufficient variability in the light curves (such as in the second season of the A and B light curves). To match two light curves at least one clear feature like a maximum or minimum that is repeated in the other image is needed. This feature needs to be well sampled. The observational period has to be long enough in order to have enough overlap and to avoid

shifting of one image into the observational gap of the other. If there is microlensing, the intrinsic variability needs to have higher amplitude to reveal the time delay. In our case the monitoring data fulfill these conditions so that all three methods work fine and give consistent results that are in agreement with checking the time delay by eye.

We also measured the very long delay for image C, finding that it leads image A by 821.6 ± 2.1 days (2.3 years). We note that this is nearly twice the longest previously measured delay (the 417 day delay in Q 0957+561, Schild & Thomson 1995, Kundic et al. 1997). We find a lower bound that D lags A by more than 1250 days (3.4 years). The fractional uncertainties in the B-A delay are still dominated by sampling and microlensing, while the fractional uncertainties in the C-A delay are dominated by cosmic variance due to density fluctuations along the line of sight rather than our measurement uncertainties of 0.3%.

A detailed mass model of the lensing galaxy cluster, including the constraints from the multiply imaged, higher redshift arcs (Sharon et al. 2005), the X-ray measurements (Ota et al. 2006, Lamer et al. 2006) and a detailed understanding of the uncertainties will be a challenge. At present, there is no completely satisfactory model for the system in the sense that the modeling of the lensing mass distribution is complex due to the gravitational potentials associated with the cluster member galaxies. All previous model studies (Oguri et al. 2004; Williams & Saha 2004; Kawano & Oguri 2006) generically predicted shorter B-A delays than the observed 40 days. This could be plausibly explained by the absence of substructure (i.e. galaxies) in the potential models. The longer C-AB and AB-D delays should be less sensitive to substructure. Oguri et al. (2004) do not include an estimate of the C-AB delays and have A-D delays consistent with our present limits. The range of B-C delays in Williams & Saha (2004) is consistent with our measurement of 780 days, but they predict A-D delays shorter than our current lower bound of 1250 days. Kawano & Oguri (2006) predict a long range for the longer delays over a broad range of mass distributions, none of which match our delays in detail. However, models with sufficiently long C-B delays generally have C-D delays long enough to agree with our present limits.

We have also clearly detected microlensing variability in the B-A images, with changes of order 0.15 mag in the B-A flux ratio over the course of the four observing seasons. This result provides strong evidence that the previously observed differential changes in the B-A emission line profiles are also due to microlensing (Richards et al. 2004, Lamer et al. 2006, Gómez-Álvarez et al. 2006) rather than variable absorption in the source (Green 2006). The microlensing time scales in SDSS J1004+4112 should be relatively shorter than in most single galaxy lenses because the internal velocities of the cluster are about 3 times higher than those of a galaxy. While the flux ratio changes in the optical continuum are modest, we would expect to find significantly larger effects at shorter wavelengths where the source size should be more compact. There is already some evidence for this from the X-ray flux ratios measured by Ota et al. (2006) and Lamer et al. (2006). A campaign to monitor this system in X-rays would both allow us to study the size of the X-ray emission region and provide the added data on the emission from the cluster needed to determine a precision comparison of the mass distributions estimated using X-ray data and lens models. Further observations, the inclusion of additional images, and monitoring in multiple bands will help to improve the measurements and potentially allow us to determine the mean surface density in stars near the images κ_* and their average mass $\langle M \rangle$. Similarly,

the ability to construct continuous light curves of the intrinsic variability and to use image C to provide early warning of sharp flux changes that can then be intensively monitored in images A and B may make this system a good candidate for applying reverberation mapping techniques to a massive, luminous quasar. At present, the structure function of this system indicates that the source is considerably more variable than the average quasar. This is promising for both improving the accuracy of the time delays and for using reverberation mapping techniques as an additional probe of the source structure.

The results described in this Chapter have been published in the Astrophysical Journal as Fohlmeister et al. 2007 and Fohlmeister et al. 2008.

Chapter 8

Summary and Perspectives

The effects of quasar light absorption and deflection provide remarkable insight into the composition and matter distribution of objects along the line of sight.
In the first part of this thesis we studied the absorption of quasar light by intervening H I Lyα and metal absorption systems.
The spectrum of the quasar PKS 0458−020 at redshift $z = 2.286$ shows a strong absorption by an intervening damped Lyα (DLA) system at redshift $z_{abs} = 2.03954$. This DLA with a column density of $\log N(\mathrm{H\ I}) = 21.7$ is one of the rare examples in which H I Lyα is also detected in emission in the center of the damped Lyα absorption trough. DLAs are believed to arise in intervening galaxies. We derive the amount of stellar mass produced in that galaxy per year, the star formation rate (SFR), from the Lyα emission to be SFR $= 1.6^{+0.6}_{-0.3}$ $M_\odot$ yr^{-1}. Beside the strong Lyα absorption several metal absorption lines that arise in the same DLA galaxy are detected in the spectrum of the background quasar. We measure the metallicities for Mg II, Si II, P II, Cr II, Mn II, Fe II and Zn II to be -1.21 ± 0.12, -1.28 ± 0.20, -1.54 ± 0.11, -1.66 ± 0.10, -2.05 ± 0.11, -1.87 ± 0.11, -1.22 ± 0.10, respectively, relative to solar. The depletion factor is therefore of the order of [Zn/Fe] = 0.65. We observe the metal absorption lines to be blueshifted compared to the Lyα emission up to a maximum of ∼100 and 200 km s^{-1} for low and high-ionization lines respectively. This can be interpreted either as the consequence of rotation in a large disk or as the imprint of a galactic wind. By comparing the star formation rate derived from the Lyα emission with that estimated from the observed C II* absorption we can give a lower limit on the size of the H I disk of $R \sim 7$ kpc. No molecular hydrogen is detected in the data, yielding a molecular fraction $\log f < -6.52$. This absence of H_2 can be explained as a consequence of a high ambient UV flux which is one order of magnitude larger than the radiation field in the inter stellar medium of our Galaxy and originates in the observed emitting region.

The two sight lines to the quasar pair Q 0037-3544 and Q 0037-3545 probe the spatial extent of absorbers over a distance of 760 kpc, corresponding to the angular separation of the two background quasars of $1.'7$. High resolution spectra of the two quasars revealed coinciding Lyα absorbers at the same redshifts in both lines of sight. We obtained deep images of the field around the quasar pair in the B, V, R, I and H and Ks bands that allowed us to measure photometric redshifts of all galaxies in the field. Field galaxies at redshifts corresponding to weak Lyα and metal absorptions towards the two quasar lines of sight Q 0037-3544 and Q 0037-3545 have been identified. The results indicate that the absorbing structures extend over a distance of 760 kpc. We measure the photometric

redshift of one field galaxy in the vicinity of the quasar Q 0037-3544 to be similar to the observed metal absorption at z = 0.59. This might imply a large (<70 kpc) gaseous halo around the galaxy, but spectroscopic redshift confirmation is needed. We find an overdensity of galaxies in front of the quasar Q 0037-3544. Spectroscopic redshift determinations will help to reveal the nature of this structure. So far, observational evidence, such as the non-detection of O VI absorption and extended X-ray emission, suggests the absence of hot gas that is typical for clusters. The field around Q 0037-3545 seems less populated by galaxies in the studied redshift range, which is in agreement with the absence of detectable metal absorption line systems along the line of sight.

In the second part of this thesis the effect of quasar light deflection was analyzed by studying the variability of the lensed quasar SDSS J1004+4112. This object is the only known example of a gravitationally lensed quasar where an intervening galaxy cluster acting as a lens causes the light to split into five images with a large separation of ∼14.6 arcseconds. We presented four years of optical monitoring from December 2003 to June 2007 for the four brightest images of the lensed quasar. These light curves allowed us to determine the differences in the light arrival times, the time delay, between the images. By using three different methods, we find the time delay between the close image pair A and B to be $\Delta t_{\rm BA} = 40.6 \pm 1.8$ days, with B being the leading image. We find that image C leads image A by $\Delta\tau_{CA} = 821.6 \pm 2.1$ days (2.3 years). The lower limit on the remaining delay is that image D lags image A by $\Delta\tau_{AD} > 1250$ days. Together with theoretical models, the time delays settle the time ordering of the images to be C-B-A-D-E. We detect microlensing variability of order 0.15 mag superimposed on the intrinsic quasar variations. Shifting the light curves of the images with respect to their time delay and magnitude offset allows us to fill in the seasonal gaps and assemble a continuous, densely sampled light curve spanning 5.7 years. The intrinsic variability of the quasar is characterized by a structure function with a logarithmic slope of $\gamma = 0.52 \pm 0.02$. From this we can derive that on time scales of 100 days, energetic processes in the quasar source cause brightness changes of $0.20 \leq \Delta m \leq 0.55$ mag. With C being the leading image, its light curve gives a forecast on the expected variations in image A and B. Sharp features in the C light curve can be intensively reobserved 2.3 years later in the A and B image pair, allowing more detailed and well planned variability studies. We note that the time delay between the images C and A is the longest measured time delay in a gravitationally lensed quasar so far.

Appendix A

Galaxies in the Field of the Quasar Pair Q 0037-3544 and Q 0037-3545

Table A.1: List of the galaxies presented in Chapter 5 in the field of the quasar pair Q 0037-3544 and Q 0037-3545 with I< 24.5 and $\Delta z/(1+z) < 0.3$. The columns give the positions, the apparent magnitude in six filters and the obtained photometric redshifts.

RA	DEC	B [mag]	V [mag]	R [mag]	I [mag]	H [mag]	Ks [mag]	z
00 39 47.37	-35 30 48.46	24.50±0.06	23.45±0.03	22.44±0.02	21.43±0.02	19.07±0.08	*	0.67±0.01
00 39 43.42	-35 30 48.66	23.43±0.05	23.26±0.03	22.92±0.02	22.46±0.03	20.10±0.10	*	0.79±0.01
00 39 33.79	-35 30 44.77	26.74±0.13	25.22±0.06	24.34±0.04	23.19±0.04	19.89±0.10	20.71±0.20	0.68±0.10
00 39 33.72	-35 30 46.49	24.83±0.06	24.24±0.04	23.67±0.03	22.80±0.03	21.12±0.15	*	0.80±0.02
00 39 47.61	-35 30 46.68	24.50±0.06	23.94±0.04	23.61±0.03	23.59±0.06	22.11±0.24	*	0.37±0.30
00 39 49.36	-35 30 44.06	25.22±0.07	24.90±0.05	24.82±0.06	24.25±0.07	*	*	0.94±0.06
00 39 48.35	-35 30 42.98	24.32±0.06	24.09±0.04	24.09±0.04	23.42±0.05	*	*	0.94±0.00
00 39 42.23	-35 30 43.23	23.64±0.05	23.27±0.03	22.87±0.02	22.05±0.03	20.17±0.11	*	0.85±0.04
00 39 34.74	-35 30 38.18	25.43±0.08	25.35±0.06	24.73±0.05	23.75±0.05	22.04±0.23	*	0.93±0.42
00 39 31.93	-35 30 37.75	25.20±0.07	24.81±0.05	24.45±0.04	23.88±0.05	*	*	0.72±0.08
00 39 50.10	-35 30 34.47	26.05±0.09	26.00±0.08	25.02±0.06	24.33±0.07	* *	*	0.73±0.38
00 39 34.57	-35 30 35.12	24.78±0.06	24.53±0.04	24.13±0.04	23.49±0.04	21.62±0.18	*	0.78±0.16
00 39 32.75	-35 30 33.26	23.01±0.05	22.41±0.02	21.83±0.01	21.38±0.02	19.99±0.10	*	0.57±0.01
00 39 42.13	-35 30 34.83	24.39±0.06	23.93±0.04	23.69±0.04	23.43±0.05	21.84±0.21	*	0.08±0.10
00 39 50.06	-35 30 26.23	20.15±0.05	19.52±0.02	19.19±0.01	18.73±0.02	17.42±0.07	*	0.44±0.04
00 39 43.20	-35 30 32.88	25.75±0.09	25.25±0.06	24.56±0.05	24.01±0.06	*	*	0.63±0.02
00 39 39.06	-35 30 32.52	24.13±0.06	23.52±0.03	22.85±0.02	22.25±0.03	21.79±0.20	*	0.64±0.04
00 39 49.75	-35 30 24.95	23.08±0.05	22.94±0.03	22.40±0.02	21.67±0.03	21.51±0.19	21.03±0.23	0.76±0.05
00 39 31.67	-35 30 21.64	24.89±0.07	24.85±0.05	24.41±0.05	23.97±0.06	22.18±0.24	*	0.67±0.26
00 39 32.46	-35 30 21.84	24.03±0.06	23.99±0.03	23.41±0.02	22.63±0.03	21.75±0.20	*	0.79±0.12
00 39 30.45	-35 30 20.20	24.74±0.06	24.40±0.04	23.87±0.04	23.09±0.04	*	*	0.81±0.15
00 39 46.73	-35 30 15.55	23.58±0.05	23.04±0.03	22.34±0.02	21.85±0.03	20.16±0.11	19.81±0.14	0.56±0.21
00 39 33.89	-35 30 14.02	24.77±0.06	24.54±0.04	24.22±0.04	23.50±0.05	*	*	0.85±0.02
00 39 39.13	-35 30 13.27	24.43±0.06	24.32±0.04	24.05±0.04	23.65±0.05	*	*	0.78±0.12
00 39 37.30	-35 30 14.24	24.59±0.06	24.01±0.03	23.18±0.02	22.60±0.03	20.69±0.13	20.31±0.17	0.51±0.06
00 39 30.14	-35 30 12.15	25.20±0.07	24.60±0.04	24.40±0.05	23.57±0.05	*	*	0.85±0.07
00 39 36.19	-35 30 08.62	25.39±0.08	25.16±0.05	24.38±0.04	23.49±0.05	20.47±0.12	*	0.70±0.05
00 39 34.55	-35 30 10.93	25.79±0.09	24.82±0.05	24.33±0.05	23.85±0.06	*	*	0.09±0.07
00 39 30.51	-35 30 09.19	24.99±0.07	24.90±0.05	24.54±0.05	24.20±0.07	*	*	0.67±0.05
00 39 37.77	-35 30 07.22	26.59±0.12	25.12±0.05	24.51±0.05	23.86±0.06	*	*	0.27±0.19
00 39 31.88	-35 30 08.87	24.14±0.06	23.83±0.03	23.38±0.03	22.65±0.03	21.05±0.15	20.32±0.18	0.81±0.00
00 39 44.23	-35 30 08.94	24.17±0.06	23.83±0.03	23.24±0.02	22.37±0.03	20.56±0.12	*	0.80±0.14
00 39 42.64	-35 30 07.39	25.95±0.10	25.56±0.08	24.73±0.06	24.28±0.08	*	*	0.60±0.10

Table A.1 – continued

RA	DEC	B [mag]	V [mag]	R [mag]	I [mag]	H [mag]	Ks [mag]	z
00 39 33.52	-35 30 01.81	25.60±0.08	25.41±0.06	25.26±0.07	24.45±0.08	*	*	0.90±0.37
00 39 48.13	-35 30 01.69	25.19±0.07	24.97±0.05	24.34±0.04	23.72±0.05	*	*	0.69±0.01
00 39 33.50	-35 29 57.35	24.18±0.06	23.96±0.03	23.50±0.03	23.28±0.04	20.94±0.14	*	0.52±0.09
00 39 30.96	-35 29 54.09	24.42±0.06	24.40±0.04	24.08±0.04	23.74±0.05	*	*	0.69±0.04
00 39 40.69	-35 29 53.48	24.79±0.06	24.60±0.04	24.47±0.05	24.10±0.07	21.66±0.19	*	1.61±0.01
00 39 42.01	-35 29 54.29	24.03±0.06	23.75±0.03	23.22±0.02	22.57±0.03	21.69±0.19	*	0.74±0.36
00 39 44.86	-35 29 53.23	24.40±0.06	24.10±0.04	23.83±0.04	23.24±0.04	21.55±0.18	21.05±0.22	0.96±0.26
00 39 47.93	-35 29 51.00	24.97±0.07	24.79±0.05	24.34±0.05	23.84±0.06	21.89±0.21	*	0.69±0.06
00 39 38.61	-35 29 51.93	25.40±0.08	24.23±0.04	23.55±0.03	22.99±0.04	21.29±0.16	*	0.04±0.19
00 39 33.95	-35 29 46.02	24.56±0.06	24.42±0.04	24.19±0.04	23.97±0.06	*	*	0.43±0.12
00 39 31.11	-35 29 44.14	24.72±0.06	24.53±0.04	24.36±0.04	24.05±0.06	23.32±0.38	*	1.04±0.00
00 39 41.05	-35 29 42.28	25.66±0.08	25.02±0.05	24.66±0.05	24.48±0.08	23.14±0.33	*	0.37±0.26
00 39 42.33	-35 29 44.72	24.03±0.06	23.95±0.04	23.78±0.03	23.31±0.05	21.67±0.20	*	0.85±0.07
00 39 44.04	-35 29 43.22	24.33±0.06	22.86±0.02	21.91±0.01	20.82±0.02	18.76±0.08	18.62±0.08	0.72±0.09
00 39 39.92	-35 29 40.44	24.55±0.06	24.44±0.04	24.26±0.04	23.98±0.06	*	*	0.76±0.19
00 39 44.06	-35 29 40.06	25.18±0.07	25.32±0.07	25.13±0.07	24.41±0.08	*	*	0.93±0.42
00 39 43.12	-35 29 39.77	24.79±0.06	24.40±0.04	23.64±0.03	23.13±0.04	*	*	0.63±0.01
00 39 38.84	-35 29 39.11	25.20±0.07	24.90±0.05	24.42±0.04	23.50±0.04	*	*	0.86±0.02
00 39 37.27	-35 29 39.62	25.41±0.08	24.81±0.05	24.17±0.04	23.65±0.05	22.90±0.32	*	0.61±0.09
00 39 41.29	-35 29 39.51	23.90±0.05	23.53±0.03	23.00±0.02	22.38±0.03	19.82±0.09	19.08±0.10	1.33±0.09
00 39 31.41	-35 29 36.24	26.25±0.10	24.95±0.05	24.17±0.04	23.35±0.04	*	*	0.61±0.04
00 39 36.72	-35 29 30.05	21.92±0.05	20.86±0.02	20.40±0.01	19.81±0.02	17.81±0.07	17.13±0.07	0.19±0.16
00 39 43.11	-35 29 33.44	24.73±0.06	24.31±0.04	23.76±0.03	22.86±0.03	21.22±0.16	20.07±0.15	0.84±0.16
00 39 30.62	-35 28 21.75	16.37±0.05	16.11±0.02	15.82±0.01	15.30±0.02	12.68±0.07	12.57±0.06	1.52±0.01
00 39 40.34	-35 29 33.81	24.31±0.06	24.30±0.04	23.98±0.04	23.37±0.05	21.53±0.18	*	1.08±0.20
00 39 48.59	-35 29 32.55	23.99±0.06	23.65±0.03	23.22±0.02	22.38±0.03	20.29±0.11	19.73±0.13	0.98±0.06
00 39 49.42	-35 29 31.98	24.60±0.06	24.44±0.04	24.14±0.04	23.65±0.05	21.53±0.18	21.34±0.27	1.40±0.22
00 39 35.50	-35 29 29.07	26.36±0.11	25.86±0.08	25.40±0.08	24.27±0.06	*	*	0.87±0.15
00 39 40.77	-35 29 29.87	24.84±0.06	24.19±0.04	23.34±0.02	22.62±0.03	20.42±0.11	19.45±0.12	0.61±0.26
00 39 39.85	-35 29 28.07	22.61±0.05	22.48±0.02	22.07±0.01	21.48±0.02	20.69±0.13	20.14±0.17	0.75±0.03
00 39 44.65	-35 29 26.59	24.12±0.06	22.43±0.02	21.46±0.01	20.41±0.02	18.32±0.07	18.24±0.08	0.63±0.19
00 39 37.23	-35 29 17.06	19.02±0.05	18.84±0.02	18.74±0.01	18.41±0.02	16.86±0.07	16.12±0.06	1.50±0.05
00 39 32.58	-35 29 24.14	25.47±0.08	25.07±0.05	24.89±0.06	24.39±0.07	*	*	1.00±0.17
00 39 31.22	-35 29 25.56	24.37±0.06	24.01±0.03	23.24±0.02	22.46±0.03	21.41±0.17	20.89±0.21	0.74±0.01
00 39 37.88	-35 29 21.42	26.15±0.10	25.63±0.07	24.81±0.06	24.36±0.07	*	*	0.58±0.17
00 39 35.62	-35 29 21.52	25.32±0.07	24.42±0.04	23.86±0.03	23.37±0.04	*	*	0.43±0.14
00 39 34.48	-35 29 21.36	25.12±0.07	25.11±0.05	24.94±0.06	24.19±0.06	*	*	0.92±0.48
00 39 42.74	-35 29 22.51	25.47±0.08	25.08±0.06	24.60±0.05	24.25±0.07	22.12±0.23	20.37±0.17	1.27±0.05
00 39 48.02	-35 29 20.82	24.17±0.06	22.95±0.03	22.35±0.02	21.79±0.03	20.02±0.10	19.58±0.13	0.06±0.01
00 39 34.06	-35 29 20.59	24.42±0.06	23.98±0.04	23.76±0.03	23.03±0.04	*	*	0.85±0.16
00 39 30.57	-35 29 20.61	28.06±0.24	25.73±0.08	24.68±0.05	23.37±0.04	*	19.53±0.12	0.76±0.17
00 39 41.38	-35 29 20.16	23.42±0.05	23.31±0.03	23.00±0.02	22.32±0.03	20.36±0.12	20.93±0.21	1.01±0.21
00 39 45.78	-35 29 15.33	22.42±0.05	21.14±0.02	20.54±0.01	19.85±0.02	17.56±0.07	16.81±0.06	0.21±0.14
00 39 36.87	-35 29 10.25	21.57±0.05	19.87±0.02	18.96±0.01	17.99±0.02	15.63±0.07	15.34±0.06	0.32±0.01
00 39 40.71	-35 29 18.13	25.76±0.09	25.02±0.05	24.30±0.04	23.57±0.05	20.21±0.10	19.06±0.10	1.33±0.05
00 39 32.67	-35 29 19.19	25.01±0.07	23.95±0.03	23.09±0.02	22.28±0.03	19.52±0.09	18.96±0.10	0.40±0.04
00 39 41.32	-35 29 17.96	*	24.46±0.04	23.12±0.02	21.78±0.02	18.86±0.08	17.99±0.07	0.88±0.50
00 39 31.26	-35 29 06.76	20.94±0.05	19.63±0.02	18.92±0.01	18.19±0.02	16.07±0.07	15.93±0.06	0.02±0.23
00 39 32.87	-35 29 13.23	24.97±0.07	24.95±0.05	24.91±0.06	24.36±0.07	*	*	0.88±0.19
00 39 45.11	-35 29 12.21	23.74±0.05	23.67±0.03	23.46±0.03	22.98±0.04	22.96±0.34	21.01±0.23	0.89±0.17
00 39 48.20	-35 29 12.13	24.92±0.07	24.72±0.05	24.31±0.04	23.41±0.05	22.75±0.28	*	0.92±0.01
00 39 34.71	-35 29 10.58	25.56±0.08	25.29±0.06	24.72±0.05	23.73±0.05	21.05±0.14	20.90±0.22	0.91±0.37
00 39 38.52	-35 29 09.30	25.60±0.08	25.14±0.05	25.02±0.06	24.36±0.07	21.92±0.21	21.70±0.30	1.55±0.68
00 39 37.61	-35 29 05.85	26.37±0.11	26.02±0.08	25.42±0.08	24.35±0.07	*	21.87±0.34	0.95±0.07
00 39 49.00	-35 29 08.38	24.75±0.06	23.71±0.03	22.93±0.02	21.85±0.03	18.90±0.08	17.91±0.07	1.36±0.07
00 39 36.34	-35 29 07.11	23.75±0.05	23.39±0.03	22.77±0.02	22.08±0.03	20.86±0.13	20.28±0.16	0.73±0.02

Table A.1 – continued

RA	DEC	B [mag]	V [mag]	R [mag]	I [mag]	H [mag]	Ks [mag]	z
00 39 37.27	-35 29 04.35	24.81±0.07	24.59±0.05	24.20±0.04	23.79±0.06	23.38±0.40	*	0.68±0.06
00 39 48.30	-35 29 03.34	25.60±0.08	25.25±0.06	24.68±0.05	24.23±0.06	*	*	0.61±0.08
00 39 49.37	-35 29 04.60	25.03±0.07	24.64±0.04	24.00±0.04	23.51±0.05	23.69±0.51	*	0.62±0.22
00 39 38.41	-35 29 02.53	25.35±0.07	24.97±0.05	24.39±0.04	23.40±0.04	22.06±0.23	20.87±0.19	0.93±0.22
00 39 33.38	-35 28 57.58	25.27±0.07	24.62±0.05	23.86±0.03	23.49±0.05	*	22.01±0.33	0.51±0.15
00 39 47.64	-35 28 57.56	25.53±0.08	25.16±0.06	24.76±0.06	23.78±0.06	*	*	0.85±0.11
00 39 44.92	-35 28 45.58	20.58±0.05	19.68±0.02	19.27±0.01	18.70±0.02	16.81±0.07	16.15±0.06	0.10±0.26
00 39 35.79	-35 28 57.42	24.42±0.06	24.35±0.04	24.10±0.04	23.73±0.05	*	*	0.75±0.06
00 39 46.77	-35 28 54.88	24.90±0.07	23.12±0.03	22.04±0.01	21.20±0.02	18.85±0.08	18.11±0.08	0.35±0.01
00 39 30.81	-35 28 55.08	25.46±0.08	25.15±0.06	24.68±0.05	23.75±0.05	*	*	0.86±0.17
00 39 36.14	-35 28 51.68	24.54±0.06	24.05±0.03	23.49±0.03	22.71±0.03	20.53±0.12	19.54±0.12	1.12±0.04
00 39 39.43	-35 28 51.51	24.40±0.06	24.28±0.04	23.87±0.03	23.14±0.04	22.17±0.25	*	0.93±0.02
00 39 42.02	-35 28 49.30	24.48±0.06	24.41±0.04	24.20±0.04	23.93±0.06	*	*	0.68±0.09
00 39 46.80	-35 28 45.38	24.08±0.06	22.58±0.02	21.58±0.01	20.84±0.02	18.50±0.08	18.02±0.07	0.34±0.35
00 39 43.46	-35 28 46.41	25.29±0.07	25.03±0.06	24.50±0.05	23.90±0.06	*	*	0.71±0.02
00 39 43.40	-35 28 45.00	*	*	25.26±0.08	23.60±0.05	20.06±0.10	19.39±0.11	0.75±0.22
00 39 31.82	-35 28 45.64	23.01±0.05	22.80±0.02	22.48±0.02	21.74±0.03	*	20.13±0.16	0.86±0.30
00 39 43.24	-35 28 44.87	*	25.37±0.06	23.96±0.03	22.33±0.03	19.99±0.10	19.53±0.12	0.82±0.12
00 39 31.50	-35 28 45.50	23.83±0.05	23.34±0.03	22.77±0.02	21.90±0.03	*	18.98±0.10	0.81±0.03
00 39 37.57	-35 28 43.95	27.16±0.15	25.73±0.08	24.66±0.05	23.53±0.05	21.81±0.20	*	0.72±0.18
00 39 44.99	-35 28 42.74	24.42±0.06	24.27±0.03	23.81±0.03	22.97±0.03	21.33±0.16	*	0.93±0.16
00 39 42.62	-35 28 42.92	25.74±0.09	25.59±0.08	24.87±0.06	24.19±0.07	*	*	0.75±0.07
00 39 35.68	-35 28 42.70	24.86±0.07	24.99±0.05	24.82±0.06	24.47±0.08	*	*	0.86±0.23
00 39 35.19	-35 28 42.27	*	26.11±0.09	24.68±0.05	23.32±0.04	19.76±0.10	18.76±0.09	1.38±0.22
00 39 39.05	-35 28 42.55	24.79±0.06	24.67±0.04	24.56±0.05	24.33±0.07	*	*	1.21±0.02
00 39 31.23	-35 28 41.59	26.31±0.11	25.77±0.08	25.40±0.08	24.33±0.08	*	*	0.85±0.16
00 39 32.63	-35 28 40.24	27.25±0.17	25.68±0.08	24.50±0.05	23.31±0.04	21.54±0.18	20.22±0.17	0.75±0.04
00 39 46.02	-35 28 33.18	24.39±0.06	22.65±0.02	21.59±0.01	20.82±0.02	18.44±0.08	17.62±0.07	0.35±0.06
00 39 30.59	-35 28 37.34	24.69±0.06	24.22±0.04	23.79±0.03	22.67±0.03	*	20.20±0.16	0.87±0.07
00 39 35.04	-35 28 36.00	22.83±0.05	21.21±0.02	20.12±0.01	18.78±0.02	16.43±0.07	16.20±0.06	0.85±0.04
00 39 49.90	-35 28 40.58	24.26±0.06	23.93±0.03	23.31±0.02	22.53±0.03	21.23±0.16	*	0.76±0.03
00 39 47.98	-35 28 34.17	24.35±0.06	22.77±0.02	21.91±0.01	21.19±0.02	18.99±0.08	17.98±0.08	0.28±0.03
00 39 47.29	-35 28 35.90	24.41±0.06	23.85±0.03	23.17±0.03	22.43±0.03	20.11±0.11	19.69±0.13	0.70±0.01
00 39 43.10	-35 28 39.83	24.28±0.06	24.15±0.03	23.83±0.03	23.22±0.04	21.93±0.22	*	0.82±0.02
00 39 41.22	-35 28 37.74	24.62±0.06	24.50±0.04	24.43±0.04	24.18±0.07	*	*	1.05±0.14
00 39 47.78	-35 28 38.77	24.93±0.07	24.87±0.05	24.24±0.04	23.56±0.05	22.74±0.31	21.21±0.23	0.73±0.43
00 39 31.49	-35 28 33.08	24.37±0.06	23.81±0.03	23.56±0.03	22.89±0.04	*	*	0.80±0.10
00 39 29.97	-35 28 37.20	26.36±0.11	25.14±0.06	24.04±0.04	22.88±0.04	*	19.48±0.12	0.76±0.32
00 39 32.23	-35 28 34.25	24.28±0.06	23.54±0.03	22.68±0.02	21.60±0.03	18.23±0.08	17.34±0.07	1.32±0.66
00 39 30.79	-35 28 34.28	25.39±0.08	24.97±0.06	23.67±0.04	22.79±0.04	*	*	0.67±0.19
00 39 29.82	-35 28 34.81	24.82±0.07	24.22±0.04	24.05±0.04	22.99±0.04	*	*	0.85±0.32
00 39 39.33	-35 28 35.72	25.14±0.07	24.46±0.04	23.78±0.03	23.48±0.05	*	*	0.44±0.30
00 39 30.33	-35 28 31.90	24.13±0.06	23.98±0.04	24.03±0.05	22.72±0.04	*	*	0.90±0.42
00 39 33.98	-35 28 31.42	23.42±0.05	22.31±0.02	21.87±0.01	21.37±0.02	19.87±0.10	19.64±0.13	0.05±0.24
00 39 37.54	-35 28 30.64	24.92±0.07	23.31±0.03	22.51±0.02	21.78±0.03	19.18±0.09	18.43±0.08	0.25±0.16
00 39 40.96	-35 28 33.48	24.82±0.07	24.68±0.04	24.54±0.05	24.19±0.07	*	21.27±0.24	1.10±0.23
00 39 47.64	-35 28 30.94	27.88±0.22	25.28±0.06	24.23±0.04	22.91±0.03	21.02±0.14	*	0.76±0.29
00 39 31.54	-35 28 28.26	24.25±0.06	25.88±0.09	25.36±0.09	22.92±0.05	*	*	0.92±0.51
00 39 43.05	-35 28 30.76	25.84±0.09	24.65±0.04	23.82±0.03	23.19±0.04	21.60±0.19	*	0.38±0.17
00 39 33.43	-35 28 30.57	24.94±0.07	24.71±0.05	24.47±0.05	24.17±0.07	*	*	0.64±0.02
00 39 47.14	-35 28 31.56	25.40±0.08	24.90±0.05	24.43±0.05	24.14±0.06	*	*	0.43±0.19
00 39 44.41	-35 28 06.94	23.44±0.05	23.01±0.03	22.35±0.02	21.74±0.03	20.62±0.12	*	0.65±0.14
00 39 31.42	-35 28 24.90	23.18±0.05	23.27±0.03	23.02±0.03	21.61±0.03	*	*	0.88±0.09
00 39 50.14	-35 28 15.30	23.58±0.05	23.22±0.03	22.58±0.02	21.94±0.03	20.48±0.12	20.03±0.15	0.70±0.12
00 39 48.25	-35 28 14.02	*	25.38±0.07	23.73±0.03	22.34±0.03	19.78±0.09	19.00±0.10	0.82±0.00
00 39 42.34	-35 28 15.42	24.09±0.06	24.00±0.03	23.62±0.03	23.01±0.04	*	22.01±0.33	0.79±0.37

Table A.1 – continued

RA	DEC	B [mag]	V [mag]	R [mag]	I [mag]	H [mag]	Ks [mag]	z
00 39 39.03	-35 28 15.95	25.01±0.07	24.87±0.05	24.77±0.06	24.10±0.07	21.82±0.20	21.13±0.23	1.50±0.02
00 39 37.91	-35 26 37.91	21.41±0.05	20.30±0.02	19.55±0.01	18.88±0.02	16.63±0.07	15.92±0.06	0.36±0.03
00 39 42.39	-35 26 47.01	20.88±0.05	20.05±0.02	19.61±0.01	19.13±0.02	17.60±0.07	17.53±0.07	0.02±0.01
00 39 41.53	-35 28 07.54	25.61±0.08	24.93±0.05	24.40±0.05	23.91±0.06	23.27±0.37	*	0.43±0.05
00 39 33.97	-35 26 37.63	24.80±0.06	24.34±0.04	24.04±0.04	23.97±0.06	23.11±0.33	*	0.37±0.07
00 39 47.47	-35 26 39.21	22.09±0.05	21.51±0.02	20.87±0.01	20.37±0.02	18.77±0.08	18.16±0.08	0.43±0.31
00 39 41.84	-35 26 57.89	24.89±0.06	24.76±0.05	24.64±0.05	24.40±0.07	*	*	1.18±0.19
00 39 44.46	-35 26 39.43	23.28±0.05	22.50±0.02	21.84±0.01	21.28±0.02	19.12±0.08	18.60±0.09	0.02±0.21
00 39 47.63	-35 26 43.47	26.46±0.11	25.30±0.06	24.10±0.04	23.43±0.04	*	*	0.57±0.12
00 39 35.92	-35 26 44.32	24.53±0.06	24.06±0.04	23.69±0.03	22.67±0.03	*	*	0.85±0.24
00 39 29.95	-35 26 44.33	24.82±0.06	23.87±0.03	23.14±0.02	22.19±0.03	*	*	0.69±0.06
00 39 30.13	-35 26 46.02	25.07±0.07	*	23.97±0.04	23.45±0.05	*	*	0.62±0.20
00 39 39.33	-35 26 45.93	23.85±0.05	23.76±0.03	23.51±0.03	23.08±0.04	*	*	0.81±0.32
00 39 45.02	-35 26 44.58	24.38±0.06	24.19±0.04	23.96±0.04	23.90±0.06	*	*	0.43±0.30
00 39 34.05	-35 26 43.72	25.53±0.08	25.40±0.07	25.19±0.07	24.31±0.07	*	*	0.88±0.14
00 39 38.00	-35 26 46.93	24.69±0.06	24.52±0.04	24.23±0.04	24.07±0.07	*	*	0.46±0.22
00 39 36.25	-35 26 47.46	25.01±0.07	24.86±0.05	24.40±0.05	24.14±0.07	*	*	0.58±0.32
00 39 43.97	-35 26 50.53	24.49±0.06	23.81±0.03	22.93±0.02	22.22±0.03	*	20.96±0.22	0.65±0.08
00 39 31.04	-35 26 51.21	26.71±0.13	25.40±0.06	24.83±0.06	24.09±0.07	*	*	0.14±0.07
00 39 37.65	-35 26 53.86	24.25±0.06	23.95±0.03	23.76±0.03	23.55±0.05	22.12±0.24	*	0.05±0.06
00 39 30.71	-35 26 55.24	23.30±0.05	23.21±0.03	22.88±0.02	22.42±0.03	21.09±0.16	21.12±0.25	0.73±0.25
00 39 29.99	-35 26 56.95	23.69±0.05	23.42±0.03	22.87±0.02	22.05±0.03	*	*	0.76±0.04
00 39 34.05	-35 27 03.08	19.26±0.05	18.89±0.02	18.74±0.01	18.28±0.02	17.16±0.07	17.14±0.06	1.06±0.07
00 39 34.05	-35 26 57.89	25.01±0.07	24.82±0.05	24.58±0.05	24.33±0.07	*	*	0.43±0.00
00 39 45.80	-35 26 55.90	25.79±0.09	24.98±0.05	24.23±0.04	23.84±0.06	*		0.49±0.03
00 39 44.22	-35 26 59.38	26.57±0.11	25.62±0.07	25.01±0.06	23.64±0.05	*	*	0.85±0.10
00 39 42.12	-35 27 04.56	25.71±0.08	25.61±0.07	25.10±0.07	24.45±0.08	21.18±0.16	*	1.26±0.09
00 39 41.77	-35 27 02.47	24.77±0.06	24.77±0.05	24.24±0.04	23.69±0.05	21.18±0.16	20.82±0.21	1.30±0.01
00 39 41.75	-35 27 05.36	24.47±0.06	24.27±0.04	23.89±0.03	23.02±0.04	21.38±0.17	21.48±0.28	0.85±0.07
00 39 31.62	-35 27 06.24	24.56±0.06	24.35±0.04	24.47±0.05	23.74±0.06	*	*	0.90±0.20
00 39 46.45	-35 27 03.27	25.64±0.08	25.78±0.08	25.22±0.08	24.20±0.07	*	*	1.00±0.06
00 39 35.66	-35 27 40.57	24.49±0.06	24.07±0.04	23.71±0.04	22.87±0.04	20.86±0.14	22.28±0.41	0.85±0.26
00 39 37.55	-35 27 12.94	26.64±0.12	24.23±0.04	22.94±0.02	21.55±0.02	18.73±0.08	18.08±0.08	0.75±0.17
00 39 38.17	-35 28 06.43	26.58±0.12	25.53±0.07	24.63±0.05	23.47±0.05	20.53±0.12	19.70±0.13	1.39±0.15
00 39 46.27	-35 27 09.90	23.18±0.05	21.94±0.02	21.02±0.01	20.32±0.02	17.75±0.07	16.95±0.06	0.40±0.15
00 39 44.15	-35 27 15.92	25.06±0.07	25.12±0.05	24.77±0.05	24.20±0.06	*	*	0.79±0.38
00 39 49.47	-35 27 15.84	25.85±0.09	24.93±0.05	24.51±0.05	24.21±0.07	*	21.17±0.22	0.37±0.02
00 39 49.20	-35 27 18.49	24.18±0.06	23.61±0.03	22.86±0.02	22.08±0.03	19.66±0.09	18.72±0.09	1.16±0.03
00 39 47.32	-35 27 19.16	25.94±0.10	24.72±0.05	23.85±0.03	22.28±0.03	*	19.92±0.13	0.84±0.29
00 39 36.08	-35 27 18.86	24.06±0.06	23.98±0.04	23.57±0.03	23.02±0.04	22.50±0.28	*	0.79±0.21
00 39 49.87	-35 27 20.14	25.24±0.08	24.73±0.05	23.96±0.04	22.97±0.04	20.03±0.10	*	0.79±0.20
00 39 36.75	-35 27 21.22	28.35±0.28	26.39±0.11	25.59±0.09	24.45±0.08	*	*	0.71±0.10
00 39 38.82	-35 27 21.67	24.49±0.06	23.72±0.03	23.15±0.02	22.63±0.03	20.98±0.14	*	0.02±0.07
00 39 31.91	-35 27 24.76	23.16±0.05	22.46±0.02	21.66±0.01	21.05±0.02	19.04±0.09	19.48±0.12	0.61±0.08
00 39 42.96	-35 27 19.90	24.73±0.06	24.08±0.04	23.61±0.03	23.26±0.04	22.80±0.30	*	0.42±0.28
00 39 44.50	-35 27 24.19	26.74±0.13	24.94±0.05	24.20±0.04	23.40±0.04	22.39±0.26	*	0.40±0.17
00 39 39.85	-35 27 24.85	26.22±0.11	25.38±0.06	24.48±0.05	23.76±0.05	20.25±0.11	18.97±0.10	1.33±0.09
00 39 32.11	-35 27 28.39	25.00±0.07	24.00±0.03	23.51±0.03	23.04±0.04	20.90±0.14	*	0.02±0.12
00 39 44.57	-35 27 30.30	23.23±0.05	22.56±0.02	22.10±0.01	21.27±0.02	19.63±0.09	19.83±0.13	0.80±0.44
00 39 44.44	-35 27 29.02	*	24.69±0.04	23.32±0.02	21.92±0.03	18.95±0.08	17.88±0.07	0.85±0.19
00 39 43.99	-35 27 29.50	26.00±0.10	25.50±0.07	24.73±0.05	24.03±0.06	*	*	0.69±0.09
00 39 45.49	-35 27 31.25	26.88±0.14	24.96±0.05	23.32±0.02	21.69±0.02	19.18±0.08	18.92±0.09	0.82±0.01
00 39 41.70	-35 27 34.71	25.41±0.08	24.01±0.03	22.97±0.02	21.76±0.02	19.03±0.08	18.24±0.08	0.68±0.08
00 39 33.60	-35 27 37.11	23.75±0.05	23.41±0.03	22.88±0.02	21.97±0.03	*	19.14±0.11	0.83±0.22
00 39 40.15	-35 27 35.45	25.36±0.08	25.25±0.06	24.87±0.06	24.08±0.07	*	*	0.92±0.49
00 39 38.74	-35 27 40.72	24.08±0.06	25.53±0.05	*	24.15±0.06	*	*	0.93±0.13

Table A.1 – continued

RA	DEC	B [mag]	V [mag]	R [mag]	I [mag]	H [mag]	Ks [mag]	z
00 39 40.32	-35 27 40.95	26.96±0.14	26.09±0.09	25.03±0.06	24.06±0.06	21.88±0.21	*	0.70±0.11
00 39 36.85	-35 27 43.21	26.14±0.10	25.40±0.07	24.73±0.06	24.33±0.08	*	21.86±0.29	0.43±0.10
00 39 38.82	-35 27 38.91	21.64±0.05	20.68±0.02	20.14±0.01	19.63±0.02	17.91±0.07	17.88±0.07	0.02±0.30
00 39 41.92	-35 27 39.99	23.97±0.06	23.75±0.03	23.17±0.03	22.56±0.03	20.41±0.12	19.88±0.14	1.18±0.02
00 39 41.85	-35 27 44.98	26.48±0.12	25.42±0.07	24.44±0.04	23.61±0.05	*	*	0.64±0.07
00 39 38.38	-35 27 41.12	25.35±0.08	25.06±0.06	24.23±0.04	23.13±0.04	19.96±0.10	19.04±0.10	1.07±0.41
00 39 33.48	-35 27 40.91	24.80±0.06	24.71±0.05	24.42±0.05	24.03±0.06	*	*	0.75±0.05
00 39 41.75	-35 27 40.27	24.63±0.06	24.43±0.04	23.93±0.03	23.24±0.04	*	*	0.75±0.03
00 39 41.98	-35 27 42.75	22.58±0.05	22.37±0.02	21.81±0.01	21.19±0.02	19.98±0.10	20.54±0.20	0.69±0.09
00 39 41.25	-35 27 43.85	25.15±0.07	24.83±0.05	24.53±0.05	23.49±0.05	*	*	0.90±0.09
00 39 46.56	-35 27 46.63	24.44±0.06	23.09±0.03	22.33±0.01	21.55±0.02	18.84±0.08	17.98±0.08	0.34±0.03
00 39 34.92	-35 27 40.62	24.93±0.07	24.25±0.04	23.92±0.03	23.35±0.04	20.19±0.11	19.74±0.14	1.79±0.53
00 39 35.00	-35 27 46.97	22.96±0.05	21.39±0.02	20.56±0.01	19.74±0.02	17.78±0.07	17.53±0.07	0.32±0.00
00 39 45.28	-35 27 49.22	*	25.75±0.08	24.43±0.04	23.00±0.04	20.61±0.12	20.78±0.22	0.79±0.06
00 39 42.69	-35 28 05.91	23.94±0.06	23.55±0.03	23.49±0.03	23.26±0.04	21.86±0.20	20.61±0.20	0.28±0.18
00 39 41.82	-35 27 53.75	25.84±0.09	25.67±0.07	25.08±0.07	23.98±0.06	*	*	0.90±0.00
00 39 42.68	-35 27 52.28	24.33±0.06	23.56±0.03	22.78±0.02	22.16±0.03	20.25±0.11	20.56±0.19	0.61±0.18
00 39 41.11	-35 27 47.94	*	24.91±0.05	23.92±0.03	22.67±0.03	19.62±0.09	19.31±0.11	0.75±0.40
00 39 42.55	-35 27 49.74	22.78±0.05	22.11±0.02	21.29±0.01	20.62±0.02	18.26±0.08	17.46±0.07	0.48±0.39
00 39 45.62	-35 27 51.32	24.76±0.06	24.57±0.04	24.42±0.04	23.99±0.06	21.66±0.18	*	1.62±0.45
00 39 49.91	-35 27 48.15	25.11±0.07	25.10±0.05	24.81±0.06	24.38±0.07	*	*	0.79±0.15
00 39 42.40	-35 27 44.02	26.21±0.10	23.51±0.03	22.15±0.01	20.83±0.02	17.93±0.07	17.14±0.06	0.88±0.33
00 39 42.20	-35 27 56.87	25.25±0.08	23.05±0.03	22.23±0.02	20.92±0.02	18.08±0.07	17.29±0.07	0.74±0.03
00 39 41.90	-35 27 55.70	*	24.84±0.05	23.56±0.03	22.14±0.03	19.80±0.09	18.82±0.09	0.75±0.01
00 39 40.86	-35 27 53.09	26.59±0.12	23.60±0.03	21.99±0.01	20.54±0.02	17.47±0.07	16.52±0.06	0.82±0.11
00 39 43.13	-35 27 50.28	25.97±0.09	25.34±0.06	24.54±0.05	23.45±0.05	*	19.83±0.14	0.81±0.01
00 39 42.51	-35 28 00.83	18.27±0.05	18.23±0.02	18.28±0.01	17.90±0.02	16.25±0.07	15.58±0.06	1.50±0.16
00 39 38.15	-35 27 51.51	25.60±0.08	24.50±0.04	23.86±0.03	23.26±0.04	22.35±0.25	21.30±0.26	0.36±0.19
00 39 40.67	-35 27 51.36	*	25.47±0.07	23.88±0.03	22.56±0.03	19.82±0.09	18.96±0.10	0.86±0.15
00 39 33.19	-35 28 00.11	24.71±0.06	24.50±0.04	24.27±0.04	23.89±0.06	*	*	0.84±0.12
00 39 39.08	-35 27 54.74	25.04±0.07	24.92±0.05	24.92±0.06	24.48±0.08	*	*	0.98±0.12
00 39 41.20	-35 27 54.14	26.45±0.11	25.38±0.06	24.80±0.05	24.41±0.07	*	*	0.42±0.31
00 39 39.96	-35 27 42.95	26.39±0.11	24.40±0.04	23.17±0.02	21.81±0.03	19.14±0.08	18.23±0.08	0.84±0.04
00 39 38.71	-35 27 55.02	26.83±0.14	26.02±0.09	25.15±0.06	23.95±0.06	22.00±0.22	20.50±0.19	0.94±0.03
00 39 44.56	-35 27 55.95	23.35±0.05	22.65±0.02	21.93±0.01	21.08±0.02	18.56±0.08	17.39±0.07	1.16±0.15
00 39 44.51	-35 27 57.21	*	24.25±0.03	22.90±0.02	21.62±0.02	18.63±0.08	17.91±0.07	0.88±0.04
00 39 38.58	-35 27 57.27	23.57±0.05	23.45±0.03	23.10±0.02	22.42±0.03	*	*	0.86±0.12
00 39 44.75	-35 28 09.04	25.35±0.08	24.81±0.05	24.02±0.04	23.00±0.04	*	*	0.79±0.33
00 39 43.31	-35 27 52.64	24.06±0.06	23.28±0.03	22.48±0.02	21.74±0.02	19.60±0.09	18.91±0.09	0.61±0.26
00 39 49.39	-35 28 01.29	24.57±0.06	23.94±0.03	23.33±0.03	22.59±0.03	20.82±0.14	20.95±0.22	0.72±0.20
00 39 43.82	-35 28 03.04	20.60±0.05	19.71±0.02	19.30±0.01	18.70±0.02	16.73±0.07	16.15±0.06	0.10±0.01
00 39 33.00	-35 28 03.53	25.16±0.07	24.80±0.05	24.50±0.05	23.46±0.05	23.00±0.34	*	0.88±0.13
00 39 47.78	-35 28 03.12	25.83±0.09	25.39±0.06	24.55±0.05	23.85±0.05	22.62±0.26	*	0.69±0.40
00 39 40.06	-35 28 09.44	24.22±0.06	23.79±0.03	23.34±0.03	23.18±0.04	*	21.64±0.28	0.43±0.34
00 39 34.11	-35 28 05.15	24.72±0.06	24.50±0.05	24.24±0.05	23.91±0.06	*	*	0.64±0.16
00 39 36.49	-35 28 05.29	25.61±0.09	24.63±0.04	23.53±0.03	22.65±0.03	19.94±0.10	19.22±0.11	0.55±0.23
00 39 40.76	-35 28 05.87	*	25.73±0.08	24.84±0.06	23.56±0.05	20.56±0.12	19.35±0.11	1.38±0.01
00 39 36.08	-35 28 09.33	24.37±0.06	23.48±0.03	22.36±0.02	21.21±0.02	18.00±0.07	17.02±0.06	1.28±0.01
00 39 37.25	-35 28 15.26	25.65±0.08	25.47±0.07	25.15±0.07	24.34±0.07	*	*	0.92±0.26
00 39 45.81	-35 28 12.16	25.43±0.08	25.34±0.06	24.99±0.07	24.35±0.08	22.47±0.26	21.99±0.32	1.07±0.10
00 39 47.90	-35 28 21.40	24.18±0.06	24.19±0.04	23.78±0.03	23.42±0.05	*	*	0.67±0.36
00 39 37.77	-35 28 12.44	24.64±0.06	24.56±0.04	24.32±0.04	23.93±0.06	*	*	0.81±0.23
00 39 37.01	-35 28 18.86	26.24±0.11	25.53±0.07	24.28±0.04	23.10±0.04	19.26±0.08	18.14±0.08	1.04±0.04
00 39 38.62	-35 28 17.43	25.07±0.07	25.05±0.05	25.03±0.07	24.41±0.08	*	*	0.90±0.55
00 39 39.15	-35 28 21.07	*	26.67±0.13	24.62±0.05	23.06±0.04	19.48±0.09	18.42±0.08	11.28±0.11
00 39 40.71	-35 28 18.51	25.46±0.08	25.09±0.05	24.47±0.04	23.46±0.04	21.38±0.17	21.74±0.31	0.90±0.04

Table A.1 – continued

RA	DEC	B [mag]	V [mag]	R [mag]	I [mag]	H [mag]	Ks [mag]	z
00 39 36.63	-35 28 09.51	24.80±0.06	24.43±0.04	23.74±0.03	23.03±0.04	*	21.12±0.23	0.72±0.07
00 39 34.26	-35 28 17.80	26.16±0.10	26.16±0.10	25.33±0.08	24.36±0.07	* *	*	0.82±0.07
00 39 45.91	-35 28 20.40	24.58±0.06	24.37±0.04	24.07±0.03	23.90±0.05	22.71±0.28	22.32±0.42	0.42±0.06
00 39 36.16	-35 28 24.80	25.75±0.09	24.91±0.05	24.44±0.05	24.24±0.07	22.97±0.29	*	0.38±0.14
00 39 41.43	-35 28 21.85	26.53±0.12	24.32±0.04	23.06±0.02	21.66±0.03	19.16±0.08	18.46±0.08	0.80±0.44
00 39 35.58	-35 28 22.57	23.77±0.05	23.69±0.03	23.59±0.03	23.43±0.05	*	*	0.05±0.28
00 39 48.83	-35 28 20.42	26.22±0.10	25.70±0.07	24.97±0.06	24.27±0.07	*	*	0.69±0.01
00 39 37.73	-35 28 26.48	25.95±0.09	25.58±0.07	24.88±0.06	24.17±0.06	21.58±0.18	21.45±0.28	1.13±0.07
00 39 39.48	-35 28 27.65	*	25.28±0.06	23.94±0.03	22.60±0.03	19.53±0.09	18.42±0.08	0.88±0.19
00 39 43.47	-35 28 30.08	24.54±0.06	24.28±0.04	23.68±0.03	22.86±0.03	22.09±0.23	20.59±0.20	0.81±0.25
00 39 40.63	-35 28 29.50	25.76±0.08	23.85±0.03	22.91±0.02	22.04±0.02	20.31±0.11	20.55±0.18	0.53±0.06
00 39 43.01	-35 28 13.17	26.86±0.13	25.66±0.07	25.13±0.06	23.94±0.05	21.44±0.17	*	0.85±0.54

Appendix B

Light Curves of SDSS J1004+4112

Table B.1: The Heliocentric Julian Days (HJD) column gives the date of the observation relative to HJD= 2450000. The χ^2/N_{dof} column indicates how well our photometric model fit the imaging data. When $\chi^2 > N_{dof}$ we rescale the photometric errors presented in this Table by $(\chi^2/N_{dof})^{1/2}$ before carrying out the time delay analysis to reduce the weight of images that were fit poorly. The image magnitudes are relative to the comparison stars (see Chapter 7). The magnitudes enclosed in parentheses are not used in the time delay estimates.

HJD	χ^2/N_{dof}	Image A	Image B	Image C	Image D	Observatory	Detector
2993.523	0.9	3.18±0.01	3.53±0.02	4.26±0.04	5.15±0.08	FLWO	4Shooter
2994.960	2.2	(3.13±0.01)	(3.47±0.01)	4.22±0.01	4.96±0.03	MDM	8K
2996.599	1.8	3.13±0.05	3.67±0.08	4.37±0.19	5.28±0.41	Wise	Tektronix
2997.344	0.8	3.16±0.02	3.54±0.03	4.39±0.06	5.24±0.13	FLWO	4Shooter
2997.598	2.4	3.11±0.04	3.60±0.06	4.20±0.17	5.44±0.49	Wise	Tektronix
2998.560	52.	3.81±0.04	5.41±0.16	5.78±1.57	6.58±2.98	Wise	Tektronix
3001.632	135	4.05±0.04	5.66±0.15	6.37±3.11	5.99±2.28	Wise	Tektronix
3004.596	53.	3.68±0.03	4.76±0.08	5.62±1.24	6.28±2.13	Wise	Tektronix
3005.538	1.3	3.19±0.03	3.68±0.05	4.48±0.10	5.62±0.27	Wise	Tektronix
3006.519	3.7	3.20±0.02	3.64±0.04	4.39±0.13	5.25±0.27	Wise	Tektronix
3011.405	0.8	3.19±0.05	3.51±0.06	4.30±0.13	6.23±0.60	FLWO	4Shooter
3021.543	3.9	3.06±0.02	3.55±0.03	4.27±0.10	5.09±0.20	Wise	Tektronix
3022.606	1.5	3.12±0.01	3.55±0.02	4.17±0.04	5.42±0.13	FLWO	4Shooter
3024.524	0.8	3.08±0.04	3.47±0.06	4.23±0.12	5.05±0.24	Wise	Tektronix
3031.920	1.5	3.13±0.01	3.59±0.02	4.22±0.04	5.31±0.10	FLWO	4Shooter
3032.920	2.0	3.10±0.01	3.52±0.02	4.16±0.04	5.28±0.11	FLWO	4Shooter
3033.913	2.5	3.09±0.01	3.54±0.02	4.16±0.05	5.27±0.12	FLWO	4Shooter
3034.916	1.0	3.11±0.01	3.57±0.02	4.17±0.03	5.41±0.10	FLWO	4Shooter
3035.382	3.2	3.20±0.06	3.74±0.10	4.10±0.23	6.87±1.85	Wise	TAVAS
3035.909	1.7	3.11±0.01	3.57±0.02	4.24±0.04	5.51±0.13	FLWO	4Shooter
3037.742	0.7	3.06±0.04	3.56±0.06	4.07±0.10	5.47±0.31	FLWO	4Shooter
3038.720	1.5	3.11±0.02	(3.73±0.03)	4.27±0.06	5.46±0.17	MDM	Templeton
3043.854	0.5	3.09±0.03	3.56±0.04	4.37±0.08	5.28±0.17	FLWO	4Shooter
3044.885	1.4	3.12±0.01	3.57±0.02	4.15±0.04	5.42±0.13	FLWO	4Shooter
3045.862	2.7	3.12±0.01	3.57±0.02	4.21±0.05	5.26±0.11	FLWO	4Shooter
3046.908	1.5	3.09±0.01	3.59±0.02	4.18±0.03	5.43±0.10	FLWO	4Shooter
3046.949	1.0	(3.06±0.01)	3.54±0.01	4.18±0.01	5.26±0.03	APO	SPICam
3047.866	3.7	3.10±0.01	3.57±0.01	4.18±0.04	5.39±0.11	FLWO	4Shooter
3048.453	1.1	3.10±0.03	3.65±0.05	4.16±0.08	5.28±0.20	Wise	Tektronix
3048.885	1.4	3.09±0.01	3.58±0.02	4.19±0.03	5.79±0.12	FLWO	4Shooter
3051.850	2.6	3.10±0.01	3.58±0.01	4.16±0.03	5.27±0.09	FLWO	4Shooter
3052.425	1.8	3.07±0.05	3.76±0.08	4.27±0.17	5.21±0.37	Wise	Tektronix
3052.869	2.8	3.10±0.01	3.56±0.02	4.20±0.04	5.36±0.12	FLWO	4Shooter

Table B.1 – continued

HJD	χ^2/N_{dof}	Image A	Image B	Image C	Image D	Observatory	Detector
3053.605	3.5	(3.45±0.04)	(4.16±0.06)	5.18±0.30	7.29±1.48	Wise	Tektronix
3056.349	9.6	1.57±0.30	(0.76±0.15)	3.30±2.97	2.09±1.30	Wise	TAVAS
3057.341	2.1	2.90±0.06	3.67±0.13	4.18±0.28	8.83±4.27	Wise	TAVAS
3057.795	2.8	3.12±0.01	3.54±0.02	4.29±0.06	5.45±0.18	FLWO	4Shooter
3058.362	1.0	2.95±0.12	3.55±0.19	3.64±0.22	4.93±0.62	Wise	TAVAS
3059.347	4.0	3.01±0.07	3.37±0.10	4.16±0.37	8.06±4.43	Wise	TAVAS
3059.856	0.7	3.07±0.02	3.60±0.03	4.17±0.05	5.32±0.14	FLWO	4Shooter
3060.353	2.5	2.89±0.06	3.49±0.12	4.24±0.31	6.30±1.50	Wise	TAVAS
3061.365	3.5	3.14±0.05	3.51±0.07	4.14±0.22	5.44±0.63	Wise	TAVAS
3062.396	4.3	3.15±0.04	3.56±0.05	4.07±0.17	5.69±0.65	Wise	TAVAS
3064.468	35.	3.82±0.05	5.48±0.23	4.42±0.56	6.59±3.32	Wise	Tektronix
3064.773	1.0	3.11±0.02	3.60±0.03	4.20±0.04	5.55±0.14	FLWO	4Shooter
3064.884	1.4	3.12±0.01	3.57±0.01	4.24±0.01	5.25±0.03	MDM	Echelle
3065.480	12.	3.19±0.06	3.96±0.11	4.39±0.60	5.40±1.35	Wise	Tektronix
3065.805	2.9	3.10±0.01	3.55±0.01	4.17±0.03	5.42±0.09	FLWO	4Shooter
3073.862	0.6	3.09±0.02	3.55±0.03	4.16±0.06	5.41±0.18	FLWO	4Shooter
3075.464	1.0	3.09±0.05	3.74±0.08	4.10±0.12	5.36±0.33	Wise	Tektronix
3078.837	1.1	3.08±0.01	3.58±0.02	4.14±0.03	5.44±0.10	FLWO	4Shooter
3079.832	1.8	3.05±0.01	3.53±0.02	4.17±0.04	5.31±0.11	FLWO	4Shooter
3079.848	11.	3.03±0.01	(3.47±0.01)	4.11±0.03	5.06±0.06	MDM	8K
3080.822	1.0	3.08±0.01	3.57±0.02	4.18±0.03	5.68±0.12	FLWO	4Shooter
3081.327	2.1	3.01±0.06	3.45±0.10	4.21±0.25	10.2±5.98	Wise	TAVAS
3081.789	3.1	3.11±0.01	3.59±0.01	4.18±0.04	5.28±0.11	FLWO	4Shooter
3082.785	1.7	3.07±0.01	3.58±0.02	4.22±0.04	5.32±0.09	FLWO	4Shooter
3083.934	1.0	3.11±0.02	3.52±0.03	4.18±0.06	5.42±0.17	FLWO	4Shooter
3085.793	1.5	3.09±0.01	3.54±0.01	4.27±0.03	5.55±0.10	FLWO	4Shooter
3087.662	3.1	3.01±0.06	3.50±0.06	4.36±0.11	5.41±0.11	WIYN	WTTM
3087.707	2.4	3.08±0.01	3.53±0.02	4.26±0.04	5.41±0.12	FLWO	4Shooter
3088.734	2.0	3.06±0.01	3.56±0.02	4.23±0.04	5.53±0.12	FLWO	4Shooter
3090.735	0.6	3.09±0.02	3.59±0.04	4.37±0.07	5.21±0.15	FLWO	4Shooter
3091.772	1.0	3.08±0.01	3.53±0.02	4.26±0.04	5.55±0.12	FLWO	4Shooter
3092.821	0.6	3.07±0.02	3.53±0.03	4.25±0.05	5.57±0.15	FLWO	4Shooter
3093.790	0.7	3.07±0.01	3.55±0.02	4.25±0.04	5.55±0.12	FLWO	4Shooter
3094.718	0.8	3.02±0.02	3.51±0.03	4.27±0.06	5.66±0.21	FLWO	4Shooter
3095.819	0.7	3.08±0.02	3.52±0.04	4.32±0.07	5.39±0.19	FLWO	4Shooter
3100.412	0.4	3.09±0.09	3.53±0.14	4.56±0.33	5.27±0.58	Wise	Tektronix
3101.657	0.4	3.02±0.03	3.46±0.04	4.27±0.08	5.47±0.22	FLWO	4Shooter
3104.747	1.0	3.07±0.02	3.53±0.03	4.24±0.05	5.52±0.14	FLWO	4Shooter
3107.686	1.3	3.03±0.75	3.49±0.75	4.27±0.86	5.25±0.87	WIYN	WTTM
3107.694	0.7	3.07±0.01	3.59±0.02	4.15±0.04	5.42±0.12	FLWO	4Shooter
3108.285	1.8	3.05±0.03	3.61±0.05	4.26±0.12	5.59±0.37	Wise	Tektronix
3108.729	1.6	3.09±0.01	3.54±0.02	4.27±0.04	5.36±0.10	FLWO	4Shooter
3111.688	1.6	3.08±0.01	3.55±0.02	4.20±0.04	5.39±0.11	FLWO	4Shooter
3113.335	0.9	3.07±0.05	3.57±0.08	4.16±0.14	5.48±0.40	Wise	Tektronix
3116.725	1.4	3.12±0.01	3.54±0.02	4.24±0.04	5.30±0.09	FLWO	4Shooter
3117.746	1.4	3.09±0.01	3.57±0.02	4.34±0.04	5.69±0.15	FLWO	4Shooter
3118.764	0.8	3.13±0.01	3.55±0.02	4.26±0.03	5.23±0.08	FLWO	4Shooter
3119.731	0.8	3.08±0.01	3.55±0.02	4.30±0.04	5.45±0.10	FLWO	4Shooter
3120.730	0.7	3.10±0.01	3.56±0.02	4.27±0.04	5.16±0.09	FLWO	4Shooter
3122.786	0.6	3.10±0.03	3.58±0.04	4.23±0.08	5.73±0.28	FLWO	4Shooter
3124.718	0.8	3.08±0.03	3.61±0.04	4.25±0.08	5.17±0.17	FLWO	4Shooter
3125.737	0.5	3.08±0.03	3.52±0.05	4.31±0.10	5.22±0.23	FLWO	4Shooter
3126.717	0.6	3.12±0.03	3.53±0.04	4.20±0.07	5.13±0.16	FLWO	4Shooter
3129.240	0.7	2.99±0.06	3.58±0.09	4.25±0.17	5.12±0.35	Wise	Tektronix
3129.812	0.6	3.12±0.04	3.54±0.05	4.35±0.11	5.00±0.19	FLWO	4Shooter
3132.749	2.1	3.11±0.01	3.60±0.01	4.26±0.03	5.19±0.07	FLWO	4Shooter

Table B.1 – continued

HJD	χ^2/N_{dof}	Image A	Image B	Image C	Image D	Observatory	Detector
3135.717	7.0	3.02±0.01	3.54±0.01	4.14±0.03	5.05±0.06	MDM	8K
3136.659	1.6	3.08±0.01	3.62±0.02	4.19±0.04	5.35±0.11	FLWO	4Shooter
3137.719	1.1	3.05±0.01	3.63±0.02	4.19±0.04	5.21±0.09	FLWO	4Shooter
3140.640	1.6	3.08±0.01	3.64±0.02	4.24±0.04	5.29±0.10	FLWO	4Shooter
3143.790	0.6	3.16±0.03	3.71±0.05	4.18±0.07	5.13±0.16	FLWO	4Shooter
3144.677	1.6	3.09±0.01	3.66±0.02	4.21±0.04	5.26±0.10	FLWO	4Shooter
3145.711	1.5	3.09±0.01	3.66±0.02	4.11±0.04	5.30±0.12	FLWO	4Shooter
3146.745	0.8	3.09±0.01	3.64±0.02	4.20±0.03	5.18±0.08	FLWO	4Shooter
3147.648	1.4	3.10±0.01	3.65±0.02	4.15±0.04	5.22±0.11	FLWO	4Shooter
3148.653	1.3	3.08±0.01	3.68±0.03	4.19±0.05	5.15±0.11	FLWO	4Shooter
3149.733	1.4	3.09±0.01	3.63±0.02	4.12±0.04	5.34±0.10	FLWO	4Shooter
3153.660	1.4	3.06±0.06	3.63±0.06	4.16±0.07	5.16±0.07	WIYN	WTTM
3153.692	0.9	3.12±0.02	3.66±0.03	4.14±0.05	5.17±0.12	FLWO	4Shooter
3154.272	0.3	3.07±0.06	3.58±0.09	4.10±0.15	4.77±0.26	Wise	Tektronix
3154.673	0.7	3.12±0.02	3.69±0.04	4.10±0.05	5.04±0.12	FLWO	4Shooter
3155.673	0.6	3.11±0.02	3.61±0.04	4.08±0.06	5.30±0.16	FLWO	4Shooter
3156.646	0.7	3.11±0.02	3.62±0.03	4.11±0.05	5.23±0.13	FLWO	4Shooter
3157.670	0.7	3.10±0.02	3.69±0.03	4.12±0.05	5.15±0.13	FLWO	4Shooter
3158.660	1.0	3.11±0.02	3.63±0.03	4.08±0.04	5.13±0.10	FLWO	4Shooter
3159.643	0.6	3.14±0.03	3.68±0.05	4.03±0.06	5.27±0.19	FLWO	4Shooter
3161.736	2.9	3.12±0.02	3.66±0.02	4.07±0.06	5.20±0.15	MDM	Templeton
3162.658	2.8	3.15±0.01	3.65±0.01	4.09±0.02	5.09±0.05	MDM	Templeton
3163.650	4.1	3.16±0.01	3.65±0.01	4.11±0.04	5.12±0.09	MDM	Templeton
3164.651	28.	3.17±0.01	3.65±0.01	4.09±0.10	5.05±0.24	MDM	Templeton
3165.656	11.	3.17±0.01	3.62±0.01	4.06±0.05	5.04±0.11	MDM	Templeton
3166.650	3.7	3.14±0.01	3.62±0.01	4.04±0.03	5.06±0.08	MDM	Templeton
3167.665	8.2	3.14±0.01	3.62±0.01	4.18±0.02	5.16±0.03	MDM	Templeton
3168.663	17.	3.15±0.01	3.64±0.01	4.13±0.03	5.16±0.06	MDM	Templeton
3169.662	6.0	3.17±0.01	3.63±0.01	4.11±0.02	5.15±0.04	MDM	Templeton
3169.674	1.1	3.16±0.01	3.64±0.02	3.98±0.03	5.20±0.09	FLWO	4Shooter
3170.259	0.3	3.11±0.05	3.59±0.07	4.00±0.10	5.03±0.25	Wise	Tektronix
3170.667	0.7	3.17±0.01	3.63±0.02	4.03±0.02	5.20±0.06	MDM	Templeton
3170.673	0.6	3.17±0.03	3.69±0.04	4.08±0.06	5.57±0.20	FLWO	4Shooter
3171.271	0.3	3.13±0.05	3.56±0.07	4.06±0.11	5.77±0.46	Wise	Tektronix
3171.661	1.8	3.18±0.01	3.63±0.01	4.07±0.01	5.10±0.03	MDM	Templeton
3171.666	1.2	3.12±0.02	3.63±0.03	4.03±0.05	5.34±0.15	FLWO	4Shooter
3172.664	1.7	3.19±0.01	3.63±0.01	4.10±0.01	5.15±0.03	MDM	Templeton
3172.668	0.7	3.15±0.02	3.59±0.02	3.99±0.03	5.23±0.09	FLWO	4Shooter
3173.658	0.7	3.16±0.02	3.65±0.03	4.02±0.04	5.10±0.09	FLWO	4Shooter
3173.659	4.6	3.21±0.01	3.65±0.01	4.13±0.02	5.20±0.04	MDM	Templeton
3174.664	0.7	3.17±0.02	3.59±0.02	4.09±0.04	5.16±0.09	FLWO	4Shooter
3176.666	1.0	3.17±0.02	3.60±0.02	4.04±0.03	5.22±0.09	FLWO	4Shooter
3177.675	1.1	3.17±0.02	3.66±0.03	4.03±0.04	5.27±0.12	FLWO	4Shooter
3178.675	0.6	3.20±0.03	3.65±0.04	3.97±0.05	4.98±0.13	FLWO	4Shooter
3182.654	0.7	3.13±0.04	3.60±0.07	4.01±0.10	5.59±0.36	FLWO	4Shooter
3183.653	0.7	3.19±0.04	3.58±0.06	3.92±0.08	5.20±0.24	FLWO	4Shooter
3184.653	0.6	3.24±0.04	3.65±0.05	4.05±0.08	4.81±0.15	FLWO	4Shooter
3185.652	0.6	3.18±0.03	3.62±0.05	3.98±0.07	5.07±0.18	FLWO	4Shooter
3186.651	0.6	3.20±0.04	3.53±0.05	3.97±0.08	5.15±0.22	FLWO	4Shooter
3187.651	0.6	3.22±0.04	3.58±0.05	3.86±0.07	5.06±0.20	FLWO	4Shooter
3188.653	0.7	3.24±0.06	3.48±0.07	4.27±0.14	5.39±0.36	FLWO	4Shooter
3189.656	0.7	3.26±0.04	3.67±0.06	4.00±0.08	5.39±0.27	FLWO	4Shooter
3191.652	0.7	3.16±0.04	3.61±0.06	3.85±0.08	5.03±0.22	FLWO	4Shooter
3192.660	0.8	3.26±0.02	3.61±0.03	3.98±0.04	5.17±0.11	FLWO	4Shooter
3193.650	0.8	3.25±0.03	3.62±0.05	4.02±0.07	5.14±0.18	FLWO	4Shooter
3194.654	0.9	3.25±0.03	3.57±0.04	3.99±0.05	4.93±0.12	FLWO	4Shooter

Table B.1 – continued

HJD	χ^2/N_{dof}	Image A	Image B	Image C	Image D	Observatory	Detector
3195.652	0.6	3.21±0.04	3.61±0.05	3.94±0.07	4.95±0.18	FLWO	4Shooter
3310.011	0.3	3.24±0.04	3.54±0.05	4.04±0.08	4.66±0.14	FLWO	Minicam
3314.010	0.3	3.17±0.05	3.58±0.08	4.10±0.12	4.73±0.21	FLWO	Minicam
3315.021	0.2	3.18±0.12	3.78±0.20	4.16±0.28	4.09±0.27	FLWO	Minicam
3318.964	0.8	3.21±0.03	3.54±0.04	4.09±0.06	4.60±0.10	FLWO	Minicam
3321.023	0.6	3.24±0.03	3.61±0.04	4.00±0.05	4.64±0.09	FLWO	Minicam
3335.040	0.6	3.21±0.03	3.66±0.05	4.12±0.07	4.57±0.11	FLWO	Minicam
3336.026	0.5	3.21±0.03	3.59±0.04	4.11±0.07	4.65±0.11	FLWO	Minicam
3341.993	0.4	3.23±0.05	3.67±0.08	4.17±0.13	4.73±0.20	FLWO	Minicam
3349.604	4.2	3.26±0.06	3.67±0.09	4.15±0.30	6.49±1.83	Wise	TAVAS
3350.012	0.4	3.20±0.03	3.62±0.04	4.17±0.06	4.63±0.10	FLWO	Minicam
3350.998	0.7	3.19±0.02	3.67±0.03	4.18±0.05	4.72±0.08	FLWO	Minicam
3352.044	0.6	3.21±0.02	3.63±0.03	4.19±0.05	4.55±0.07	FLWO	Minicam
3352.572	2.4	3.30±0.06	3.78±0.09	4.29±0.22	6.01±0.86	Wise	TAVAS
3353.038	0.9	3.22±0.03	3.72±0.04	4.14±0.05	4.55±0.08	FLWO	Minicam
3354.033	0.8	3.22±0.02	3.66±0.03	4.15±0.05	4.60±0.07	FLWO	Minicam
3354.920	0.9	3.20±0.02	3.66±0.03	4.16±0.05	4.58±0.06	FLWO	Minicam
3359.000	1.6	3.26±0.05	3.88±0.08	4.49±0.17	5.03±0.28	Wise	Tektronix
3359.920	1.2	3.24±0.02	3.67±0.02	4.25±0.04	4.53±0.05	FLWO	Minicam
3360.000	0.4	3.30±0.09	3.63±0.12	4.48±0.26	4.85±0.35	Wise	Tektronix
3377.879	0.7	3.24±0.03	3.60±0.03	4.26±0.06	4.53±0.08	FLWO	Minicam
3378.945	0.4	3.26±0.03	3.63±0.04	4.25±0.06	4.51±0.08	FLWO	Minicam
3379.878	0.4	3.26±0.03	3.69±0.04	4.28±0.06	4.55±0.07	FLWO	Minicam
3380.000	1.3	3.32±0.05	3.67±0.07	4.36±0.14	4.95±0.24	Wise	Tektronix
3380.606	2.8	3.41±0.05	3.85±0.08	4.48±0.21	4.80±0.27	Wise	TAVAS
3381.581	1.6	3.46±0.15	3.99±0.24	4.60±0.53	4.97±0.70	Wise	TAVAS
3384.554	2.7	3.31±0.07	3.68±0.10	4.01±0.23	4.46±0.32	Wise	TAVAS
3385.816	0.4	3.37±0.01	3.69±0.01	4.39±0.02	4.45±0.02	APO	SPICam
3385.951	0.6	3.30±0.02	3.66±0.03	4.28±0.05	4.48±0.06	FLWO	Minicam
3386.453	2.7	3.30±0.08	3.65±0.11	4.41±0.36	5.99±1.20	Wise	TAVAS
3387.527	2.9	3.32±0.09	3.61±0.11	4.42±0.41	6.09±1.47	Wise	TAVAS
3387.960	0.7	3.33±0.03	3.63±0.03	4.31±0.06	4.52±0.07	FLWO	Minicam
3399.018	0.3	3.34±0.07	3.75±0.10	4.22±0.15	4.32±0.16	FLWO	Minicam
3399.714	0.2	3.34±0.05	3.67±0.06	4.39±0.12	4.53±0.14	FLWO	Minicam
3402.990	0.3	3.40±0.04	3.66±0.05	4.30±0.09	4.40±0.10	FLWO	Minicam
3403.412	2.0	3.32±0.06	3.83±0.10	4.49±0.25	4.82±0.34	Wise	TAVAS
3406.322	1.3	3.33±0.10	3.74±0.15	3.98±0.21	7.83±2.51	Wise	TAVAS
3408.375	2.0	3.41±0.07	3.69±0.09	4.16±0.19	5.43±0.55	Wise	TAVAS
3410.806	0.8	3.33±0.02	3.66±0.03	4.38±0.05	4.49±0.06	FLWO	Minicam
3411.452	2.8	(2.99±0.06)	3.49±0.11	4.14±0.31	4.82±0.54	Wise	TAVAS
3412.404	2.2	3.59±0.09	3.78±0.11	4.45±0.29	10.6±6.65	Wise	TAVAS
3416.000	0.6	3.53±0.10	3.64±0.11	4.54±0.25	4.94±0.35	Wise	Tektronix
3417.000	0.9	3.36±0.07	3.65±0.09	4.07±0.14	4.63±0.22	Wise	Tektronix
3419.000	0.5	3.44±0.07	3.65±0.09	4.64±0.21	5.06±0.29	Wise	Tektronix
3430.930	0.3	3.39±0.04	3.61±0.05	4.20±0.09	4.52±0.12	FLWO	Minicam
3431.738	0.6	3.36±0.03	3.68±0.04	4.27±0.06	4.46±0.07	FLWO	Minicam
3432.721	0.6	3.38±0.03	3.64±0.04	4.25±0.06	4.39±0.06	FLWO	Minicam
3433.740	0.9	3.36±0.03	3.66±0.03	4.28±0.05	4.38±0.06	FLWO	Minicam
3439.643	0.4	3.38±0.01	3.64±0.01	4.24±0.02	4.38±0.02	APO	SPICam
3439.719	0.7	3.34±0.03	3.65±0.03	4.21±0.05	4.47±0.06	FLWO	Minicam
3441.615	0.3	3.38±0.01	3.64±0.01	4.24±0.02	4.38±0.02	APO	SPICam
3441.797	0.6	3.35±0.03	3.67±0.04	4.22±0.06	4.44±0.07	FLWO	Minicam
3442.734	0.8	3.37±0.03	3.66±0.03	4.20±0.05	4.41±0.06	FLWO	Minicam
3443.748	1.2	3.35±0.03	3.68±0.04	4.26±0.07	4.49±0.08	FLWO	Minicam
3459.333	1.4	3.32±0.07	3.78±0.10	4.37±0.20	4.52±0.23	Wise	TAVAS
3462.836	0.3	3.32±0.04	3.74±0.05	4.27±0.08	4.54±0.11	FLWO	Minicam

Table B.1 – continued

HJD	χ^2/N_{dof}	Image A	Image B	Image C	Image D	Observatory	Detector
3462.859	1.2	3.38±0.01	3.67±0.01	4.22±0.02	4.37±0.02	APO	SPICam
3463.722	0.6	3.38±0.03	3.65±0.04	4.21±0.06	4.46±0.08	FLWO	Minicam
3464.719	0.8	3.38±0.02	3.68±0.03	4.17±0.04	4.44±0.05	FLWO	Minicam
3466.251	1.6	3.52±0.08	3.92±0.12	4.20±0.20	4.72±0.31	Wise	TAVAS
3467.320	2.3	3.49±0.06	3.79±0.08	4.37±0.21	4.78±0.30	Wise	TAVAS
3468.291	1.5	3.32±0.09	3.77±0.13	4.41±0.28	4.88±0.41	Wise	TAVAS
3469.756	0.3	3.40±0.05	3.77±0.07	4.32±0.12	4.36±0.13	FLWO	Minicam
3470.713	0.5	3.36±0.03	3.71±0.03	4.25±0.05	4.43±0.06	FLWO	Minicam
3471.000	0.5	3.46±0.09	3.75±0.11	4.07±0.15	4.52±0.22	Wise	Tektronix
3471.763	0.3	3.39±0.03	3.76±0.04	4.17±0.06	4.49±0.07	FLWO	Minicam
3472.766	0.9	3.40±0.03	3.71±0.03	4.28±0.05	4.45±0.06	FLWO	Minicam
3473.744	1.4	3.39±0.02	3.69±0.02	4.24±0.04	4.44±0.05	FLWO	Minicam
3474.743	0.8	3.40±0.02	3.72±0.03	4.21±0.04	4.44±0.05	FLWO	Minicam
3476.739	0.4	3.38±0.04	3.69±0.06	4.33±0.10	4.44±0.11	FLWO	Minicam
3477.735	0.6	3.40±0.05	3.67±0.06	4.29±0.10	4.42±0.11	FLWO	Minicam
3478.690	0.4	3.37±0.05	3.77±0.07	4.25±0.11	4.58±0.15	FLWO	Minicam
3485.738	0.3	3.39±0.05	3.77±0.07	4.27±0.12	4.43±0.14	FLWO	Minicam
3486.707	0.3	3.44±0.05	3.71±0.07	4.08±0.09	4.41±0.12	FLWO	Minicam
3487.675	1.1	3.40±0.03	3.71±0.03	4.28±0.05	4.44±0.06	FLWO	Minicam
3489.000	0.9	3.38±0.07	4.18±0.14	4.58±0.21	4.94±0.28	Wise	Tektronix
3492.710	0.5	3.42±0.04	3.72±0.05	4.22±0.08	4.53±0.10	FLWO	Minicam
3494.722	0.8	3.41±0.03	3.77±0.03	4.25±0.05	4.51±0.06	FLWO	Minicam
3495.722	0.3	3.35±0.06	3.70±0.08	4.42±0.15	4.34±0.14	FLWO	Minicam
3496.694	0.4	3.41±0.03	3.70±0.04	4.33±0.06	4.51±0.07	FLWO	Minicam
3497.720	0.4	3.44±0.03	3.73±0.04	4.31±0.06	4.42±0.07	FLWO	Minicam
3498.691	0.6	3.42±0.03	3.73±0.03	4.36±0.06	4.51±0.06	FLWO	Minicam
3499.695	0.7	3.40±0.03	3.74±0.03	4.30±0.05	4.38±0.05	FLWO	Minicam
3500.244	1.1	3.48±0.11	3.68±0.12	4.07±0.20	5.01±0.44	Wise	TAVAS
3501.245	1.3	3.41±0.08	3.63±0.10	4.55±0.25	5.03±0.37	Wise	TAVAS
3501.708	0.7	3.44±0.04	3.67±0.05	4.25±0.09	4.50±0.11	FLWO	Minicam
3501.817	0.2	3.46±0.02	3.73±0.02	4.32±0.04	4.46±0.04	APO	SPICam
3502.701	0.4	3.41±0.03	3.75±0.04	4.33±0.07	4.39±0.08	FLWO	Minicam
3503.666	0.7	3.44±0.03	3.73±0.04	4.22±0.05	4.54±0.07	FLWO	Minicam
3504.687	0.2	3.52±0.07	3.70±0.07	4.44±0.11	4.44±0.11	FLWO	Minicam
3509.698	0.3	3.46±0.05	3.72±0.07	4.18±0.10	4.28±0.11	FLWO	Minicam
3510.674	0.6	3.47±0.05	3.71±0.06	4.49±0.13	4.40±0.12	FLWO	Minicam
3516.680	0.5	3.47±0.03	3.78±0.04	4.29±0.06	4.37±0.07	FLWO	Minicam
3520.686	0.6	3.56±0.04	3.78±0.04	4.34±0.07	4.36±0.07	FLWO	Minicam
3521.691	0.5	3.52±0.03	3.83±0.04	4.37±0.07	4.34±0.07	FLWO	Minicam
3522.646	0.4	3.50±0.05	3.75±0.06	4.31±0.09	4.36±0.10	FLWO	Minicam
3524.667	0.6	3.53±0.03	3.83±0.04	4.28±0.06	4.41±0.07	FLWO	Minicam
3525.673	0.4	3.52±0.03	3.85±0.04	4.29±0.06	4.30±0.07	FLWO	Minicam
3527.651	0.7	3.51±0.03	3.90±0.05	4.33±0.07	4.36±0.07	FLWO	Minicam
3530.650	0.4	3.57±0.04	3.89±0.05	4.24±0.07	4.48±0.09	FLWO	Minicam
3536.660	0.3	3.55±0.07	3.88±0.10	4.11±0.12	4.42±0.16	FLWO	Minicam
3537.661	0.3	3.55±0.06	3.97±0.09	4.28±0.12	4.44±0.14	FLWO	Minicam
3538.652	0.4	3.51±0.06	3.83±0.08	4.15±0.11	4.45±0.14	FLWO	Minicam
3541.654	0.3	3.42±0.12	3.98±0.19	4.15±0.23	4.68±0.35	FLWO	Minicam
3547.650	0.3	3.60±0.06	4.08±0.09	4.34±0.12	4.45±0.13	FLWO	Minicam
3549.651	0.3	3.65±0.08	4.04±0.12	4.43±0.17	4.88±0.25	FLWO	Minicam
3655.027	3.5	3.55±0.02	3.98±0.02	4.18±0.05	4.53±0.06	MDM	RETROCAM
3656.000	5.0	3.62±0.01	3.99±0.01	4.13±0.03	4.64±0.03	MDM	RETROCAM
3664.001	1.1	3.55±0.05	4.05±0.07	4.16±0.09	4.77±0.15	FLWO	Keplercam
3664.001	4.3	3.63±0.01	4.02±0.01	4.12±0.03	4.70±0.04	MDM	RETROCAM
3667.967	0.6	3.64±0.05	3.97±0.06	4.09±0.08	4.95±0.16	FLWO	Keplercam
3668.006	3.5	3.64±0.02	3.98±0.02	4.04±0.04	4.72±0.07	MDM	RETROCAM

Table B.1 – continued

HJD	χ^2/N_{dof}	Image A	Image B	Image C	Image D	Observatory	Detector
3673.899	0.5	3.63±0.01	3.94±0.02	4.07±0.02	4.78±0.03	APO	SPICam
3674.990	0.6	3.60±0.04	3.94±0.05	4.05±0.06	4.75±0.10	FLWO	Keplercam
3676.001	1.0	3.56±0.03	3.93±0.03	4.04±0.04	4.86±0.08	FLWO	Keplercam
3676.969	0.3	3.47±0.09	3.71±0.11	4.17±0.16	4.94±0.31	FLWO	Keplercam
3677.013	2.8	3.61±0.01	3.92±0.02	4.10±0.03	4.73±0.05	MDM	RETROCAM
3677.995	9.2	3.62±0.01	3.91±0.01	4.06±0.04	4.70±0.04	MDM	RETROCAM
3678.997	3.0	3.63±0.01	3.91±0.01	4.07±0.02	4.76±0.03	MDM	RETROCAM
3679.013	1.0	3.58±0.03	3.88±0.04	4.02±0.05	4.86±0.10	FLWO	Keplercam
3679.995	0.6	3.58±0.04	3.95±0.05	4.01±0.06	4.80±0.11	FLWO	Keplercam
3681.004	1.3	3.55±0.02	3.95±0.03	4.05±0.04	4.88±0.08	FLWO	Keplercam
3684.012	0.6	3.65±0.05	3.86±0.06	4.01±0.07	4.59±0.12	FLWO	Keplercam
3685.017	0.7	3.58±0.03	3.94±0.05	4.04±0.05	4.81±0.10	FLWO	Keplercam
3686.564	4.6	3.48±0.07	3.83±0.09	3.99±0.23	4.89±0.50	Wise	TAVAS
3686.892	1.5	3.55±0.03	3.89±0.04	4.00±0.05	4.67±0.08	Palomar	SITE
3687.024	0.9	3.55±0.04	3.93±0.05	3.95±0.05	4.73±0.10	FLWO	Keplercam
3688.016	1.3	3.59±0.03	3.88±0.04	3.99±0.05	4.80±0.09	FLWO	Keplercam
3688.929	1.9	3.60±0.02	3.89±0.02	4.06±0.03	4.71±0.05	MDM	RETROCAM
3689.034	0.5	3.58±0.04	3.86±0.05	3.96±0.05	4.79±0.11	FLWO	Keplercam
3690.002	0.4	3.51±0.07	3.90±0.09	3.92±0.10	4.66±0.19	FLWO	Keplercam
3691.019	0.6	3.53±0.05	3.77±0.07	4.06±0.09	4.57±0.14	FLWO	Keplercam
3691.898	1.7	3.57±0.03	3.93±0.04	3.90±0.05	4.52±0.09	Palomar	SITE
3692.018	0.4	3.61±0.06	3.87±0.07	3.95±0.08	4.59±0.14	FLWO	Keplercam
3693.022	0.4	3.54±0.05	3.95±0.08	4.01±0.08	4.65±0.15	FLWO	Keplercam
3693.865	0.6	3.59±0.05	3.86±0.06	3.97±0.07	4.48±0.11	Palomar	SITE
3693.927	0.3	3.61±0.02	3.89±0.03	3.98±0.03	4.59±0.05	APO	SPICam
3694.012	0.6	3.56±0.05	3.99±0.07	4.06±0.08	4.55±0.12	FLWO	Keplercam
3694.862	0.8	3.65±0.05	3.98±0.06	3.94±0.06	4.64±0.11	Palomar	SITE
3698.919	3.6	3.64±0.01	3.94±0.01	4.02±0.02	4.58±0.03	MDM	RETROCAM
3700.601	0.7	-0.1±1.05	(-0.5±0.93)	1.68±2.03	-0.4±0.94	Wise	TAVAS
3700.927	1.3	3.59±0.02	3.91±0.03	4.04±0.04	4.65±0.06	FLWO	Keplercam
3700.997	2.0	3.62±0.01	(3.85±0.01)	4.02±0.02	4.59±0.02	MDM	RETROCAM
3701.581	0.9	3.00±0.24	(3.05±0.24)	3.78±0.46	12.2±7.76	Wise	TAVAS
3702.560	2.6	3.46±0.10	3.60±0.12	4.18±0.33	5.18±0.74	Wise	TAVAS
3706.012	3.4	3.61±0.02	3.93±0.02	4.01±0.05	4.61±0.08	FLWO	Keplercam
3707.581	3.3	3.48±0.07	4.10±0.12	4.08±0.22	5.01±0.48	Wise	TAVAS
3708.849	0.4	3.54±0.05	3.99±0.07	4.19±0.08	4.49±0.11	Palomar	SITE
3708.984	1.0	3.63±0.03	3.93±0.04	4.03±0.04	4.77±0.07	FLWO	Keplercam
3709.996	0.8	3.56±0.03	3.94±0.04	4.04±0.05	4.59±0.07	FLWO	Keplercam
3710.561	0.9	3.56±0.19	4.18±0.31	4.00±0.29	5.70±0.98	Wise	TAVAS
3710.896	0.6	3.61±0.01	3.93±0.01	4.05±0.01	4.55±0.02	APO	SPICam
3710.971	1.5	3.62±0.03	3.96±0.03	4.00±0.04	4.59±0.07	FLWO	Keplercam
3711.943	9.0	3.60±0.01	3.98±0.01	4.05±0.05	4.61±0.06	FLWO	Keplercam
3712.545	5.1	3.59±0.06	3.92±0.09	4.05±0.22	4.68±0.38	Wise	TAVAS
3712.871	1.2	3.53±0.02	4.02±0.03	4.06±0.04	4.53±0.05	FLWO	Keplercam
3712.891	4.1	(3.67±0.01)	4.01±0.01	4.07±0.03	4.58±0.03	MDM	RETROCAM
3713.483	3.1	3.63±0.06	4.14±0.09	4.23±0.19	5.16±0.41	Wise	TAVAS
3714.951	0.5	3.60±0.04	4.01±0.06	4.03±0.06	4.47±0.09	FLWO	Keplercam
3718.765	0.6	3.58±0.05	4.02±0.08	3.94±0.08	4.46±0.12	Palomar	SITE
3725.965	5.9	3.58±0.02	4.03±0.02	4.08±0.05	4.46±0.07	FLWO	Keplercam
3726.932	5.4	3.59±0.01	4.09±0.02	4.08±0.04	4.49±0.06	FLWO	Keplercam
3728.935	0.6	3.59±0.04	4.07±0.06	4.09±0.06	4.36±0.08	FLWO	Keplercam
3729.951	17.	3.61±0.01	4.09±0.01	4.10±0.05	4.46±0.05	MDM	RETROCAM
3729.984	2.0	3.58±0.02	4.06±0.03	4.11±0.05	4.46±0.06	FLWO	Keplercam
3730.951	0.6	3.55±0.05	4.05±0.08	4.09±0.08	4.39±0.10	FLWO	Keplercam
3731.854	0.6	3.56±0.04	4.04±0.05	4.06±0.05	4.52±0.08	FLWO	Keplercam
3732.464	3.3	3.50±0.05	4.23±0.10	4.38±0.22	4.79±0.31	Wise	TAVAS

Table B.1 – continued

HJD	χ^2/N_{dof}	Image A	Image B	Image C	Image D	Observatory	Detector
3734.457	3.0	3.59±0.07	3.94±0.09	4.29±0.22	4.55±0.28	Wise	TAVAS
3734.918	12.	3.63±0.01	4.11±0.01	4.15±0.04	4.48±0.04	MDM	RETROCAM
3736.018	3.9	3.59±0.01	4.06±0.01	4.09±0.02	4.41±0.03	MDM	RETROCAM
3736.902	3.8	3.63±0.01	4.07±0.01	4.12±0.02	4.44±0.02	MDM	RETROCAM
3737.923	3.4	3.62±0.01	4.09±0.01	4.13±0.03	4.43±0.03	MDM	RETROCAM
3738.961	2.7	3.60±0.01	4.08±0.02	4.12±0.03	4.42±0.04	MDM	RETROCAM
3740.032	0.6	3.54±0.03	4.05±0.05	4.12±0.05	4.47±0.07	FLWO	Keplercam
3740.910	3.1	3.66±0.01	4.12±0.01	4.20±0.02	4.46±0.02	MDM	RETROCAM
3741.012	0.6	3.49±0.06	3.98±0.09	3.97±0.09	4.75±0.17	FLWO	Keplercam
3741.885	1.8	(3.68±0.01)	(4.15±0.01)	4.20±0.02	4.47±0.02	MDM	RETROCAM
3742.992	1.5	3.57±0.02	4.11±0.03	4.13±0.04	4.45±0.05	FLWO	Keplercam
3743.772	5.2	3.52±0.02	4.09±0.03	4.02±0.06	4.28±0.08	Palomar	SITE
3743.976	19.	3.66±0.01	4.12±0.01	4.21±0.05	4.43±0.06	MDM	RETROCAM
3744.962	379	3.63±0.05	4.08±0.05	4.18±1.02	4.39±1.02	MDM	RETROCAM
3745.931	17.	3.60±0.01	4.09±0.02	4.12±0.07	4.38±0.09	MDM	RETROCAM
3745.970	0.7	3.62±0.03	4.05±0.05	4.09±0.05	4.28±0.06	FLWO	Keplercam
3747.024	8.5	3.65±0.01	4.09±0.01	4.19±0.04	4.37±0.04	MDM	RETROCAM
3749.000	2.1	3.65±0.01	4.07±0.01	4.25±0.02	4.41±0.03	MDM	Echelle
3752.918	1.1	3.64±0.02	4.07±0.02	4.20±0.03	4.47±0.04	MDM	Echelle
3753.950	1.7	3.61±0.02	4.00±0.03	4.07±0.04	4.37±0.05	FLWO	Keplercam
3755.878	2.6	3.65±0.01	(4.16±0.01)	4.13±0.02	4.38±0.02	MDM	RETROCAM
3755.897	0.4	3.59±0.04	4.04±0.06	4.15±0.07	4.33±0.08	FLWO	Keplercam
3756.929	3.3	3.65±0.01	4.06±0.01	4.12±0.02	4.35±0.02	MDM	RETROCAM
3757.884	14.	3.66±0.01	4.05±0.01	4.11±0.04	4.35±0.05	MDM	RETROCAM
3757.892	0.7	3.61±0.03	4.03±0.05	4.04±0.05	4.35±0.06	FLWO	Keplercam
3758.916	10.	3.66±0.01	4.03±0.01	4.09±0.04	4.35±0.04	MDM	RETROCAM
3758.937	0.6	3.62±0.03	4.02±0.04	4.05±0.05	4.40±0.06	FLWO	Keplercam
3761.985	0.6	3.65±0.09	3.99±0.13	4.36±0.18	4.56±0.21	Palomar	SITE
3762.389	2.2	3.58±0.09	4.03±0.13	3.89±0.18	4.46±0.28	Wise	TAVAS
3764.885	0.5	3.65±0.04	4.06±0.06	4.02±0.06	4.44±0.09	FLWO	Keplercam
3766.051	0.6	3.66±0.03	4.08±0.05	4.02±0.05	4.33±0.06	FLWO	Keplercam
3766.906	1.0	3.68±0.03	4.03±0.03	4.04±0.04	4.37±0.05	FLWO	Keplercam
3767.858	5.2	3.67±0.01	4.07±0.01	4.04±0.03	4.44±0.04	FLWO	Keplercam
3768.842	1.0	3.69±0.03	3.97±0.04	4.05±0.04	4.38±0.05	FLWO	Keplercam
3769.909	1.2	3.62±0.05	4.06±0.08	4.03±0.09	4.71±0.16	FLWO	Keplercam
3770.792	2.1	3.70±0.01	4.04±0.01	4.02±0.02	4.31±0.02	MDM	8K
3770.908	0.9	3.67±0.03	4.08±0.04	4.09±0.04	4.41±0.05	FLWO	Keplercam
3771.393	3.9	3.83±0.08	4.05±0.10	4.14±0.22	4.56±0.31	Wise	TAVAS
3771.772	5.1	3.64±0.02	3.94±0.02	3.95±0.05	4.25±0.06	MDM	8K
3771.870	0.6	3.75±0.05	4.07±0.06	4.11±0.06	4.38±0.08	FLWO	Keplercam
3772.435	1.7	3.61±0.08	3.91±0.11	4.10±0.17	4.88±0.34	Wise	TAVAS
3772.758	0.8	3.63±0.03	4.15±0.05	4.07±0.04	4.18±0.05	MDM	8K
3772.922	0.6	3.75±0.04	4.15±0.06	4.05±0.05	4.43±0.08	FLWO	Keplercam
3773.722	1.7	3.70±0.01	4.04±0.02	4.04±0.02	4.30±0.03	MDM	8K
3775.952	0.5	3.73±0.04	3.96±0.04	4.00±0.05	4.33±0.06	Palomar	SITE
3776.938	5.2	3.69±0.02	4.00±0.03	4.01±0.06	4.12±0.07	MDM	8K
3786.858	0.5	3.70±0.04	4.07±0.05	4.04±0.05	4.43±0.08	FLWO	Keplercam
3787.802	0.3	3.72±0.09	4.07±0.12	4.07±0.12	4.31±0.15	FLWO	Keplercam
3788.859	1.4	3.68±0.02	4.08±0.03	4.12±0.04	4.30±0.04	FLWO	Keplercam
3790.773	1.8	3.70±0.04	4.00±0.05	4.15±0.09	4.29±0.10	FLWO	Keplercam
3791.791	1.1	3.65±0.03	4.04±0.04	4.15±0.05	4.26±0.05	FLWO	Keplercam
3792.946	0.4	3.73±0.11	4.29±0.18	4.27±0.18	4.10±0.16	Palomar	SITE
3793.794	1.2	3.67±0.03	4.02±0.04	4.17±0.05	4.24±0.05	FLWO	Keplercam
3794.750	0.6	3.68±0.04	4.07±0.05	4.09±0.05	4.30±0.06	FLWO	Keplercam
3795.306	4.4	3.67±0.07	4.26±0.12	4.20±0.24	4.75±0.38	Wise	TAVAS
3797.286	2.4	3.64±0.07	4.01±0.09	4.06±0.16	4.90±0.33	Wise	TAVAS

Table B.1 – continued

HJD	χ^2/N_{dof}	Image A	Image B	Image C	Image D	Observatory	Detector
3797.797	0.5	3.60±0.05	4.07±0.07	4.09±0.07	4.19±0.08	FLWO	Keplercam
3798.375	4.0	3.58±0.04	3.93±0.06	4.16±0.15	4.39±0.19	Wise	TAVAS
3798.841	1.4	3.69±0.03	3.95±0.04	4.11±0.05	4.27±0.06	FLWO	Keplercam
3799.364	5.7	3.70±0.04	4.01±0.05	4.18±0.15	4.51±0.20	Wise	TAVAS
3799.854	0.7	3.68±0.03	3.97±0.04	4.07±0.05	4.17±0.05	FLWO	Keplercam
3800.037	0.7	3.64±0.05	3.88±0.06	4.16±0.08	4.16±0.08	Palomar	SITE
3800.791	0.3	3.60±0.09	4.06±0.14	4.12±0.15	4.22±0.16	FLWO	Keplercam
3815.828	0.7	3.71±0.04	4.01±0.05	4.18±0.06	4.21±0.07	FLWO	Keplercam
3816.330	2.4	3.67±0.05	4.07±0.07	4.40±0.15	4.32±0.14	Wise	TAVAS
3817.854	0.5	3.70±0.05	3.98±0.07	4.04±0.07	4.23±0.08	FLWO	Keplercam
3817.933	0.2	3.82±0.15	4.03±0.17	3.97±0.17	4.38±0.24	Palomar	SITE
3818.272	4.8	3.71±0.11	3.76±0.12	3.96±0.31	4.97±0.73	Wise	TAVAS
3818.843	0.9	3.67±0.05	4.00±0.06	4.22±0.08	4.29±0.09	FLWO	Keplercam
3819.721	1.0	3.82±0.06	3.92±0.06	4.37±0.10	4.22±0.09	FLWO	Keplercam
3820.240	6.9	3.64±0.06	4.04±0.09	4.17±0.27	4.32±0.31	Wise	TAVAS
3820.720	0.6	3.68±0.05	3.96±0.06	4.17±0.07	4.12±0.07	FLWO	Keplercam
3822.247	2.3	3.67±0.08	4.05±0.11	3.94±0.17	4.48±0.26	Wise	TAVAS
3823.696	1.5	3.70±0.03	3.98±0.03	4.14±0.05	4.16±0.05	FLWO	Keplercam
3827.816	0.6	3.72±0.04	3.94±0.05	4.22±0.06	4.08±0.05	FLWO	Keplercam
3827.919	0.7	3.75±0.03	3.94±0.03	4.17±0.04	4.15±0.04	Palomar	SITE
3832.752	0.6	3.67±0.07	4.09±0.11	4.36±0.14	4.05±0.11	FLWO	Keplercam
3837.715	0.5	3.71±0.07	3.94±0.09	4.02±0.09	4.12±0.10	FLWO	Keplercam
3841.669	0.7	3.75±0.04	3.92±0.05	4.09±0.06	4.28±0.07	FLWO	Keplercam
3843.674	1.2	3.65±0.03	3.90±0.04	4.15±0.06	4.19±0.06	FLWO	Keplercam
3844.642	0.8	3.71±0.04	3.95±0.04	4.13±0.05	4.27±0.06	FLWO	Keplercam
3845.668	0.8	3.67±0.04	3.86±0.04	4.16±0.05	4.24±0.06	FLWO	Keplercam
3846.265	1.8	3.70±0.06	3.84±0.07	4.15±0.13	4.43±0.17	Wise	TAVAS
3846.644	0.9	3.70±0.03	3.89±0.04	4.19±0.05	4.25±0.05	FLWO	Keplercam
3848.665	1.1	3.66±0.03	3.96±0.04	4.18±0.05	4.18±0.05	FLWO	Keplercam
3849.667	1.4	3.66±0.04	3.86±0.04	4.05±0.06	4.32±0.08	FLWO	Keplercam
3850.696	1.0	3.69±0.04	3.84±0.04	4.09±0.05	4.20±0.05	FLWO	Keplercam
3851.707	0.9	3.69±0.03	3.89±0.04	4.18±0.05	4.23±0.05	FLWO	Keplercam
3852.837	0.4	3.70±0.06	3.96±0.08	4.18±0.10	4.37±0.12	FLWO	Keplercam
3854.730	0.6	3.71±0.03	3.94±0.04	4.14±0.04	4.23±0.05	FLWO	Keplercam
3855.650	2.1	3.67±0.03	3.90±0.03	4.10±0.05	4.21±0.06	FLWO	Keplercam
3856.695	5.3	3.66±0.01	3.88±0.02	4.17±0.05	4.21±0.05	FLWO	Keplercam
3857.822	0.6	3.71±0.05	3.87±0.05	4.11±0.06	4.24±0.07	FLWO	Keplercam
3858.643	1.2	3.63±0.03	3.89±0.04	4.12±0.05	4.24±0.05	FLWO	Keplercam
3859.641	1.6	3.61±0.03	3.93±0.04	4.18±0.07	4.24±0.07	FLWO	Keplercam
3861.765	0.6	3.74±0.05	3.97±0.05	4.10±0.06	4.22±0.07	FLWO	Keplercam
3873.245	3.6	3.64±0.06	4.15±0.09	4.14±0.17	4.44±0.22	Wise	TAVAS
3875.259	0.8	3.61±0.11	3.99±0.15	4.37±0.22	4.64±0.27	Wise	TAVAS
3878.251	2.3	3.69±0.05	4.04±0.07	4.21±0.13	4.45±0.17	Wise	TAVAS
3879.245	1.3	3.68±0.07	4.07±0.09	4.20±0.12	4.15±0.12	Wise	TAVAS
3881.706	1.5	3.67±0.03	4.03±0.03	4.18±0.05	4.23±0.05	FLWO	Keplercam
3882.666	1.8	3.66±0.02	4.02±0.03	4.16±0.05	4.26±0.05	FLWO	Keplercam
3883.654	1.4	3.61±0.03	4.07±0.04	4.15±0.05	4.24±0.05	FLWO	Keplercam
3884.724	1.8	3.63±0.01	4.00±0.01	4.20±0.02	4.20±0.02	MDM	8K
3885.653	1.8	3.61±0.03	4.01±0.04	4.18±0.06	4.21±0.06	FLWO	Keplercam
3885.720	3.7	3.65±0.01	4.04±0.01	4.18±0.03	4.21±0.03	MDM	8K
3886.646	2.0	3.60±0.01	4.00±0.01	4.19±0.02	4.19±0.02	MDM	8K
3887.646	1.1	3.65±0.01	4.01±0.02	4.20±0.02	4.22±0.02	MDM	8K
3890.729	0.4	3.55±0.06	3.92±0.08	4.32±0.12	4.13±0.10	FLWO	Keplercam
3896.660	0.4	3.55±0.06	3.98±0.08	4.02±0.09	4.21±0.10	FLWO	Keplercam
3899.680	0.3	3.47±0.07	3.94±0.11	4.29±0.16	4.38±0.17	FLWO	Keplercam
3903.708	0.6	3.63±0.04	3.95±0.05	4.22±0.07	4.24±0.07	FLWO	Keplercam

Table B.1 – continued

HJD	χ^2/N_{dof}	Image A	Image B	Image C	Image D	Observatory	Detector
3907.679	0.8	3.62±0.03	3.99±0.04	4.18±0.05	4.30±0.05	FLWO	Keplercam
4019.006	1.1	3.45±0.03	3.88±0.03	4.33±0.03	4.32±0.03	MDM	RETROCAM
4029.001	2.0	3.49±0.03	3.95±0.03	4.38±0.03	4.35±0.03	MDM	RETROCAM
4031.006	1.5	3.53±0.03	3.98±0.03	4.41±0.03	4.36±0.03	MDM	RETROCAM
4035.026	1.0	3.48±0.03	4.02±0.03	4.33±0.03	4.39±0.03	MDM	RETROCAM
4035.980	2.2	3.51±0.03	4.00±0.03	4.34±0.03	4.36±0.03	MDM	RETROCAM
4039.016	2.0	3.58±0.03	4.06±0.03	4.39±0.03	4.43±0.03	MDM	RETROCAM
4043.955	0.9	3.51±0.03	3.92±0.03	4.25±0.03	4.30±0.03	MDM	RETROCAM
4044.949	0.9	3.53±0.03	3.93±0.03	4.26±0.03	4.32±0.03	MDM	RETROCAM
4045.966	0.8	3.47±0.03	3.98±0.03	4.45±0.04	4.27±0.03	MDM	RETROCAM
4046.966	1.0	3.51±0.03	3.92±0.03	4.27±0.03	4.28±0.03	MDM	RETROCAM
4047.004	0.5	3.43±0.10	3.91±0.16	4.41±0.25	4.62±0.30	FLWO	Keplercam
4048.968	1.3	3.52±0.03	3.92±0.03	4.28±0.03	4.34±0.03	MDM	RETROCAM
4050.008	1.0	3.52±0.03	3.94±0.03	4.24±0.03	4.32±0.03	MDM	RETROCAM
4054.008	0.6	3.49±0.03	3.88±0.03	4.26±0.05	4.34±0.05	FLWO	Keplercam
4059.902	1.4	3.58±0.03	4.00±0.03	4.41±0.03	4.39±0.03	MDM	RETROCAM
4059.947	1.5	3.49±0.03	3.94±0.03	4.29±0.03	4.42±0.03	FLWO	Keplercam
4060.884	2.6	3.48±0.03	3.91±0.03	4.28±0.03	4.41±0.03	FLWO	Keplercam
4065.001	0.9	3.50±0.03	3.88±0.03	4.34±0.04	4.33±0.04	FLWO	Keplercam
4066.006	0.8	3.51±0.05	3.82±0.06	4.31±0.10	4.30±0.10	FLWO	Keplercam
4067.965	1.4	(3.65±0.03)	(4.01±0.03)	4.49±0.03	4.44±0.03	MDM	RETROCAM
4070.954	1.2	3.52±0.03	3.84±0.03	4.33±0.04	4.31±0.04	FLWO	Keplercam
4071.884	1.0	3.57±0.03	3.85±0.03	4.29±0.03	4.31±0.03	MDM	RETROCAM
4072.014	1.5	3.53±0.03	3.86±0.03	4.32±0.03	4.32±0.03	FLWO	Keplercam
4072.890	1.1	3.53±0.05	3.82±0.06	4.32±0.09	4.30±0.09	FLWO	Keplercam
4072.949	0.8	3.55±0.03	3.87±0.03	4.30±0.03	4.39±0.03	MDM	RETROCAM
4073.894	0.6	3.59±0.03	3.87±0.03	4.34±0.04	4.33±0.04	MDM	RETROCAM
4074.897	1.3	3.57±0.03	3.84±0.03	4.28±0.03	4.30±0.03	MDM	RETROCAM
4074.996	1.0	3.51±0.04	3.87±0.05	4.35±0.08	4.39±0.08	FLWO	Keplercam
4075.993	0.9	3.55±0.04	3.80±0.05	4.31±0.08	4.46±0.09	FLWO	Keplercam
4076.029	1.1	3.60±0.03	3.85±0.03	4.35±0.03	4.31±0.03	MDM	RETROCAM
4081.022	1.3	3.55±0.03	3.87±0.04	4.18±0.06	4.44±0.07	FLWO	Keplercam
4082.865	1.2	3.52±0.03	3.80±0.03	4.19±0.05	4.33±0.05	FLWO	Keplercam
4084.972	0.8	3.51±0.03	3.84±0.03	4.28±0.03	4.39±0.03	FLWO	Keplercam
4086.877	0.9	3.52±0.03	3.83±0.03	4.24±0.05	4.42±0.06	FLWO	Keplercam
4092.985	0.6	3.56±0.03	3.94±0.04	4.26±0.06	4.43±0.07	FLWO	Keplercam
4093.956	3.2	3.53±0.03	3.78±0.03	4.25±0.05	4.33±0.05	FLWO	Keplercam
4094.999	0.6	3.54±0.03	3.85±0.04	4.24±0.05	4.45±0.06	FLWO	Keplercam
4096.038	2.1	(3.69±0.03)	3.99±0.03	4.41±0.03	4.45±0.03	MDM	RETROCAM
4096.050	1.2	3.57±0.03	3.87±0.03	4.21±0.04	4.32±0.04	FLWO	Keplercam
4100.947	1.0	3.57±0.03	3.89±0.04	4.14±0.05	4.43±0.07	FLWO	Keplercam
4102.850	0.4	3.67±0.09	3.85±0.10	4.25±0.15	4.20±0.15	FLWO	Keplercam
4107.900	0.7	3.67±0.06	4.02±0.08	4.23±0.10	4.69±0.15	FLWO	Keplercam
4108.972	0.9	3.50±0.04	4.01±0.06	4.27±0.08	4.33±0.09	FLWO	Keplercam
4109.979	0.6	3.55±0.06	4.09±0.10	4.27±0.12	4.49±0.15	FLWO	Keplercam
4111.021	1.1	3.49±0.03	3.97±0.05	4.24±0.07	4.24±0.07	FLWO	Keplercam
4115.026	0.6	3.47±0.03	3.92±0.04	4.12±0.05	4.35±0.06	FLWO	Keplercam
4117.922	1.2	3.52±0.03	3.96±0.03	4.13±0.04	4.26±0.04	FLWO	Keplercam
4126.888	1.4	3.50±0.03	3.95±0.04	4.31±0.05	4.21±0.05	FLWO	Keplercam
4127.928	0.8	3.53±0.03	3.90±0.04	4.31±0.06	4.21±0.05	FLWO	Keplercam
4128.896	2.0	3.51±0.03	3.97±0.04	4.28±0.06	4.25±0.05	FLWO	Keplercam
4137.930	1.0	3.51±0.04	4.04±0.07	4.36±0.09	4.31±0.09	FLWO	Keplercam
4138.775	0.7	3.56±0.05	4.11±0.08	4.19±0.09	4.39±0.11	FLWO	Keplercam
4139.857	1.7	3.41±0.05	3.99±0.08	4.14±0.10	4.34±0.12	FLWO	Keplercam
4140.820	1.4	3.51±0.03	4.00±0.03	4.34±0.04	4.27±0.04	FLWO	Keplercam
4150.876	1.4	3.54±0.03	4.03±0.04	4.35±0.05	4.23±0.05	FLWO	Keplercam

Table B.1 – continued

HJD	χ^2/N_{dof}	Image A	Image B	Image C	Image D	Observatory	Detector
4152.757	0.7	3.53±0.04	4.17±0.07	4.36±0.08	4.42±0.08	FLWO	Keplercam
4153.758	0.6	3.58±0.03	4.01±0.05	4.23±0.06	4.18±0.06	FLWO	Keplercam
4155.833	0.6	3.50±0.04	4.09±0.06	4.19±0.07	4.25±0.08	FLWO	Keplercam
4156.826	0.9	3.57±0.04	4.01±0.05	4.27±0.07	4.21±0.06	FLWO	Keplercam
4165.922	0.6	3.62±0.03	(4.45±0.03)	4.53±0.03	4.53±0.03	FLWO	Keplercam
4166.764	1.8	3.60±0.04	4.07±0.06	4.22±0.07	4.07±0.06	FLWO	Keplercam
4168.830	0.5	3.66±0.04	4.14±0.06	4.22±0.07	4.18±0.07	FLWO	Keplercam
4169.811	1.4	3.63±0.03	4.15±0.04	4.23±0.04	4.18±0.04	FLWO	Keplercam
4170.776	0.5	3.60±0.03	4.16±0.03	4.18±0.03	4.14±0.03	FLWO	Keplercam
4171.800	1.5	3.61±0.03	4.19±0.03	4.22±0.03	4.14±0.03	FLWO	Keplercam
4172.714	0.9	3.64±0.03	4.17±0.04	4.21±0.04	4.12±0.04	FLWO	Keplercam
4173.754	2.6	3.64±0.03	4.15±0.03	4.23±0.03	4.12±0.03	FLWO	Keplercam
4174.778	1.0	3.66±0.03	4.16±0.04	4.21±0.04	4.10±0.04	FLWO	Keplercam
4176.850	0.9	3.69±0.03	4.16±0.04	4.21±0.04	4.14±0.04	FLWO	Keplercam
4177.700	1.1	3.63±0.03	4.17±0.03	4.18±0.04	4.08±0.03	FLWO	Keplercam
4179.665	1.0	3.65±0.03	4.19±0.04	4.22±0.04	4.11±0.04	FLWO	Keplercam
4180.687	0.9	3.66±0.03	4.20±0.04	4.16±0.04	4.12±0.04	FLWO	Keplercam
4194.799	0.7	3.69±0.05	4.23±0.09	4.27±0.09	4.05±0.08	FLWO	Keplercam
4197.724	1.0	3.73±0.03	4.14±0.04	4.23±0.04	4.06±0.03	FLWO	Keplercam
4201.761	0.8	3.76±0.03	4.17±0.03	4.36±0.03	4.14±0.03	FLWO	Keplercam
4213.802	0.6	3.74±0.06	4.05±0.08	4.37±0.10	4.11±0.08	FLWO	Keplercam
4214.699	0.9	3.67±0.06	3.89±0.08	4.43±0.13	4.07±0.09	FLWO	Keplercam
4215.700	0.8	3.78±0.06	4.04±0.08	4.51±0.12	4.11±0.08	FLWO	Keplercam
4227.656	0.5	3.72±0.04	3.95±0.05	4.47±0.08	4.09±0.06	FLWO	Keplercam
4230.661	0.9	3.78±0.04	3.98±0.04	4.39±0.06	4.10±0.05	FLWO	Keplercam
4232.706	0.6	3.80±0.05	4.04±0.06	4.52±0.09	4.06±0.06	FLWO	Keplercam
4233.737	0.7	3.72±0.04	4.05±0.05	4.44±0.07	4.07±0.05	FLWO	Keplercam
4237.673	0.5	3.70±0.04	4.02±0.05	4.32±0.07	4.08±0.05	FLWO	Keplercam
4238.688	0.6	3.71±0.04	3.98±0.05	4.49±0.08	4.11±0.06	FLWO	Keplercam
4239.745	0.4	3.68±0.05	4.15±0.08	4.38±0.09	4.18±0.08	FLWO	Keplercam
4240.707	0.8	3.72±0.04	3.98±0.05	4.49±0.08	4.04±0.05	FLWO	Keplercam
4245.660	0.9	3.71±0.05	4.04±0.07	4.46±0.10	4.07±0.07	FLWO	Keplercam
4246.714	0.3	3.66±0.08	3.89±0.09	4.25±0.13	4.15±0.12	FLWO	Keplercam
4247.702	2.0	3.79±0.09	4.05±0.11	4.25±0.13	4.13±0.12	FLWO	Keplercam
4248.668	0.8	3.76±0.07	4.24±0.10	4.76±0.17	4.23±0.11	FLWO	Keplercam
4249.684	1.5	3.85±0.08	4.36±0.13	4.38±0.13	4.20±0.11	FLWO	Keplercam
4250.685	0.9	3.67±0.06	4.11±0.09	4.64±0.15	4.16±0.10	FLWO	Keplercam
4252.675	1.7	3.53±0.07	4.01±0.10	4.45±0.15	4.09±0.11	FLWO	Keplercam
4254.660	0.6	3.65±0.04	4.08±0.05	4.43±0.07	4.07±0.05	FLWO	Keplercam
4255.667	1.3	3.65±0.03	4.08±0.05	4.43±0.07	4.12±0.05	FLWO	Keplercam
4258.675	0.5	3.62±0.04	4.10±0.06	4.36±0.08	4.14±0.06	FLWO	Keplercam
4260.697	0.7	3.64±0.04	4.05±0.05	4.39±0.07	4.06±0.05	FLWO	Keplercam
4261.716	0.5	3.62±0.04	4.11±0.06	4.42±0.08	4.07±0.06	FLWO	Keplercam
4263.668	0.5	3.65±0.05	4.23±0.08	4.31±0.09	4.12±0.08	FLWO	Keplercam
4264.654	0.7	3.62±0.05	4.10±0.07	4.47±0.10	4.03±0.07	FLWO	Keplercam
4265.685	0.5	3.69±0.05	4.14±0.07	4.30±0.08	4.11±0.07	FLWO	Keplercam
4266.700	0.7	3.53±0.07	4.24±0.13	4.15±0.12	4.25±0.14	FLWO	Keplercam
4269.687	1.3	3.70±0.08	4.12±0.12	4.43±0.16	3.97±0.11	FLWO	Keplercam
4271.674	0.4	3.74±0.08	3.96±0.09	4.32±0.13	4.04±0.10	FLWO	Keplercam
4276.677	0.4	3.72±0.08	4.10±0.11	4.36±0.14	4.12±0.11	FLWO	Keplercam
4277.649	0.2	3.69±0.17	3.99±0.21	4.20±0.27	4.28±0.28	FLWO	Keplercam
4278.668	0.3	3.62±0.08	4.10±0.12	4.58±0.19	4.00±0.12	FLWO	Keplercam

Recommended Literature

The following books and articles have been very helpful while writing up this thesis. They give very good overviews on the research area and provide detailed knowledge on the underlying concepts of the relevant topics.

Quasar Absorption Line Systems

"Element Abundances through the Cosmic Ages", Pettini, M. , in "Cosmochemistry: The Melting Pot of Elements" Esteban, C., Garcia López, R., Herroro, A. & Sánchez, F., eds. 2004, 257-298

"The Lyman Alpha Forest in the Spectra of Quasistellar Objects", Rauch, M., Annu. Rev. Astron. Astrophys. 1998, 36, 267

"Damped Lyα Systems", Wolfe, A.M., Gawiser, E. & Prochaska, J.X., Annu. Rev. Astron. Astrophys. 2005, 43, 861

"IAU Colloq. 199: Probing Galaxies through Quasar Absorption Lines" Williams, P.R., Shu, C., Menard, B., eds. 2005

Gravitational Lensing

"Lectures on Gravitational Lensing", Narayan R. & Bartelmann M. 1996, astro-ph/9606001

"Gravitational Lensing: Strong, Weak & Micro", Schneider, P., Kochanek, C. S. & Wambsganss, J., in Saas-Fe Advanced Course 33, Meylan, G., Jetzer, P. & North, P., eds. 2006

"Gravitational Lensing in Astronomy", Wambsganss, J. , Living Rev. Relativity 1998, 1, 12

"Strong Gravitational Lenses in a Cold Dark Matter Universe", Oguri, M., Phd thesis 2004, astro-ph/0408573

Publications

Fohlmeister, J., Kochanek, C.S., Falco, E.E., Morgan, C.W., & Wambsganss, J.:
The Rewards of Patience: an 822 Day Time Delay in the Gravitational Lens SDSS J1004+4112.
2008, The Astrophysical Journal, 677

Fohlmeister, J., Kochanek, C.S., Falco, E.E., Wambsganss, J., Morgan, N., Morgan, C.W., Ofek, E.O., Maoz, D., Keeton, C.R., Barentine, J.C., Dalton, g., Dembicky, J., Ketzeback, W., McMillan, R., & Peters, C.S.:
A Time Delay for the Cluster-Lensed Quasar SDSS J1004+4112.
2007, The Astrophysical Journal, 663, 62

Heinmüller, J., Petitjean, P., Ledoux, C., Caucci, S.,& Srianand, R.:
Kinematics and star formation activity in the z_{abs}=2.03954 damped Lyman-a system towards PKS 0458-020.
2006, Astronomy & Astrophysics, 449, 33

Kubas, D., Cassan, A., Beaulieu, J.P., Coutures, C.,.., **Heinmüller, J.**, and 23 coauthors:
Full characterization of binary-lens event OGLE-2002-BLG-069 from PLANET observations.
2005, Astronomy & Astrophysics, 435, 941

Cassan, A., Beaulieu, J.-P., Brillant, S., Coutures, C.,.., **Heinmüller**, J., and 23 coauthors:
Probing the atmosphere of the bulge G5III star OGLE-2002-BLG-069 by analysis of microlensed Hα line.
2004, Astronomy & Astrophysics Letters, 419, 132

Heinmüller, J., Wisotzki, L.:
Evolution of Luminous Quasars from the Hamburg/ESO Survey.
In: Schielicke, R.E.(ed.): Short Contrib. Ann. Sci. Meeting Astron. Ges. Freiburg,
2003, Astronomische Nachrichten 324, Suppl. Issue 3, 49

Wisotzki, L., Schechter, P.L., Bradt, H.V., **Heinmüller**, J.,& Reimers, C.:
HE 0435-1223: A wide separation quadruple QSO and gravitational lens.
2002, Astronomy & Astrophysics, 395, 17

Bibliography

Adelberger, K. L., Shapley, A. E., Steidel, C. C., et al. 2005, ApJ, 629, 636

Alard, C. & Lupton, R. H. 1998, ApJ, 503, 325

Aracil, B., Petitjean, P., Smette, A., et al. 2002, A&A, 391, 1

Ballester, P., Dorigo, D., Disarò, A., Pizarro de La Iglesia, J. A., & Modigliani, A. 2000, in Astronomical Society of the Pacific Conference Series, Vol. 216, Astronomical Data Analysis Software and Systems IX, ed. N. Manset, C. Veillet, & D. Crabtree, 461–+

Bertin, E. & Arnouts, S. 1996, A&AS, 117, 393

Bolzonella, M., Miralles, J.-M., & Pelló, R. 2000, A&A, 363, 476

Boyle, B. J., Shanks, T., Croom, S. M., et al. 2000, MNRAS, 317, 1014

Braun, R. & Walterbos, R. A. M. 1992, ApJ, 386, 120

Briggs, F. H., Wolfe, A. M., Liszt, H. S., Davis, M. M., & Turner, K. L. 1989, ApJ, 341, 650

Bruzual A., G. & Charlot, S. 1993, ApJ, 405, 538

Chen, H.-W. & Lanzetta, K. M. 2003, ApJ, 597, 706

Chen, H.-W., Lanzetta, K. M., Webb, J. K., & Barcons, X. 2001, ApJ, 559, 654

Collier, S. & Peterson, B. M. 2001, ApJ, 555, 775

Condon, J. J., Cotton, W. D., Greisen, E. W., et al. 1998, AJ, 115, 1693

Coppolani, F., Petitjean, P., Stoehr, F., et al. 2006, MNRAS, 370, 1804

Corbett, E. A., Croom, S. M., Boyle, B. J., et al. 2003, MNRAS, 343, 705

Croom, S. M., Smith, R. J., Boyle, B. J., et al. 2004, MNRAS, 349, 1397

de Vries, W. H., Becker, R. H., White, R. L., & Loomis, C. 2005, AJ, 129, 615

Dekker, H., D'Odorico, S., Kaufer, A., Delabre, B., & Kotzlowski, H. 2000, in Presented at the Society of Photo-Optical Instrumentation Engineers (SPIE) Conference, Vol. 4008, Proc. SPIE Vol. 4008, p. 534-545, Optical and IR Telescope Instrumentation and Detectors, Masanori Iye; Alan F. Moorwood; Eds., ed. M. Iye & A. F. Moorwood, 534–545

Falco, E. E., Gorenstein, M. V., & Shapiro, I. I. 1985, ApJ, 289, L1

Fan, X., Strauss, M. A., Schneider, D. P., et al. 2001, AJ, 121, 54

Fassbender, R., Boehringer, H., Lamer, G., et al. 2008, ArXiv e-prints, 802

Fohlmeister, J., Kochanek, C. S., Falco, E. E., Morgan, C. W., & Wambsganss, J. 2007a, ArXiv e-prints, 710

Fohlmeister, J., Kochanek, C. S., Falco, E. E., et al. 2007b, ApJ, 662, 62

Fox, A. J., Petitjean, P., Ledoux, C., & Srianand, R. 2007, ApJ, 668, L15

Gil-Merino, R., Wambsganss, J., Goicoechea, L. J., & Lewis, G. F. 2005, A&A, 432, 83

Gil-Merino, R., Wisotzki, L., & Wambsganss, J. 2002, A&A, 381, 428

Gómez-Álvarez, P., Mediavilla, E., Muñoz, J. A., et al. 2006, ApJ, 645, L5

Green, P. J. 2006, ApJ, 644, 733

Hawkins, M. R. S. 2007, A&A, 462, 581

Inada, N., Oguri, M., Keeton, C. R., et al. 2005, PASJ, 57, L7

Inada, N., Oguri, M., Morokuma, T., et al. 2006, ApJ, 653, L97

Inada, N., Oguri, M., Pindor, B., et al. 2003, Nature, 426, 810

Irwin, M. J., Webster, R. L., Hewett, P. C., Corrigan, R. T., & Jedrzejewski, R. I. 1989, AJ, 98, 1989

Kanekar, N. & Chengalur, J. N. 2003, A&A, 399, 857

Kaspi, S., Brandt, W. N., Maoz, D., et al. 2007, ApJ, 659, 997

Kawaguchi, T., Mineshige, S., Umemura, M., & Turner, E. L. 1998, ApJ, 504, 671

Kawano, Y. & Oguri, M. 2006, PASJ, 58, 271

Kennicutt, Jr., R. C. 1998, ARA&A, 36, 189

Kochanek, C. S. 2002, ApJ, 578, 25

Kochanek, C. S. 2004, ApJ, 605, 58

Kochanek, C. S., Falco, E. E., Impey, C. D., et al. 1999, in American Institute of Physics Conference Series, Vol. 470, After the Dark Ages: When Galaxies were Young (the Universe at $2 < z < 5$), ed. S. Holt & E. Smith, 163–+

Kochanek, C. S., Morgan, N. D., Falco, E. E., et al. 2006, ApJ, 640, 47

Kogut, A., Lineweaver, C., Smoot, G. F., et al. 1993, ApJ, 419, 1

Kundic, T., Colley, W. N., Gott, J. R. I., et al. 1995, ApJ, 455, L5+

Kundic, T., Turner, E. L., Colley, W. N., et al. 1997, ApJ, 482, 75

Lamer, G., Schwope, A., Wisotzki, L., & Christensen, L. 2006, A&A, 454, 493

Landolt, A. U. 1992, AJ, 104, 340

Lanzetta, K. M., Bowen, D. V., Tytler, D., & Webb, J. K. 1995, ApJ, 442, 538

Le Brun, V., Bergeron, J., & Boisse, P. 1996, A&A, 306, 691

Le Brun, V., Bergeron, J., Boisse, P., & Deharveng, J. M. 1997, A&A, 321, 733

Ledoux, C., Petitjean, P., & Srianand, R. 2003, MNRAS, 346, 209

Lowrance, J. L., Morton, D. C., Zucchino, P., Oke, J. B., & Schmidt, M. 1971, in Bulletin of the American Astronomical Society, Vol. 3, Bulletin of the American Astronomical Society, 238–+

Matthews, T. A. & Sandage, A. R. 1963, ApJ, 138, 30

Møller, P., Fynbo, J. P. U., & Fall, S. M. 2004, A&A, 422, L33

Møller, P. & Warren, S. J. 1993, A&A, 270, 43

Møller, P., Warren, S. J., & Fynbo, J. U. 1998, A&A, 330, 19

Morgan, C. W., Byard, P. L., DePoy, D. L., et al. 2005, AJ, 129, 2504

Morton, D. C. 2003, ApJS, 149, 205

Mortonson, M. J., Schechter, P. L., & Wambsganss, J. 2005, ApJ, 628, 594

Myers, A. D., Brunner, R. J., Richards, G. T., et al. 2006, ApJ, 638, 622

Nagamine, K., Springel, V., & Hernquist, L. 2004, MNRAS, 348, 435

Narayan, R. & Bartelmann, M. 1996, ArXiv Astrophysics e-prints

Oguri, M. 2004, PhD thesis, AA(The University of Tokyo)

Oguri, M. 2006, MNRAS, 367, 1241

Oguri, M. 2007, ApJ, 660, 1

Oguri, M., Inada, N., Keeton, C. R., et al. 2004, ApJ, 605, 78

Oguri, M., Ofek, E. O., Inada, N., et al. 2008, ArXiv e-prints, 802

Ota, N., Inada, N., Oguri, M., et al. 2006, ApJ, 647, 215

Pelt, J., Hoff, W., Kayser, R., Refsdal, S., & Schramm, T. 1994, A&A, 286, 775

Pelt, J., Kayser, R., Refsdal, S., & Schramm, T. 1996, A&A, 305, 97

Pelt, J., Schild, R., Refsdal, S., & Stabell, R. 1998, A&A, 336, 829

Pequignot, D. & Aldrovandi, S. M. V. 1986, A&A, 161, 169

Péroux, C., Dessauges-Zavadsky, M., D'Odorico, S., Kim, T.-S., & McMahon, R. G. 2003, MNRAS, 345, 480

Persson, S. E., Murphy, D. C., Krzeminski, W., Roth, M., & Rieke, M. J. 1998, AJ, 116, 2475

Peterson, B. M., Ferrarese, L., Gilbert, K. M., et al. 2004, ApJ, 613, 682

Petitjean, P., Surdej, J., Smette, A., et al. 1998, A&A, 334, L45

Pettini, M. 2004, in Cosmochemistry. The melting pot of the elements, ed. C. Esteban, R. García López, A. Herrero, & F. Sánchez, 257–298

Pettini, M., Shapley, A. E., Steidel, C. C., et al. 2001, ApJ, 554, 981

Pichon, C., Vergely, J. L., Rollinde, E., Colombi, S., & Petitjean, P. 2001, MNRAS, 326, 597

Poindexter, S., Morgan, N., Kochanek, C. S., & Falco, E. E. 2007, ApJ, 660, 146

Press, W. H., Rybicki, G. B., & Hewitt, J. N. 1992, ApJ, 385, 416

Prochaska, J. X., Herbert-Fort, S., & Wolfe, A. M. 2005, ApJ, 635, 123

Prochaska, J. X. & Wolfe, A. M. 1997, ApJ, 487, 73

Prochaska, J. X. & Wolfe, A. M. 1999, ApJS, 121, 369

Rauch, M. 1998, ARA&A, 36, 267

Refsdal, S. 1964a, MNRAS, 128, 307

Refsdal, S. 1964b, MNRAS, 128, 295

Rengstorf, A. W., Brunner, R. J., & Wilhite, B. C. 2006, AJ, 131, 1923

Richards, G. T., Keeton, C. R., Pindor, B., et al. 2004, ApJ, 610, 679

Rodríguez, E., Petitjean, P., Aracil, B., Ledoux, C., & Srianand, R. 2006, A&A, 446, 791

Schild, R. & Thomson, D. J. 1995, AJ, 109, 1970

Schneider, P., Kochanek, C. S., & Wambsganss, J. 2006, in Saas-Fee Advanced Course 33: Gravitational Lensing: Strong, Weak and Micro, ed. G. Meylan, P. Jetzer, P. North, P. Schneider, C. S. Kochanek, & J. Wambsganss

Shapiro, I. I. 1964, Physical Review Letters, 13, 789

Sharon, K., Ofek, E. O., Smith, G. P., et al. 2005, ApJ, 629, L73

Srianand, R., Shaw, G., Ferland, G., Petitjean, P., & Ledoux, C. 2005, ArXiv Astrophysics e-prints

Takahashi, R. & Chiba, T. 2001, ApJ, 563, 489

Tripp, T. M., Lu, L., & Savage, B. D. 1998, ApJ, 508, 200

Vanden Berk, D. E., Richards, G. T., Bauer, A., et al. 2001, AJ, 122, 549

Vanden Berk, D. E., Wilhite, B. C., Kron, R. G., et al. 2004, ApJ, 601, 692

Veilleux, S., Cecil, G., & Bland-Hawthorn, J. 2005, ARA&A, 43, 769

Voges, W., Aschenbach, B., Boller, T., et al. 1999, A&A, 349, 389

Vreeswijk, P. M., Ellison, S. L., Ledoux, C., et al. 2004, A&A, 419, 927

Walsh, D., Carswell, R. F., & Weymann, R. J. 1979, Nature, 279, 381

Wambsganss, J. 1998, Living Reviews in Relativity, 1, 12

Wambsganss, J. 2003, Nature, 426, 781

Wambsganss, J., Paczynski, B., & Schneider, P. 1990, ApJ, 358, L33

Warren, S. J., Møller, P., Fall, S. M., & Jakobsen, P. 2001, MNRAS, 326, 759

Weatherley, S. J., Warren, S. J., Møller, P., et al. 2005, MNRAS, 358, 985

Wilhite, B. C., Brunner, R. J., Grier, C. J., Schneider, D. P., & Vanden Berk, D. E. 2008, MNRAS, 383, 1232

Wilhite, B. C., Vanden Berk, D. E., Brunner, R. J., & Brinkmann, J. V. 2006, ApJ, 641, 78

Williams, L. L. R. & Saha, P. 2004, AJ, 128, 2631

Williams, P., Shu, C.-G., & Menard, B., eds. 2005, Probing Galaxies through Quasar Absorption Lines

Williger, G. M., Smette, A., Hazard, C., Baldwin, J. A., & McMahon, R. G. 2000, ApJ, 532, 77

Wisotzki, L., Schechter, P. L., Bradt, H. V., Heinmüller, J., & Reimers, D. 2002, A&A, 395, 17

Wolfe, A. M. 2005, in IAU Colloq. 199: Probing Galaxies through Quasar Absorption Lines, ed. P. Williams, C.-G. Shu, & B. Menard, 148–155

Wolfe, A. M., Briggs, F. H., Turnshek, D. A., et al. 1985, ApJ, 294, L67

Wolfe, A. M., Gawiser, E., & Prochaska, J. X. 2003, ApJ, 593, 235

Wolfe, A. M., Gawiser, E., & Prochaska, J. X. 2005, ARA&A, 43, 861

Young, P. A., Impey, C. D., & Foltz, C. B. 2001, ApJ, 549, 76

Acknowledgements

This is the end of my thesis[1] and following the old tradition I am glad to finally have the chance to acknowledge all the people that helped me. First of all, I want to express my acknowledgements to my supervisor Prof. Joachim Wambsganß for providing the opportunity, freedom and financial support to do this work. Thanks to him I discovered the interesting field of gravitational lensing. I am grateful for his advice, for his trust and for encouraging me to present and publish my results.

It is a pleasure to thank Patrick Petitjean for selecting me for a six month Marie Curie Fellowship at the Institut d'Astrophysique de Paris (IAP). The professional guidance and stimulating discussions provided by him and his group made my stay in Paris an absorbing experience. His expertise on quasar absorption line systems significantly helped to improve parts of this thesis.

During my time as a PhD student, every few months Emilio Falco cheered me up by sending new monitoring data of the wide separation lensed quasar SDSS J1004+4112, making its light curve more and more fascinating. I want to thank him and the staff at Fred Lawrence Whipple observatory for their hospitality during the week I spent there observing. I thank Chris Kochanek for his collaboration and the supply of additional monitoring data. While writing the papers on the time delays he was an excellent mentor, promptly answering emails and substantially improving the contents.
Further thanks goes to all the other collaborators on my papers, especially Cédric Ledoux, Sara Caucci, Raghunathan Srianand and Chris Morgan for their fundamental contributions.

I want to thank Prof. Matthias Bartelmann, Prof. Eva Grebel and Prof. Franz Eisele for their interest in my work and their immediate agreement to be part of my PhD committee.

The first year of my thesis was spent in the Potsdam astrophysics group. The friendly atmosphere there, especially at the coffee breaks with Achim, Adriane, Andreas, Götz, Helge, Lida, Olaf, Rodrigo, Robert and Wolf-Rainer will always be a happy memory.
I also want to thank all the students at IAP for shared dreams, drinks and desperation, especially Ali, Francois, JC, Michal and Sara. The couch in your office was always a good refuge.
Among the lensing group at the ARI in Heidelberg, I wish to thank Mr. "Planet" Arnaud for inviting us to his house, Ms. "Lens Discovery" Cécile for valuable scientific comments and very good advice, Mr. "I told you." Jonathan for his patience with pregnant women

[1] For those who only read this, please also have a look at the rest, at least the Figures are nice.

and non-native English speakers, Mr. “Chatting” Robert for questioning my intention to finish my PhD and Mr. “Singing” Timo for his cheerfulness.

During all these years, I was very fortunate with my officemates. It was a great pleasure sharing an office with Dijana Dominis, Daniel Kubas, Alessandro Fabbri, Atsunori Yonehara, Nick Bate, Christine Liebig and the most affectionate woman in this world: Marta Zub.

Every institute profits from good souls, that care for human relations and stand out for having creative solutions to all kinds of problems. I found them in Andrea Brockhaus, Chantal Le Vaillant, Irene Seckel and Helga Ballmann.

A very special thanks goes to Jessica Agarwal. Her strength and determination in finishing a PhD while having a small child was a big source of motivation for me.

Numerous people read and corrected this thesis. I am deeply indebted to Cécile Faure, Jonathan Duke, Timo Anguita and Nick Bate for their tremendous and immediate help.

Finally I want to thank my parents for all the backup they could provide from what seemed to be a cosmological distance. My deepest thanks goes to Jens and Henry for supporting and believing in me. You are my heroes !